Interim Report

entitled

Computational and Theoretical Analysis of Free Surface Flow in a Thin Liquid Film Under Zero and Normal Gravity

by

Amir Faghri
Professor
Department of Mechanical Systems Engineering
Wright State University
Dayton, Ohio 45435
Tel. (513) 873-2501

to

Theodore D. Swanson
NASA Goddard Spaceflight Center
Contract # NAG 5-956

Date of Submission
October 20, 1988

Table of Contents

I. COMPUTATION AND ANALYSIS OF FREE SURFACE FLOW OF A THIN LIQUID FILM UNDER ZERO AND NORMAL GRAVITY

1.1 Summary

The results of a numerical computation and theoretical analysis are presented for the flow of a thin liquid film in the presence or absence of a gravitational body force. The numerical computations employed a curvilinear body-fitted coordinate system. The governing transport equations were discretized using the finite control-volume formulation and solved implicitly. The computer code PHOENICS was used for this purpose.

Five different flow systems were studied: (a) falling film down a vertical wall, (b) plane film flow along a horizontal plate, (c) plane film flow at zero gravity, (d) radial film flow along a horizontal plate and (e) radial film flow at zero gravity. In all these systems, the distribution of the film height, the flow field and resistance exerted by the solid wall were studied.

For the flow of a laminar falling film, a fully-developed flow regime is present where an equilibrium is established between the gravitational body force and the shear force at the wall. It was found that a film introduced at a height above or below the equilibrium height eventually reaches the equilibrium condition for that flow rate. In the developing region, the height of the free surface and the distribution of the velocity components change simultaneously. For plane flow along a horizontal plate, the film height rises up and forms a hydraulic jump where a change of the

flow regime from supercritical to subcritical takes place. For plane flow under zero gravity, the film height increases monotonically. The shape of the velocity profile becomes parabolic after some distance from the entrance but the flow never attains a fully-developed condition.

For radial flow the height of the film and the downstream flow structure are determined by the flow rate, inlet height and magnitude of the gravitational acceleration. For larger flow rates, the film height decreases downstream under zero gravity whereas the film height increases slightly downstream when the gravitational body force is present. For smaller flow rates and inlet film heights, the fluid level downstream rises to a height above the inlet. This rise happens suddenly under normal gravity whereas the rise occurrs more gradually under zero gravity. The level of the fluid decreases slowly after the jump. This rise or jump is also found to be associated with a region of flow separation. The flow re-attaches after the separation zone and the velocity profile becomes parabolic downstream.

1.2 Introduction

The flow of a thin liquid film is encountered in many engineering devices. During evaporation or condensation on a solid surface in a compact heat exchanger or cooling tower, spin coating in metal industries, and impingement of a liquid jet on a solid wall as in impingement cooling, a thin film is quite commonly found. Besides practical applications, the fluid mechanics of thin film flow is important from a theoretical point of view since both viscosity and free-surface effects are important in these flows. Moreover, the understanding of such flows under reduced or zero gravity is essential for proper design of heat exchangers for space applications.

The falling of a thin liquid film along a plane vertical wall has been studied by many investigators since the turn of this century. For steady fully-developed laminar flow, a theoretical solution can be derived from a simple balance between the gravitational body force and the shear force at the solid wall (Bird, et al. [1]). The film height remains constant and the velocity profile across the film becomes parabolic in the fully developed region. The analysis of developing flow when a film is introduced at its equilibrium height is also available in the literature.

A film falling under the influence of gravity ceases to be laminar and constant in thickness when the flow rate is high. Waves tend to appear on the surface and the flow becomes turbulent as the flow rate is increased. A number of theoretical as well as experimental studies have been performed to understand the flow in wavy-laminar and turbulent regions. A review of such studies has been prepared by Faghri and Payvar [2]. This review also

included the experimental studies on laminar flow with constant thickness.

A somewhat less studied problem is the spread of a liquid film over a plate. Watson [3] presented results of analytical and experimental studies of the radial spread of a liquid jet impinging on a horizontal plane for laminar and turbulent flows. By using the boundary layer approximations for the governing equations, he derived analytical solutions using a similarity transformation along with the Pohlhausen integral method. His analysis covered the regions where the boundary layer thickness is less than the film height and where the film is totally engulfed by the boundary layer. The effects of the gravitational pressure gradient was discussed. The possibility of a hydraulic jump in such a flow was also anticipated. However, the analysis was applicable only to regions before the jump and the jump height could be predicted for any given location of the jump. The agreement between the experimental data and the analysis was satisfactory.

Another interesting problem of thin film research is the spreading of the film under the action of centrifugal force as seen in a rotating system. An approximate analytical solution for laminar flow on a rotating disk was developed by Rauscher et al. [4]. An asymptotic expansion technique was used where the radial spread of the fluid was perturbed to determine the effects of convection, Coriolis acceleration, radial diffusion, surface curvature and surface tension. These higher order effects were discussed on a physical basis. The turbulent counterpart of the rotating disk problem was solved by Murthy [5] where the governing transport equations were integrated across the thickness of the film and the reduced equations were solved analytically.

The heat transfer in a thin film has also been studied by many investigators, particularly dealing with evaporation or condensation. The earliest study in this regard is credited to Nusselt [6], who developed an analytical solution for film condensation along a vertical isothermal wall. The analysis given by Nusselt has been improved by several investigators to include the effects of inertia, vapor pressure, etc. Sparrow and Gregg [7] developed a theory for rotating condensation where the removal of the condensate took place due to centrifugal force instead of the force due to gravity. Butuzov and Rifert [8] performed experiments to verify the theory developed in [7]. In a more recent study, Butuzov and Rifert [9] presented experimental as well as theoretical results for the reverse problem of film evaporation from a rotating disk.

In the previous studies concerning thin liquid films, the investigators have tried to develop analytical models or have taken experimental data. Some of these models are quite approximate in nature and do not bring out the finer details of the flow field. A numerical finite-difference solution of a thin film flow is not available at the present time. These flows are difficult to solve by the finite-difference method since the geometry of the free surface is not known ahead of time, and the surface profile cannot be fitted in a regular Cartesian or cylindrical coordinate system. Moreover, none of the studies mentioned above has considered the flow under reduced or zero gravity, which is expected to be different from the flow under normal gravity. A proper understanding of such flows is essential in the design of space cooling systems.

The present study is undertaken to develop a general numerical solution procedure for thin film flows which can be applicable to both plane and radial systems, and to both normal and zero gravity environments. The numerical solution is supplemented with a one-dimensional analysis. The results highlight the effects of gravity for different configurations of the flow.

1.3 Problem Formulation

The equations governing the conservation of mass and momentum in a thin film of fluid which is newtonian with constant properties are given by

$$\nabla \cdot \vec{V} = 0 \tag{1.1}$$

$$\rho \frac{D\vec{V}}{Dt} = - \nabla p + \mu \nabla^2 \vec{V} + \rho \vec{g} \tag{1.2}$$

These governing equations have to be supplemented with appropriate boundary conditions. At the solid wall the no-slip condition exists, therefore, $\vec{V} = 0$. On the free surface the shear stress vanishes which implies $\partial \vec{V} / \partial n = 0$, where n is the coordinate normal to the free surface. Moreover, in the absence of any significant surface tension, the static pressure on the free surface must equal the ambient pressure. By setting p equal to the difference between the actual and ambient pressures, then p = 0 on the free surface since pressure is a scalar quantity. Boundary conditions must also be assigned in the direction of the flow at two locations if the problem is elliptic. The locations usually are the

entrance and exit to the control volume or computation domain. At the entrance, the film height and velocity are prescribed: $h = h_{in}$, and $\vec{V} = \vec{V}_{in}$. These also determine the flow rate and the Reynolds and Froude numbers. At the exit the flow condition is usually unknown, so the fully developed condition $\partial\vec{V}/\partial n = 0$ is prescribed. Moreover, if the film height or Froude number is known at the exit, this information can also be prescribed as a boundary condition. A boundary condition for the pressure has to be given at one location in the direction of the flow. In the numerical computation, it is convenient to prescribe this condition at the outlet of the flow field. The coordinate system used here is shown in Fig. 1.1. The boundary conditions for different flow systems are listed in Table 1 in the component form. The flow configurations considered in the present investigation are shown in Fig. 1.2. They can be broadly classified into two groups:

(P) Plane thin film flow

(R) Radial thin film flow

In the first group, three problems will be considered:

(P1) Falling film along a vertical wall

(P2) Plane flow along a horizontal wall

(P3) Plane flow under zero gravity

The first case is a classical problem where the major driving mechanism is the gravitational body force. This problem was used to check the accuracy of the present numerical scheme. The effects of introducing the film at a height other than the equilibrium height for a given flow

rate will be investigated for this case.

For plane flow along a horizontal wall, different flow regimes may be present depending on the film height and fluid velocity. For plane flow under zero gravity, the orientation of the solid wall is immaterial. The flow remains the same whether the plate is vertical, horizontal or inclined. In this case, the flow is driven by inertial and viscous forces.

In the second group, we will again consider two problems according to the presence or absence of gravity.

(R1) Radial flow under zero gravity

(R2) Radial flow along a horizontal plate under normal gravity.

As the flow spreads out radially, the cross sectional area of the flow increases downstream. The velocity decreases downstream due to friction and the change in area. The flow field changes continuously as the fluid moves downstream and can never become fully developed. Different phenomena may also happen according to the rate of the flow.

1.4 Theoretical Analysis

We consider the one-dimensional flow of a thin film where the film height h is a function of the radial (longitudinal, for plane flow) location r. Let W be the average velocity of the film in that direction and Q be the volume flow rate. In the case of plane flow, Q is the volume flow rate per unit of cross sectional area. The volume flow rate is given by

$$Q = (2\pi\, r)^K\, hW \tag{1.3}$$

where $K = \begin{cases} 0, \text{ for plane system} \\ 1, \text{ for radial system} \end{cases}$

Expressing the friction at the wall in terms of the friction coefficient gives

$$\tau_w = c_f \frac{\rho W^2}{2} \tag{1.4}$$

It is assumed that c_f is constant in the present analysis.

Integrating eqn. (1.2) across the thickness of the film and substituting the eqns. (1.3) and (1.4) results in

$$\frac{d}{dr}\left(\frac{W^2}{2} + gh \right) = - \frac{c_f}{2} \frac{W^2}{h} \tag{1.5}$$

This momentum equation has to be solved along with eqn. (1.3) to determine the flow field, and will be carried out in the following subsections.

1.4.1 Flow Under Zero Gravity

For a steady flow under zero gravity, the governing equations, eqns. (1.3) and (1.5), reduce to

$$Q = (2\pi r)^K\, hW = \text{constant} \tag{1.6}$$

$$W \frac{dW}{dr} = - \frac{c_f}{2} \frac{W^2}{h} \tag{1.7}$$

Eliminating h from eqns. (1.6) and (1.7) gives

$$W^{-2}\, dW = - \frac{c_f}{2Q} (2\pi r)^K \, dr$$

Integrating this equation and substituting the inlet boundary condition (i.e., at $r = r_1$, $W = W_1$ and $h = h_1$) yields the solution in the form

$$\frac{W}{W_1} = \frac{1 - \frac{c_f}{2} \frac{r}{(K+1)h}}{1 - \frac{c_f}{2} \frac{r_1}{(K+1)\, h_1}} = \frac{h_1}{h} \left(\frac{r_1}{r} \right)^K \tag{1.8}$$

Solving for h results in the following relation

$$\frac{h}{h_1} = A \frac{r}{r_1} + (1 - A) \left(\frac{r_1}{r} \right)^K \tag{1.9}$$

$$\text{where } A = \frac{c_f}{2} \frac{r}{(K+1)h_1} \tag{1.10}$$

It can be observed in eqn. (1.9) that for plane flow where K = 0 the film height increases monotonically with radial location r. This increase in height is due to a decrease in velocity because of friction. For inviscid flow when no resistance is exerted by the solid wall, the film height remains the same at all downstream locations beginning from the

entrance. In an axisymmetric radial system, however, it is noticed that h can decrease or increase depending on the radial location. The location for the minimum h can be determined by differentiating eqn. (1.9) which gives

$$\left(\frac{r}{r_1} \right)_{\text{for min } h} = \left(\frac{1 - A}{A} \right)^{1/2} \tag{1.11}$$

$$\left(\frac{h}{h_1} \right)_{\min} = 2 \sqrt{A} \sqrt{1 - A} \tag{1.12}$$

From eqn. (1.11) we find that a minimum exists if $A < 1/2$. Otherwise, the film height increases continuously from the entrance.

1.4.2 Flow on a horizontal plane under normal gravity

This analysis is applicable for radial and planar flows under normal gravity with a free surface. The flow of a thin film resembles open channel flow, so the Froude number may be a useful parameter. We define the Froude number as

$$Fr = \frac{W}{\sqrt{gh}} \tag{1.13}$$

Expressing eqns. (1.3) and (1.5) in terms of the Froude number results in

$$Q = (2\pi r)^K \sqrt{g}\, Fr\, h^{3/2} \tag{1.14}$$

$$\frac{d}{dr} \left[h \left(1 + \frac{Fr^2}{2} \right) \right] = - \frac{c_f}{2} Fr^2 \tag{1.15}$$

(a) Plane Flow

For plane flow, K = 0, so eqns. (1.14) and (1.15) can be reduced to the following form:

$$\frac{dFr}{dR} = -\frac{3}{2}\frac{Fr^{11/3}}{(Fr^2 - 1)} \tag{1.16}$$

where

$$R = \left[\frac{r}{\frac{8\,Q^2}{c_f^3\,g}}\right]^{1/3} \tag{1.17}$$

Integration of this equation gives

$$\frac{1}{4}Fr^{-8/3} - Fr^{-2/3} = -R + c \tag{1.18}$$

To evaluate the integration constant, the Froude number must be specified at one location in the flow. The methodology of the present analysis is somewhat similar to Fanno flow analysis of one-dimensional compressible flow with friction. For Fanno flow, it is customary to evaluate the integration constant at a critical location where the Mach number is unity. It is assumed that a critical location exists in the flow field. Let Fr = 1 at a location where $R = R^*$.

Substituting this in eqn. (1.18) and rearranging gives

$$R - R^* = (Rr^{-2/3} - 1) - 1/4(Fr^{-8/3} - 1) \tag{1.19}$$

Equation (1.19) is a double-valued function as shown in Fig. 1.3. The two stems of the function represent subcritical and supercritical flows where the Froude number is less and greater than unity, respectively.

Since two solutions exist at any location, the possibility of a sudden jump from supercritical to subcritical flow exists. The opposite is not true since that would violate the second law of thermodynamics. The height of the film before and after the jump can be related by the conservation of mass and momentum across the jump. For plane flow this is given by

$$\frac{h_2}{h_1} = \frac{1}{2}\left[\sqrt{1 + 8\,Fr_1^2} - 1\right] \qquad (1.20)$$

where subscript 1 indicates conditions before the jump and subscript 2 indicates conditions after the jump.

(b) Axisymmetric Radial Flow

For radial flow, K = 1, so eqns. (1.14) and (1.15) can be transformed into the following form

$$\frac{dFr}{dR} = \frac{Fr\,(2 + Fr^2)}{2R\,(Fr^2 - 1)} - \frac{3Fr^{11/3}\,R^{2/3}}{2\,(Fr^2 - 1)} \qquad (1.21)$$

where

$$R = \frac{r}{\left[\dfrac{2Q^2}{\pi^2\sqrt{g}\,c_f^3}\right]^{1/5}} \qquad (1.22)$$

The radial distance has been non-dimensionalized in terms of other flow parameters. An analytical solution for eqn. (1.21) is not possible, so a numerical integration was performed using the Euler method. It can be noticed that the equation is singular at Fr = 1. Therefore, the critical condition cannot be directly applied as a boundary condition in the numerical solution. To avoid this singularity, the equation can be expanded around the singular point and the solution can be found at a short distance from the singular point from the lowest-order expansion. The numerical integration was then carried out beginning from a short distance away from the singular point, where the solution is already known. The solution is shown in Fig. 1.4.

It should be noted that the critical radius, R^*, appears as a parameter. Also, the shape of the curve in somewhat different from that for plane flow. This is because the flow spreads out as it propagates radially downstream. The double-valued nature of the solution still remains in radial flow which indicates the possibility of a hydraulic jump.

1.4.3 Characteristic Behavior of the Flow

Since the equations of transport in a thin film are somewhat similar to those for one-dimensional compressible flow, it may be useful to analyze the characteristic behavior of the flow.

The conservation equation in its time-dependent form can be written as

$$\frac{\partial U}{\partial t} + \frac{1}{r^K} \frac{\partial}{\partial r} \left(r^K E \right) = H$$

where

$$U = \begin{vmatrix} h \\ hW \end{vmatrix}, \quad E = \begin{vmatrix} hW \\ h(W^2 + \frac{gh}{2}) \end{vmatrix}$$

and $$H = \begin{vmatrix} 0 \\ \tau_w/\rho \end{vmatrix}$$

where τ_w is the surface shear stress. These are two first-order ordinary differential equations in t and r with two dependent variables, h and W.

Expressing the equations in the characteristic form results in the following equation

$$R_t + C R_x = S$$

where

$$R = \begin{vmatrix} W + \sqrt{gh_1}\,\frac{h}{h_1} \\ W - \sqrt{gh_1}\,\frac{h}{h_1} \end{vmatrix} = \text{Riemann invariants}$$

$$C = \begin{vmatrix} W + \sqrt{gh_1} \\ W - \sqrt{gh_1} \end{vmatrix} = \text{Wave speed}$$

It can be seen that the first invariant always propagates downstream. The second invariant, however, propagates downstream for supercritical flow (Fr = $W/\sqrt{gh_1} > 1$) and propagates upstream for subcritical flow (Fr < 1). This implies that both W and h must be prescribed upstream for supercritical

flow while only one is prescribed upstream and one downstream for subcritical flow. This analysis will assist in determining the appropriate location of the boundary conditions for the computations addressed in the following sections.

1.5 Numerical Solution Procedure

The governing transport equations along with the appropriate boundary conditions were solved numerically using a finite-difference scheme. Since the free surface geometry cannot be handled very well with a regular rectangular or cylindrical coordinate system, a boundary-fitted curvilinear coordinate system had to be used. In this system, the free surface of the film was used as one of the boundaries of the control volume.

A curvilinear system can be either orthogonal or non-orthogonal depending on whether the faces of the control cells are orthogonal to each other or not. The orthogonal system has the advantage of simplicity compared to the non-orthogonal system. In either system, the vectorial form of the governing equations [i.e., eqns. (1.1) and (1.2)] can be written in terms of components and can be discretized to determine the finite-difference equations. In most of the computations presented, the coordinate system was non-orthogonal.

Within the range of the general non-orthogonal coordinate system there exist several options in formulating the equations. These options arise from the freedom available in the choice of velocity components and their direction with reference to the coordinates. Thus, velocity and force vectors can be resolved either into their Cartesian, covariant or

contravariant components. Moreover, the problem can be solved in a physical domain or transformed into a domain where the grid cells are rectangular and other physical quantities are non-dimensional or reduced in dimension. Although all these options are obviously equivalent to each other from the physical point of view, they are substantially different as far as numerical treatment is concerned, each presenting its own problems. Some of these problems are highlighted in the paper by Galea and Markatos [10] and are discussed briefly below.

The resolution of the velocity and other vectors into Cartesian components is possibly the simplest approach, but this leads to an inaccurate numerical formulation, in particular for the pressure gradient term driving the flow. The use of contravariant components makes the formulation of convective terms straightforward, but still does not solve the problem of accurately formulating the pressure gradient and does not help with respect to properly assigning the value of the velocity convected into the distorted grid cell. The use of covariant components solves the two problems above, but leads to more complicated calculations for the convective terms. In the present study, the problem was solved in the physical domain where covariant velocity components were used.

The grid system used can be considered as a distorted version of the usual orthogonal Cartesian grid system in which grid lines and control cells are stretched, bent and twisted in a arbitrary manner, subject to the cells retaining their topologically Cartesian character. This means that grid cells always have six sides and eight corners in a three-dimensional case.

As shown in Fig. 1.1, the local coordinates are defined along lines joining adjacent cell centers. The z-axis was taken in the stream line direction and y-axis in the direction across the film. The resolutes of the velocity vectors in the y and z directions are v and w, respectively, and can be defined as

$$v = \vec{V} \cdot \vec{j}$$

$$w = \vec{V} \cdot \vec{k}$$

Here $\vec{j}$ and $\vec{k}$ are unit vectors in the direction of the coordinate axes. In general, the resolutes are not the same as the velocity components in these directions, but can be related to them by geometrical factors.

The finite difference equations were derived by the application of the conservation principle of mass and momentum to the grid cells. The transport processes for each cell are convection and diffusion. Moreover, there may be a momentum or mass source within the cell. The mass flux across a cell boundary was computed exactly from the scalar product of the velocity vector and the vector representing the area of the cell face. Note that this can be written out in terms of velocity resolutes and geometrical factors including angles between cell faces. In the calculation of convection across a cell face, special attention was given to the change of orientation of the coordinate axes from cell to cell and the curvature of a cell face. These resulted in extra terms in the calculation of convection. However, the representation of convection was

exact and did not involve any approximation due to the non-orthogonality of the grids.

The calculation of diffusion is somewhat more complicated than convection. The diffusion flux was calculated assuming the coordinate system to be locally orthogonal. This obviously neglects cell curvature and non-orthogonal orientation and may incorporate a substantial amount of error where the process is primarily diffusive. However, in the thin film calculation this approximation should not introduce severe inaccuracies, particularly when the film enters the control volume with a reasonably high velocity.

The relative importance of convection and diffusion at each cell was determined from the magnitude of the local Peclet number. A hybrid difference scheme demonstrated by Patankar [11] was used. The calculation of the momentum source due to the pressure gradient and that due to the gravitational body force could be accomplished without any approximation for non-orthogonality.

The grid generation was achieved in two steps. First, the grid cells were formed by algebraic interpolation between the boundary points. This provided an approximately equal volume for each control cell. The boundaries for the interior cells were then smoothed to make the cell faces more orthogonal to each other. This operation resulted in a better representation of diffusion in the flow field and more accurate computations. The details of the formulation in a body-fitted coordinate

system and the generation of grid cells are described in the work by Spalding et al. [12].

The number of grids in the y-z plane was determined from a series of computations with different grid sizes. A sample of this investigation is shown in Fig. 1.5 where the free surface profile for radial flow under zero gravity is plotted. It can be seen that the free surface profile is somewhat sensitive to the grid size. The solution obtained by using 20 x 20 grids is somewhat different from that obtained with 40 x 20 grids in z-y directions. The differences become smaller when the 40 x 20 solution is compared with the 50 x 25 solution. Finally, the difference completely disappears when the solution corresponding to 50 x 25 grids is compared with the 55 x 27 solution. Therefore, 50 grids in the direction of flow and 25 in the direction across the film was found to be adequate and was used for all radial flow computations. For plane flow, it was found that the solution corresponding to 40 x 20 grids in the z-y plane precisely predicts the friction coefficient and velocity profile in a falling film system. Therefore, further refinement of the grids appeared to be unnecessary and all computations for plane flow were carried out using 40 x 20 grids except for case P2, which involved a complex free surface profile. For this case 50 x 25 grids were used.

The flow field was solved by using SIMPLEST algorithm as discussed by Spalding [13]. One special feature of this algorithm is that in the discretized form of the momentum equation, the convection terms are lumped together with the source term. This results in a faster convergence for some flow conditions. The algorithm works in an iterative manner where the

continuity equation is transformed and used as a pressure correction equation. The computation starts by guessing a pressure field. This is used to determine velocity components from their corresponding momentum equations. The modified continuity equation is then used to determine the amount of pressure correction. The guessed pressure, the amount of pressure correction and the solution corresponding to the momentum equations are then assembled together to give the flow rate and pressure field for that step. The new pressure serves as a guess for the next step. The solution proceeds across the control volume until the normalized residual for each equation was approximately 10^{-6}. The above finite-difference formulation and solution procedure is incorporated in computer program PHOENICS that was used in the present study. In the free surface flow discussed here, both the zero-shear condition and the $p = 0$ condition at the free surface need to be satisfied. These two conditions cannot be simultaneously given at a boundary. On the other hand, the free surface geometry, which is unknown in the problem has to be given before solving the flow field by a finite-difference method. To avoid this difficulty, an iteration scheme has been adapted as described below.

(1) Guess a free surface profile.

(2) Solve the flow field completely for that profile using the zero-shear condition on the free surface boundary.

(c) Find the pressure distribution on the free surface and calculate its deviation from an ideal zero-pressure free surface. The measure used here is the RMS (root-mean-square) error.

(d) Calculate and reduce the RMS error on the free surface by successive alteration of the surface profile.

(e) The results with the minimum error give the required final solution.

The accuracy of the computation depends somewhat on the assumption of the form of free surface. In the results presented here, hyperbolas with two or more degrees of freedom were used to represent the computation domain.

1.6 Results and Discussion

1.61 Plane Film

The flow of a plane film along a vertical wall under the influence of gravity is a classical fluid mechanics problem where an analytical solution is available for fully-developed laminar flow. In the fully-developed region, the film height remains constant and the velocity profile has a parabolic appearance. Numerical computations using the present methodology were performed for a film which has already reached the fully-developed condition. A parabolic velocity profile with the same shape as given by the analytical solution was used for the incoming fluid. The Reynolds number for the film was Re = 50 where water was used as the fluid. It was found that for the entire domain, the velocity profile across the film remains about the same and the friction coefficient was equivalent to that of the analytical solution. In the present investigation, the friction coefficient is defined as

$$c_f = \frac{\tau_w}{\frac{1}{2}\rho W^2} \tag{1.23}$$

where W is the average velocity of the fluid across the film. This definition is applicable for both plane and radial flow. For plane flow with constant thickness, W is a constant because of continuity.

The distribution of pressure on the free surface was also computed and the RMS error was determined to be 0.18 Pa. This non-zero figure of RMS error may be attributed to the inaccuracy associated with the representation of flow field by finite-difference equations. This amount of error cannot be avoided in a numerical solution, so it provides a lower bound on the error that can be expected in thin film computations.

The developing flow of a falling film when introduced at a height equal to, or above or below the equilibrium height was also investigated. The flow conditions are summarized in Table 2 and the results are shown in Table 3 and Figs. 1.6-1.9. When the film enters the control volume at the equilibrium height, the height remains the same and the development of the velocity profile from uniform to parabolic occurs as the flow moves downstream. When the film enters with a height other than the equilibrium height, a gradual adjustment of height takes place until the flow reaches the equilibrium height. The adjustment of the free surface and the development of the velocity profile occur simultaneously in this flow. To model the free surface, we have assumed a profile of the form

$$h = \begin{cases} h_{in} \left(1 + \frac{z}{A} \right)^{an} & , \text{ for } z < z_1 \\ \delta & , \text{ for } z \geq z_1 \end{cases} \qquad (1.24)$$

The first part of this profile provides the variation of the free surface

height in the developing flow region and the second part gives the height after the adjustment is completed. The downstream location where the free surface adjustment is complete is z_1.

For the computation with $h_{in} = \delta$, we find that the RMS error on the free surface condition is 1.2 Pa. The uniform entrance condition provides a higher RMS error than the parabolic entrance since a developing flow region is present where the pressure has to conform with the flow development. An error of this order may be acceptable for a free surface computation since no variation of height is expected to take place when a film is introduced at the equilibrium height. The distance required for flow development was found to be about 5 times the film thickness in this case. A flow is defined to be fully-developed when the wall shear stress is within 2 % of the final equilibrium value. This definition is similar to that given by Kays and Crawford [14] for developing flow in closed conduits.

As evident from Fig. 1.6 the adjustment of film height takes places for a length of 0.006 m (i.e., approximately 10δ) when a film is introduced at a height 20% more than the equilibrium height. In this situation the velocity profile also becomes fully-developed at the same location. A film introduced at a height 20% lower than the equilibrium is found to take a shorter distance for the adjustment of the free surface and the velocity profile. The distribution of the free surface pressure is shown in Fig. 1.7. It can be noticed that most of the pressure variation takes place in the developing flow region and its value becomes very close to zero when the flow becomes fully developed. The RMS error in pressure

is small in all cases which indicates that modeling the free surface with an equation of the form of eqn. (1.24) is reasonably accurate.

The variation of the friction coefficient along the length of the film is shown in Fig. 1.8. The distributions for $h_{in} = \delta$ and $h_{in} = 0.8\delta$ are very close to each other, but for $h_{in} = 1.2\delta$ the variation is significantly different. The friction coefficient first decreases to a value lower than that for the equilibrium condition and then rises up to the equilibrium value. This is due to two counter-acting phenomena that affect the film in the developing flow region in this case. The wall friction propagates outward as the boundary layer develops beginning from the entrance point which tends to reduce the velocity of the fluid. The thickness of the film, however, decreases and tends to increase the fluid velocity due to the area available for the flow. Since the first effect starts from the wall, it is more dominant in the earlier part of the flow development and then the second effect takes over in the region downstream. It can also mentioned that when the film is introduced below the equilibrium height, the increase in the film height and the propagation of the shear tend to reduce the film velocity, so the behavior is not analogous to the case when the film is introduced above the equilibrium height. In all situations, a plane falling film eventually attains a fully-developed flow. This is confirmed by comparison of the velocity profile in a location near the exit as shown in Fig. 1.9. The variation of the velocity and the friction coefficient are identical in all situations.

The flow of a plane film was also investigated for a horizontal orientation of the plate where the gravity acts across the thickness of the

film instead of in the direction of the main flow. The flow conditions used here are listed in Table 2 and the corresponding free surface geometry is described in Table 3. Figs. 1.10-1.13 present the computational results.

In Fig. 1.10 it can be seen that after the film enters the control volume, the liquid film height increases rapidly within a short distance until it is about 4 times the inlet height. The film height then levels off slowly as the flow moves downstream. Close to the exit the height decreases to accommodate the outlet boundary condition. In this case, the inlet Froude number is 3.0 which means that the flow enters the control volume at a supercritical condition. The transition of the flow from supercritical to subcritical takes place with a rapid change in fluid level. Once the subcritical condition is established, the change in height is basically due to the deceleration of the flow by friction at the wall. Figure 1.10 also shows the results obtained by Thomas [15] for a one-dimensional model of the flow under the same flow conditions. This result was obtained by numerical integration of the subcritical and supercritical streams proceeding from the end points and matching the conditions at the jump location. The one-dimensional solution seems to be quite different from the two-dimensional flow considered here, particularly in the subcritical region. It appears to be quite strongly influenced by the downstream boundary condition whereas in the two-dimensional case the influence is less dramatic. A computation using the present numerical scheme where the free surface was forced to take the form obtained by Thomas [15] showed a RMS error of 21.62 Pa on the free surface pressure, which is about 10 times the RMS error in our final solution, as listed in

Table 3. Therefore, the free surface profile predicted by the 2-D solution is likely to be much more accurate than that predicted by the 1-D solution.

The distribution of the flow velocity across the thickness of the film is shown in Fig. 1.11 for two locations on the plate. The velocity profile is parabolic in nature. Even though the average velocity decreases downstream, the local velocity may increase or decrease depending on the location across the film thickness. In the numerical results, it was also seen that there is a separated flow region around the location of the jump. To cope with the rapid rise of the fluid level, flow separation occurs near the wall, which reattaches again at a downstream location. The profiles shown here correspond to locations beyond the reattachment point. Inside the recirculating flow region, the fluid moves in a direction opposite to the main flow at locations adjacent to the wall. Even though the velocity is positive at all locations after reattachment, the acceleration of the fluid near the wall continues for a distance as seen in Fig. 1.11.

The shear stress exerted by the wall and the corresponding friction coefficient are shown in Figs. 1.12 and 1.13, respectively. The wall shear stress decreases rapidly after the entrance, which is due to the simultaneous adjustment of the film height and the development of the velocity profile from uniform entrance conditions to a two-dimensional form. Both effects aid to a decrease in the shear stress. The shear stress is negative in the recirculating flow region and becomes positive again after reattachment. The two locations corresponding to zero shear are the separation and reattachment locations. In Fig. 1.12, it can be also noted that the wall shear becomes constant at an intermediate location

of the flow and rises again near the exit. The increase in the wall shear stress and the friction coefficient are due to an increase in flow velocity near the wall as the exit is approached.

The remaining part of the investigation concerning plane film flow is the flow of a film under zero gravity. In this situation the orientation of the plate become immaterial and an identical flow condition is achieved if the plate is horizontal, vertical or inclined. Consider a situation where the film is introduced at a height equal to the equilibrium fully-developed flow in a falling film system. In the absence of gravity, the flow is acted on only by viscous and inertial forces and the film height is expected to increase downstream. To model the free surface, we assume a profile of the form given in Table 2. The flow conditions are also listed in the same table. The results are shown in Table 3 and Figs. 1.14-1.18.

Figure 1.14 shows the variation of the film height with distance which increases monotonically. The figure also shows the analytical solution derived in the previous section. The analytical solution requires the specification of a friction coefficient. In the present investigation it was taken from the numerical solution instead of assuming it to be constant throughout the region. The comparison between the analytical and numerical solutions appears to be good in most regions of the flow.

The variation of the free surface pressure is shown in Fig. 1.15. Analogous to the falling film flow, most of the pressure variations occur in regions close to the entrance where the development of the velocity from

a uniform to parabolic profile takes place, which is analogous to the falling film flow. However, in contrast to the falling film, the velocity keeps changing as the flow moves downstream and never attains a fully-developed situation. To illustrate this point, the velocity profile at three different locations on the plate are plotted in Fig. 1.16. Even though the profile becomes parabolic in nature, the magnitude of the velocity decreases continuously. The shear stress exerted by the solid wall is shown in Fig. 1.17 and the corresponding friction coefficient is plotted in Fig. 1.18. It can be noticed that the shear stress decreases continuously as the flow moves downstream, whereas the friction coefficient has a minimum at an intermediate location and then increases downstream. The largest variations of the shear stress occur close to the entrance due to the development of the velocity from a uniform to a parabolic profile. After the velocity profile is parabolic, the slight reduction in the shear stress is due to the deceleration of the flow, which is small compared to the reduction of the average velocity in regions away from the entrance. This results in an increase in the friction coefficient.

1.6.2 Radial Film Flow

The system where a fluid is introduced at the center of a circular horizontal plate and spreads uniformly in all radial directions was also studied. Two combinations of flow rates and initial film heights were chosen and water was used as the fluid. These cases were studied for zero-gravity ($g = 0$) and normal gravity ($g = 9.81\ m/s^2$) situations. The effect of critical outflow as may happen at the exit of the plate was studied for one case. The flow parameters for different cases studied here are shown in Table 4. The surface profile and corresponding RMS error for

the surface pressure for different cases are listed in Table 5. The constants appearing in each profile equation were optimized to give the minimum possible error in the free surface pressure. The values appearing in Table 5 are optimum values corresponding to each flow configuration. It can be noticed that all RMS errors are on the order of 1 Pa, so the solutions may be considered to be acceptable.

Figure 1.19 shows the variation of the film height with the radial distance for cases R1A and R2A. These cases correspond to the same flow rate and inlet film height but the gravitational acceleration for R1A is g = 0.0 and for R2A is g = 9.81 m/s^2. The one-dimensional analytical solutions, as discussed in a previous section, corresponding to these cases are also shown in the figure. The analytical solution requires the specification of a friction coefficient which was taken to be the average friction factor in the numerical solution. The comparison between the 1-D and 2-D solutions appears to be quite reasonable. In the derivation of the one-dimensional solution it was assumed that the film has a uniform velocity across its thickness, whereas in reality the film has a parabolic velocity profile as seen in Fig. 1.20. This assumption, along with the assumption of a constant friction coefficient may be the primary reasons for the difference between the 1-D and 2-D solutions.

Comparing the film height for the case R1A with that for the case R2A, it can be seen that gravity has very significant effect in determining the flow behavior of the film at this flow rate. In the absence of gravity, the film height gradually decreases in the downstream direction, whereas when g = 9.81 m/s^2, the film height slightly increases as the flow proceeds

downstream. In the absence of gravity, there is no static pressure gradient across the thickness of the film and the momentum balance in the film is solely due to inertial and viscous effects. The pressure variation is significant for a film of moderate thickness which tends to flatten out the free surface.

The variation of velocity across the film thickness is shown in Fig. 1.20 for two different locations. The profile remains parabolic but its magnitude decreases downstream due to the increase in area available for the flow. The decrease is less dramatic for the zero gravity case since the film height also decreases downstream. The distribution of free surface pressure for the two cases are plotted in Fig. 1.21. Figures 1.22 and 1.23 show the variation of the wall shear stress and the friction coefficient at this rate of flow, respectively. The largest variations of these quantities appear to be in regions close to the inlet. This is primarily an outcome of the development of the velocity profile from uniform at entrance to parabolic in downstream locations. For case R2A, the wall shear decreases downstream, which is expected since the velocity of the fluid decreases and consequently encounters less resistance from the wall. In case R1A, however, the wall shear stress increases slightly at locations far downstream. This is due to the local acceleration of the flow in the region next to the wall. It may be pointed out that even though the velocity profile is parabolic, the actual shape of the parabola changes along the plate. This is caused by the increase of the local velocity next to the wall. The increase of the friction coefficient for cases R1A and R2A is primarily caused by a decrease of the average velocity as the fluid moves downstream.

Figures 1.24-1.28 demonstrate the behavior of the flow when the film is introduced at a smaller height and flow rate. As in the previous two cases, case R1B and R2B correspond to identical flow and boundary conditions, but the gravitational acceleration in case R1B is g = 0.0 and in case R2B is g = 9.81 m/s^2. Case R2C is an extension of case R2B where the film at the exit is forced to have a Froude number of Fr = 1. When the radius of the plate is finite and ends at the exit of the computation domain, the fluid spreads over the plate and then free falls over the edge of the plate. For a free-falling exit situation, a subcritical flow (Fr < 1) has to transform to a supercritical flow (Fr > 1) at the discharge location. To incorporate this effect, the Froude number at the edge of the plate is set to Fr = 1, which corresponds to critical flow. Cases R1B and R2B does not take into account this effect and the plate is assumed to extend somewhat beyond the end of the computation domain.

The film height for the three different cases are shown in Fig. 1.24. The analytical solution corresponding to case R2B is shown here for comparison. At this condition, the fluid rises up and forms a hydraulic jump close to the entrance. The shape of the free surface and its maximum height depend on the gravitational body force and exit boundary condition. In case R1B, which corresponds to a situation where g = 0.0, the increase of the fluid level is about 10% more than the other two cases when g = 9.81 m/s^2. The presence of gravity, which causes a pressure gradient across the thickness of the film, tends to flatten out the free surface profile. It is also evident that a sudden rise of the flow occurs when gravity is present which contrasts the gradual increase of the fluid level when g = 0.0. After the jump, the height of the film slowly decreases as the fluid

proceeds further downstream. In case R2C, when the outlet is constrained to have Froude number of Fr = 1, the film maintains about the same thickness for the most regions of the plate and suddenly drops very close to the exit. In Fig. 1.24, it can be also noticed that the height and location of the jump is the same for both cases R2B and R2C. This may suggest that the jump height is determined by the flow rate and Froude number before the jump, rather than conditions at the outlet. The conditions of the flow after the jump, however, depend on the exit conditions as evident from the shape of the free surface. This observation is consistent with an open channel flow where the flow rate and Froude number before the jump determine the height after the jump, and the fluid motion downstream is subcritical and affected by the outlet condition.

Figure 1.24 also shows the analytical solution corresponding to one-dimensional radial flow in the presence of gravity. The solution requires the specification of the friction coefficient and one boundary condition. The friction coefficient used here is 2.0, which is the average value after the jump as obtained in the numerical solution corresponding to case R2B or R2C. When the inlet condition is used as the boundary condition, the analytical solution predicts a jump to a height close to that of the numerical solution and the film height diminishes slowly thereafter. The figure also shows the film height when the exit boundary condition corresponding to case R2B is used. The solution shows that the film height gradually increases in the upstream direction, but no drop in fluid level is obtained near the inlet. This behavior of the analytical solution reaffirms the previous observation that the exit boundary condition in the subcritical region cannot influence the supercritical flow

before the jump. The numerical solution is between the two analytical solutions. The one-dimensional solution does not account for the details of the behavior of the flow like separation after the jump and the parabolic velocity profile thereafter. The difference between the analytical and numerical solutions may be attributed to these fine details of the flow field.

The velocity profile across the film at two radial locations are shown in Fig. 1.25. The velocity profile appears to be parabolic at each location both in the presence and absence of gravity. The magnitude of the velocity at $z/z_m = 0.8$ is less than that at $z/z_m = 0.4$ due to the larger area available for the flow. At a particular location, the velocity is greater for the case of $g = 9.81\ m/s^2$ than the corresponding zero-gravity case. This is because of the smaller film thickness in the presence of the gravitational field at this flow rate. The free surface pressure for the three cases studied here are shown in Fig. 1.26. The pressure at intermediate locations become very close to zero. There are some fluctuations close to the inlet and the exit for the case R2C. This is due to the rapid change of the flow in these regions to account for the imposed boundary conditions. The assumed form of the free surface profile may not be very precise in these regions. A more complex profile assumption with a larger number of degrees of freedom may smooth out these pressure fluctuations. However, the profiles used in the present investigation are reasonably simple to handle in computation and capture the most significant structures of the flow and yield solutions that are physically realistic and accurate enough for engineering applications. Therefore, it is preferable to use a rather simple free surface profile rather than making

it very general to fit all regions of the flow. It should be also mentioned that the present free surface profiles were also arrived at after a number of trials with different parabolas, hyperbolas and polynomials for each case studied and the form selected was found to be the most accurate and general.

The wall shear stresses and friction coefficients for cases R1B, R2B and R2C are plotted in Figs. 1.27 and 1.28. In case R1B, which corresponds to g = 0.0, the shear stress is positive and high near the entrance. At a location downstream, it becomes negative and then rises up to positive values again and diminishes slowly thereafter. The negative value of shear stress is due to separation of the flow after the jump. It becomes positive again when the flow reattaches, and assumes a parabolic profile. The small decrease in the magnitude of shear stress as the flow moves further downstream is due to the gradual expansion of the flow because of the area change. In cases R2B and R2C, the shear stress starts with a negative value, rises up to a positive value at a location downstream and slowly diminishes thereafter. In these cases, the jump occurs immediately downstream from the entrance and results in flow separation in that region. It may be noticed that the value of shear stress is slightly different near the entrance for cases R2B and R2C. In case R2B a uniform velocity profile was assumed at the entrance, whereas in case R2C a parabolic velocity profile was assumed. Even though both profiles become distorted due to flow seperation, the magnitude of the wall shear stress is somewhat affected by the entrance condition. The separation of the flow results in a very complex distribution of the friction coefficient near the entrance as seen in Fig. 1.28. After the flow reattaches to the surface, the

friction coefficient gradually increases downstream. It may be recalled that the friction coefficient in the present investigation is defined in terms of the local velocity. The gradual decrease of the local average velocity as the fluid spreads downstream overpowers the loss of wall shear stress and increases the friction coefficient downstream.

1.7 Conclusions

The present study developed a numerical solution procedure for the computation of plane or radial thin film flow in a normal or zero gravity environment. An analytical solution was also derived for a one-dimensional approximation of the flow. A reasonable agreement between the numerical and analytical solutions was obtained for most flow configurations considered here.

Five different flow systems were studied: (a) plane falling film, (b) plane flow on a horizontal plate, (c) plane flow under zero gravity, (d) radial flow on a horizontal plate, and (e) radial flow under zero gravity. For plane falling films, an equilibrium fully-developed region is present where the gravitational body force is balanced by the viscous shear force at the wall. The film, whether introduced at the equilibrium height or at a height above or below the equilibrium, eventually comes to this fully-developed condition. In the fully developed region the numerical velocity profile, which is parabolic, matched exactly with the analytical solution irrespective of the entrance condition of the film. When a film is introduced at its equilibrium height and with the same velocity profile as that of fully-developed flow, no further change in the velocity distribution is found to happen as the film proceeds downstream. This

gives confidence in the stability and accuracy of the present numerical scheme. The error on the estimation of the free surface pressure in this case is the minimum that cannot be avoided in a numerical computation. An estimate on the error bound of the free surface pressure was developed from the calculation of developing flow and it was concluded that an error of the order of 1 Pa may be acceptable. The length of the developing region was found to be small. Both the free surface height and velocity profile appeared to arrive at the equilibrium condition within 10 times the equilibrium film thickness. The length was found to be relatively larger when the film begins with a height above the equilibrium height.

For plane flow on a horizontal plate it was found that the film height increases rapidly and forms a hydraulic jump. The flow regime changes from the supercritical entrance condition to a subcritical downstream condition. The analysis of the flow indicated that both supercritical and subcritical flow proceed towards a critical flow when friction is present. The sudden rise of the fluid level resulted in flow separation adjacent to the solid wall. The flow reattached again at a downstream location and developed a parabolic velocity profile. The location of separation and reattachment could be determined from a plot of shear stress at the wall, which vanishes at these locations.

For a plane flow under zero gravity it was found that the film thickness monotonically increases as the flow moves downstream. The velocity profile is parabolic except for regions very close to the entrance. The shear stress at the wall decreases as the flow moves downstream. The friction coefficient was computed in terms of the local

average velocity and was found to increase after coming to a minimum at an intermediate location on the plate.

For radial flow, computations were performed for two sets of flow rates and inlet heights. The behavior of the flow was found to depend significantly on the flow rate and magnitude of the gravitational acceleration. At the higher flow rate, it was found that the film decreases in thickness downstream under zero gravity whereas the thickness increases downstream when the gravitational acceleration is $g = 9.81\ m/s^2$. The velocity profile was parabolic in most regions, even though the shape of the profile changed as the flow moved downstream. The change here was more severe than plane flow since the area available for the fluid increased downstream. For zero gravity it was found that the wall shear at locations far downstream increased due to the local acceleration of fluid near the wall.

When the film thickness at the inlet is low and the Froude number is greater than unity, the flow jumped up within a short distance from the entrance and remained subcritical downstream. The jump happened at the same location and height whether or not the Froude number at the exit was $Fr = 1$. The flow after the jump was affected by the outlet condition. For the same flow condition when the gravitational acceleration is reduced to zero, it was found that the rise in fluid level still occurs, even though the rise is more gradual and to a greater height than the corresponding jump case. The jump or rise in fluid level was also found to be associated with flow separation. The flow was found to reattach to the surface and form a parabolic profile after the jump. After the

reattachment, the wall shear stress slightly decreased as the flow moved downstream, irrespective of whether or not gravity was present. For radial flow, the friction coefficient was found to increase downstream in regions somewhat away from the entrance and flow separation.

1.8 References

1. Bird, R.B., Stewart, W.E., and Lightfoot, E.N., 1960, Transport Phenomena, John Wiley and Sons, N.Y.

2. Faghri, A., and Payvar, P., 1979, "Transport of Thin Falling Liquid Films," Reg. J. Energy Heat Mass Transfer, Vol. 1, No. 2, pp. 153-173.

3. Watson, E.J., 1964, "The Radial Spread of a Liquid Jet Over a Horizontal Plane," J. Fluid Mechanics, Vol. 20, Part 3, pp. 481-499.

4. Rauscher, J.W., Kelly, R.E., and Cole, J.D., 1973, "An Asymptotic Solution for the Laminar Flow of a Thin Film on a Rotating Disk," ASME J. Applied Mechanics, Vol. 40, No. 1, pp. 43-47.

5. Murthy, V.N.D., 1976, "Combined Laminar and Turbulent Flow Over a Rotating Disk," Indian J. Technology, Vol. 14, pp. 107-112.

6. Nusselt, W., 1916, "Die Oberflächen Kondensation des Wasserdampfes," Zeitschrift des Vereines Deutscher Ingenieure, Vol. 60, pp. 541-569.

7. Sparrow, E.M., and Gregg, J.L., 1959, "A Theory of Rotating Condensation," ASME J. Heat Transfer, Vol. 81, No. 2, pp. 113-120.

8. Butuzov, A.I., and Rifert, V.F., 1972, "An Experimental Study of Heat Transfer During Condensation of Steam at a Rotating Disk," Heat Transfer-Soviet Research, Vol. 4, No. 6, pp. 150-153.

9. Butuzov, A.I., and Rifert, V.G., 1973, "Heat Transfer in Evaporation of Liquid From a Film on a Rotating Disk," Heat Transfer-Soviet Research, Vol. 5, No. 1, pp. 57-61.

10. Galea, E.R., and Markatos, N.C., 1987, "Prediction of Fire Development in Aircraft," Proc. 2nd Int. PHOENICS User Conference, London.

11. Patankar, S.V., 1980, Numerical Heat Transfer and Fluid Flow, Hemisphere Publishing Corporation, N.Y.

12. Spalding, D.B., Rosten, H.I., Glynn, D.R., Malin, M.R., and Edwards, J.P., 1986, "Lecture Panels for Use of the Body-fitted Coordinates in PHOENICS," CHAM TR/126, Concentration Heat and Momentum Ltd., London.

13. Spalding, D.B., 1980, "Mathematical Modeling of Fluid Mechanics, Heat Transfer and Chemical Reaction Processes," A Lecture Course, CFDU Report, HTS/80/1.

14. Kays, W.M., and Crawford, M.E., 1980, Convective Heat and Mass Transfer, McGraw-Hill, N.Y.

15. Thomas, S., 1988, "Computation of Plane and Radial Hydraulic Jumps," Research Report, Mechanical Systems Engineering Department, Wright State University, Dayton, Ohio.

16. Rosten, H.I., and Spalding, D.B., 1987, The PHOENICS Beginner's Guide, CHAM TR/100, Concentration Heat and Momentum Ltd., London.

Nomenclature

A Optimization parameter in free surface equation, flow parameter (defined by eqn. (1.10))

an Optimization parameter in free surface equation

bn Optimization parameter in free surface equation

C Optimization parameter in free surface equation, wave speed

c_f Friction coefficient

Fr Froude number, $W/\sqrt{gh}$

g Acceleration due to gravity

h Film height

h_{in} Inlet film height

h_{out} Film height at exit

p Static pressure

t Time

K Exponent for eqn. (1.3)

Q Flow rate

r Radial coordinate

r^* Radial location for critical flow

Re Reynolds number, $4Q/\nu$

R Riemann invariant, dimensionless radial coordinate (eqns. (1.17) and (1.22))

R^* Critical radius (dimensionless)

v Normal component of velocity

$\vec{V}$ Velocity vector

w Component of velocity along the plate

W Average velocity along the plate

y Coordinate normal to main flow direction

ym Maximum value of y

z Coordinate along the plate

zm Maximum value of z

z_1 Optimization parameter in free surface equation

z_2 Optimization parameter in free surface equation

Greek symbols

ρ Density

μ Dynamic viscosity

τ_w Shear stress at wall

δ Equilibrium film thickness

ν Kinematic viscosity

List of Tables

Table 1: Boundary Conditions for Plane and Radial Flow

Case P1:	at $y = 0$:	$v = w = 0$
	at $y = h$:	$\frac{\partial w}{\partial y} = 0, \quad v = 0, \quad p = 0$
	at $z = 0$:	$\begin{cases} w = W_{in}, \text{ for uniform entrance} \\ w = 1.5\, W_{in} \left[2(\frac{y}{h}) - (\frac{y}{h})^2 \right], \text{ for parabolic entrance} \end{cases}$
	at $z = L$:	$p = 0$
Cases P2	at $y = 0$:	$v = w = 0$
and P3:	at $y = h$:	$\frac{\partial w}{\partial y} = 0, \quad v = 0, \quad p = 0$
	at $z = 0$:	$w = W_{in}$
	at $z = L$:	$p = \rho g\,(h-y)$
Cases R1	at $y = 0$:	$v = w = 0$
and R2:	at $y = h$:	$\frac{\partial w}{\partial y} = 0, \quad v = 0, \quad p = 0$
	at $z = r_{in}$:	$\begin{cases} w = W_{in}, \text{ for uniform entrance} \\ w = 1.5\, W_{in} \left[2(\frac{y}{h}) - (\frac{y}{h})^2 \right], \text{ for parabolic entrance} \end{cases}$
	at $z = r_{out}$:	$p = \rho g\,(h-y)$

Table 2: Flow Conditions: Plane Flow

General data: $\rho = 913.026\ kg/m^3$

$v = 7.432 \times 10^{-6}\ m^2/s$

Case P1A: $h_{in} = 0.000595\ m$

$W_{in} = 0.1561\ m/s, \quad g = 9.81\ m/s^2$

Free surface profile: $h = \delta$, where $\delta = 0.000595\ m$

Case P1B: $h_{in} = 0.000714\ m\ (1.2\delta)$

$W_{in} = 0.1301\ m/s, \quad g = 9.81\ m/s^2$

Free surface profile: $\begin{cases} h = h_{in}\ (1 + \frac{z}{A})^{an} & \text{for } z < z_1 \\ h = \delta, & \text{for } z > z_1 \end{cases}$

Case P1C: $h_{in} = 0.000476\ m\ (0.8\delta)$

$W_{in} = 0.1952\ m/s, \quad g = 9.81\ m/s^2$

Free surface profile: $\begin{cases} h = h_{in}\ (1 + \frac{z}{A})^{an} & \text{for } z < z_1 \\ h = \delta, & \text{for } z > z_1 \end{cases}$

Case P2: $h_{in} = 0.0009674\ m, \quad Fr_{in} = 3.0$

$W_{in} = 0.2922\ m/s\ , \quad z_{out} = 0.1445\ m$

$Fr_{out} = 1.0, \quad h_{out} = 0.002012\ m, \quad g = 9.81\ m/s^2$

Free surface profile: $\begin{cases} h = h_{in}\ (1 + \frac{z}{A}), & \text{for } z < z_1 \\ h = Ch_{in}\ [2 - (1 + \frac{z}{B})^{bn}], & \text{for } z_1 \leq z \leq z_2 \\ h = (h)_{z = z_2} + \dfrac{(z - z_2)}{(z_{out} - z_2)} \times & \\ (h_{out} - h_{z = z_2}), & \text{for } z > z_2 \end{cases}$

Case P3: $h_{in} = 0.000595$ m

$V_{in} = 0.1561$ m/s, $g = 0.0$

Free surface profile: $h = h_{in} \left(1 + \frac{z}{A}\right)^{an}$

Table 3: Summary of Results: Plane Flow

Problem	Optimum Profile	RMS Error in Pressure (Pa)
Case P1A (Parabolic Inlet)	--	0.1818
Case P1A (Uniform Inlet)	--	1.2
Case P1B	A = 0.004 an = -0.199 z_1 = 0.006	0.3346
Case P1C	A = 0.00001 an = 0.0445 z_1 = 0.0015	0.5536
Case P2	A = 0.055 an = 6.0486 B = 0.05 bn = -0.6 C = 3.5924 z_1 = 0.01445 m z_2 = 0.14161 m	2.172
Case P3	A = 0.003 an = 0.93	0.6013

Table 4: Flow Conditions: Radial Flow

General data: $\rho = 913.026\ Kg/m^3$

$\nu = 7.432 \times 10^{-6}\ m^2/s$

$r_{in} = 0.0508\ m$

$r_{out} = 0.1953\ m$

Case R1A: $h_{in} = 0.02\ m$, $V_{in} = 0.14996\ m/s$

$Q = 9.573 \times 10^{-4}\ m^3/s$, $g = 0.0$

Free surface profile: $h = h_{in} \left(\frac{r - A}{r_{in} - A} \right)^{an}$

Case R1B $h_{in} = 0.000508\ m$, $V_{in} = 0.1248\ m/s$

$Q = 2.0236 \times 10^{-5}\ m^3/s$, $g = 0.0$

Free surface profile: $h = h_{in} \left(\frac{r - A}{r_{in} - A} \right)^{an}$, for $r < r_1$

$h = C\, h_{in} \left[2 - \left(\frac{r}{r_{in}} \right)^{bn} \right]$, for $r \geq r_1$

Case R2A: $h_{in} = 0.02\ m$, $V_{in} = 0.14996\ m/s$

$Q = 9.573 \times 10^{-4}\ m^3/s$, $g = 9.81\ m/s^2$

Free surface profile: $h = h_{in} \left(\frac{r - A}{r_{in} - A} \right)^{an}$

Case R2B: $h_{in} = 0.000508\ m$, $V_{in} = 0.1248\ m/s$

$Q = 2.0236 \times 10^{-5}\ m^3/s$, $g = 9.81\ m/s^2$

Free surface profile: $h = h_{in} \left(\frac{r - A}{r_{in} - A} \right)^{an}$, for $r < r_1$

$h = C\, h_{in} \left[2 - \left(\frac{r}{r_{in}} \right)^{bn} \right]$, for $r \geq r_1$

Case R2C: $h_{in} = 0.000508$ m, $V_{in} = 0.1248$ m/s

$Q = 2.0236 \times 10^{-5}$ m^3/s, $g = 9.81$ m/s^2

$h_{out} = 0.00030265$ m (Fr = 1.0)

Free surface profile: $h = h_{in} \left(\frac{r - A}{r_{in} - A} \right)^{an}$ for $r < r_1$

$h = C\, h_{in} \left[2 - \left(\frac{r}{r_{in}}\right)^{b} \right]$, for $r \geq r_1$

$h = h_{out}$, at $r = r_{out}$

Table 5: Summary of Results: Radial Flow

Problem	Optimum Profile	RMS Error in Pressure (Pa)
Case R1A	A = -0.05 an = -1.0	1.238
Case R1B	A = 0.044 an = 2.2876 r_1 = 0.06236 C = 9.74 bn = 0.02	0.2961
Case R2A	A = 0.01 an = 0.04	1.06
Case R2B	A = 0.04 an = 8.8337 r_1 = 0.05369 C = 8.1225 bn = 0.05	0.5478
Case R2C	A = 0.04 an = 8.822 r_1 = 0.05369 C = 8.1 bn = 0.0	0.7552

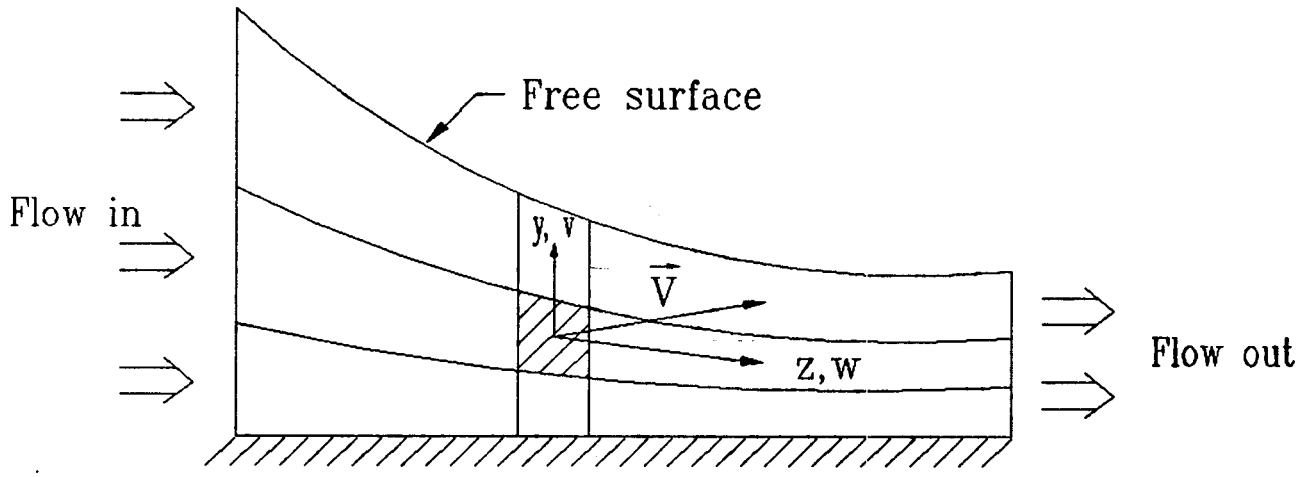

Fig. 1.1 The coordinate system on a grid cell

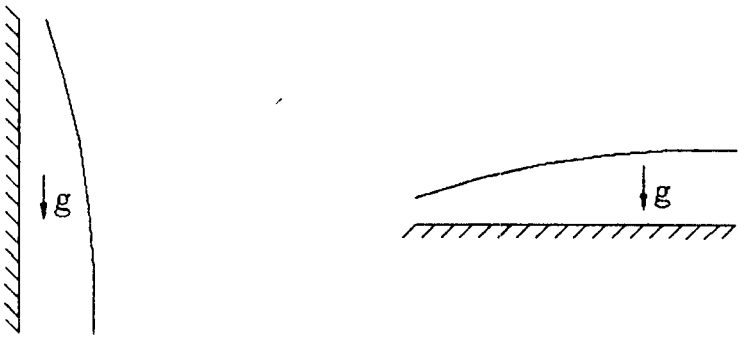

P1. Plane falling film P2. Plane film flow on horizontal plate

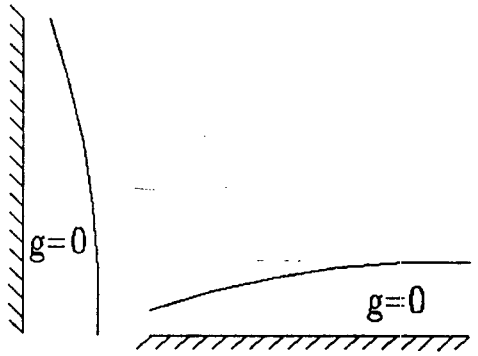

P3. Plane film flow under zero gravity

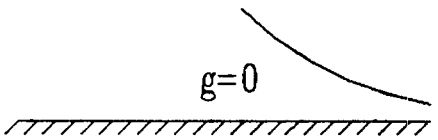

R1. Radial film flow under zero gravity

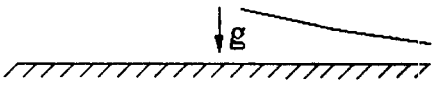

R2. Radial film flow on horizontal plate

Fig.1.2 Flow systems in present investigation

Fig.3 Analytical solution for plane flow over a plate in the presence of gravity

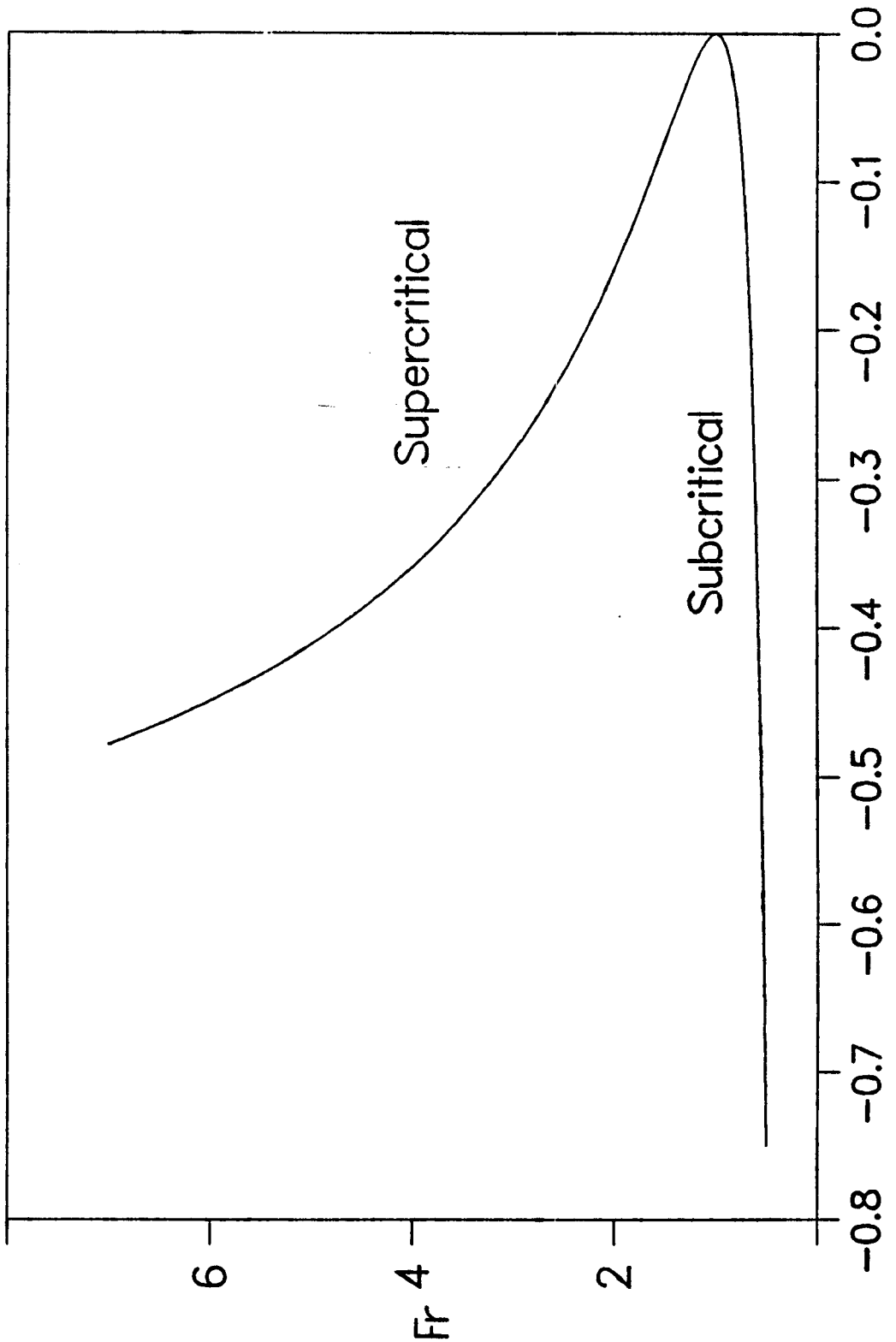

Fig.4 Analytical solution for radial flow over a plate in the presence of gravity

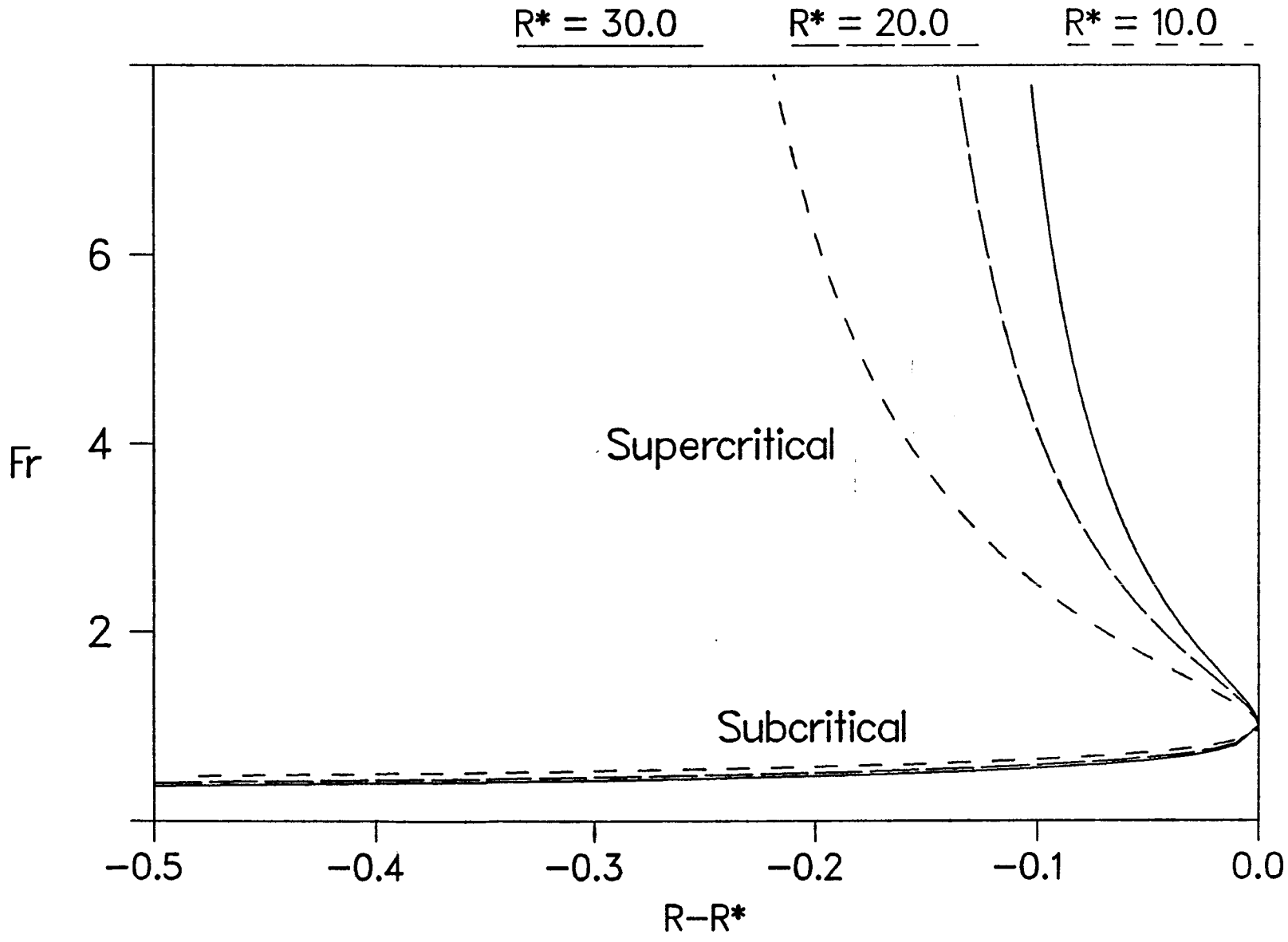

Fig.1.5 Comparison of the solution for different grid sizes

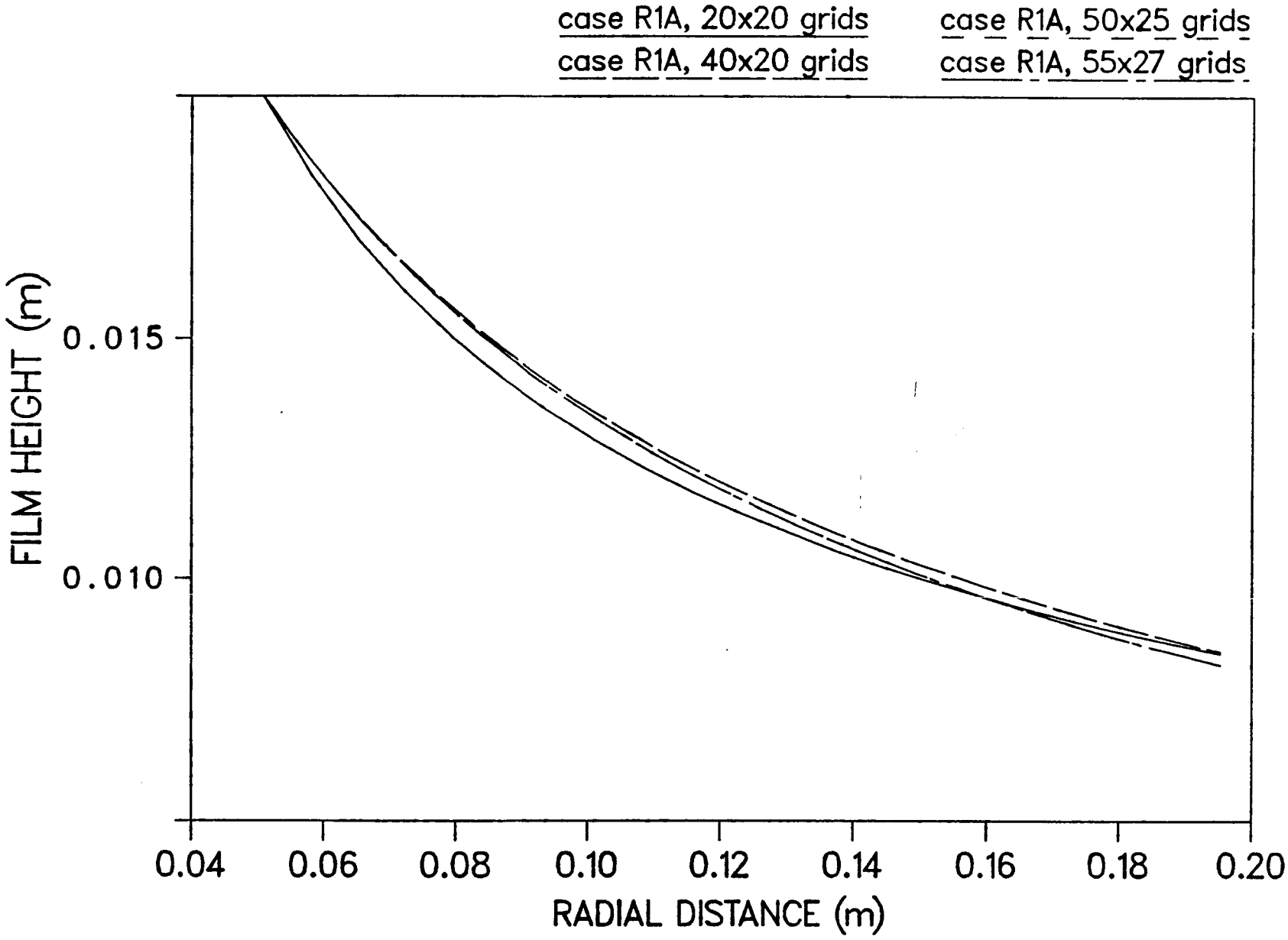

Fig.1.6 Film height in a developing falling film flow

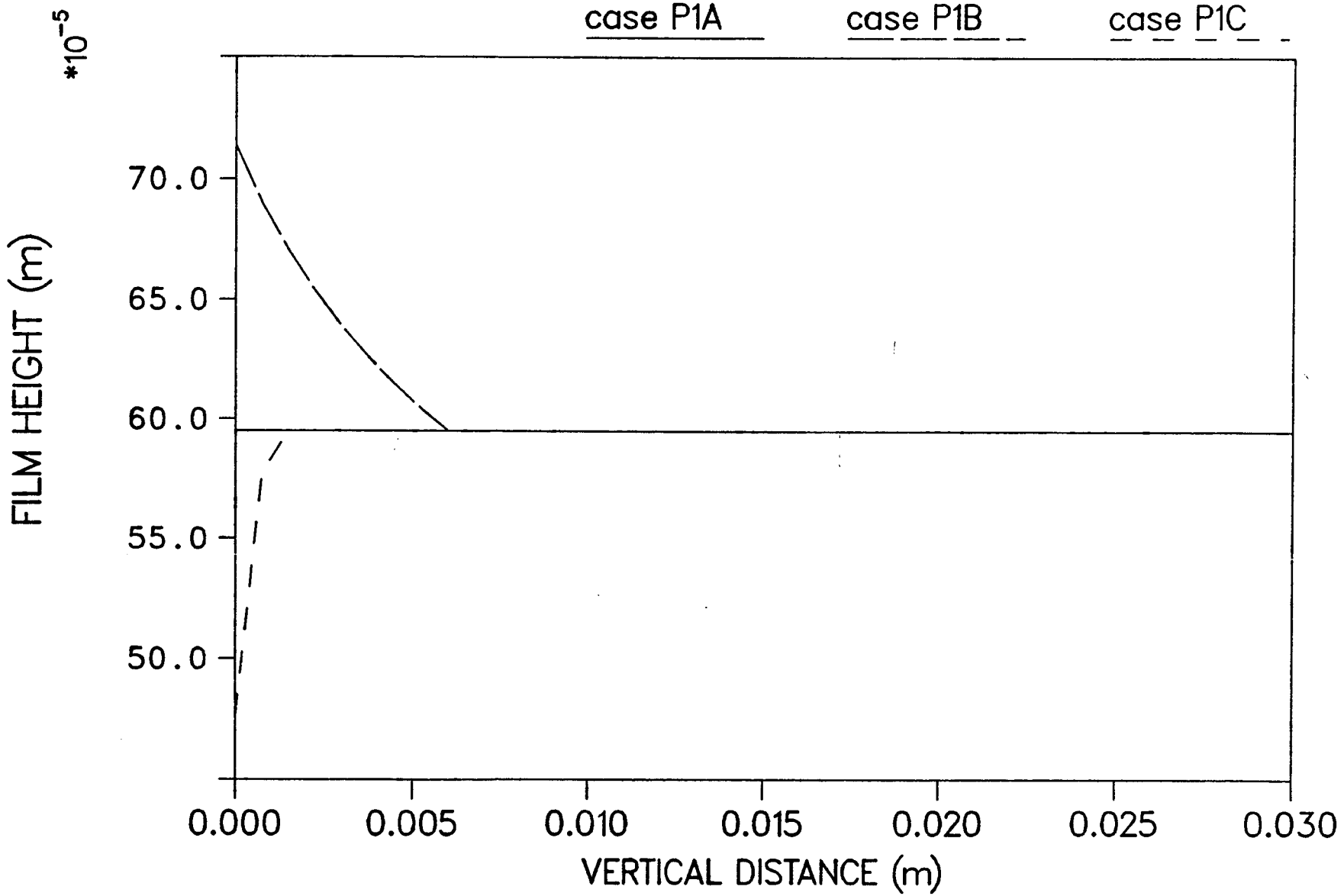

Fig.1.7 Free surface pressure in falling film flow

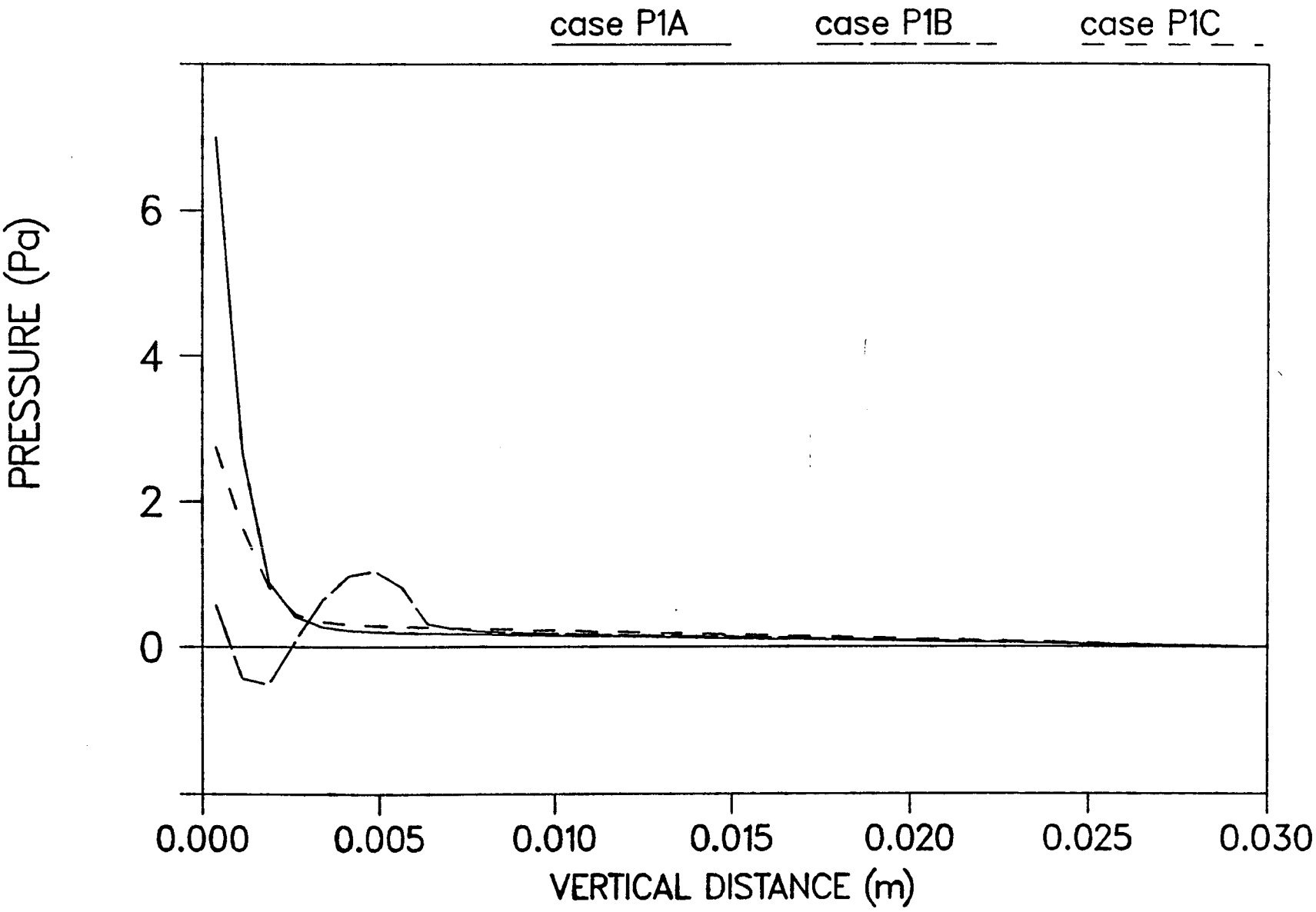

Fig.1.8 Friction coefficient in falling film flow

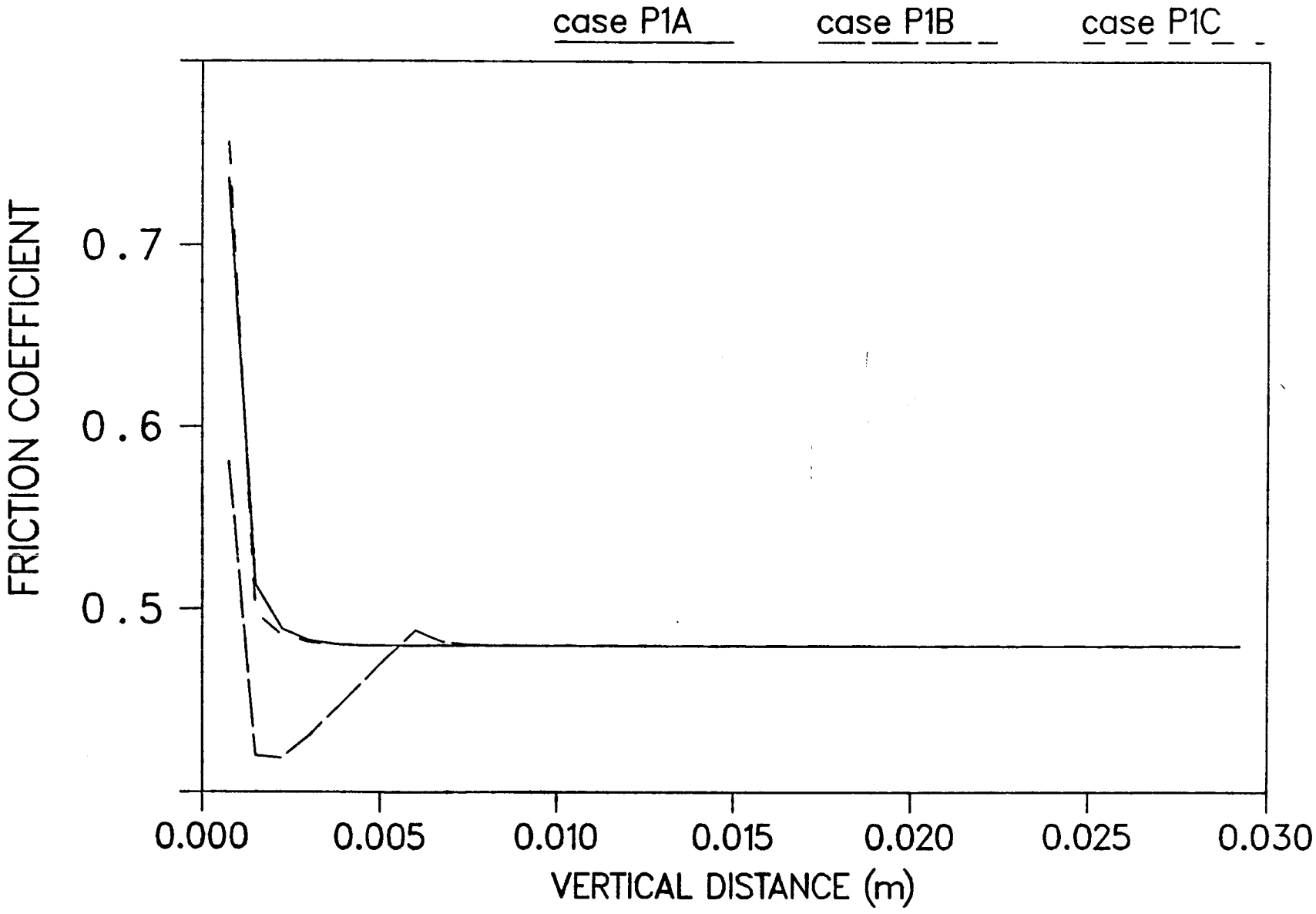

Fig.1.9 Comparison of the velocity profile at the exit for different inlet conditions in a falling film flow

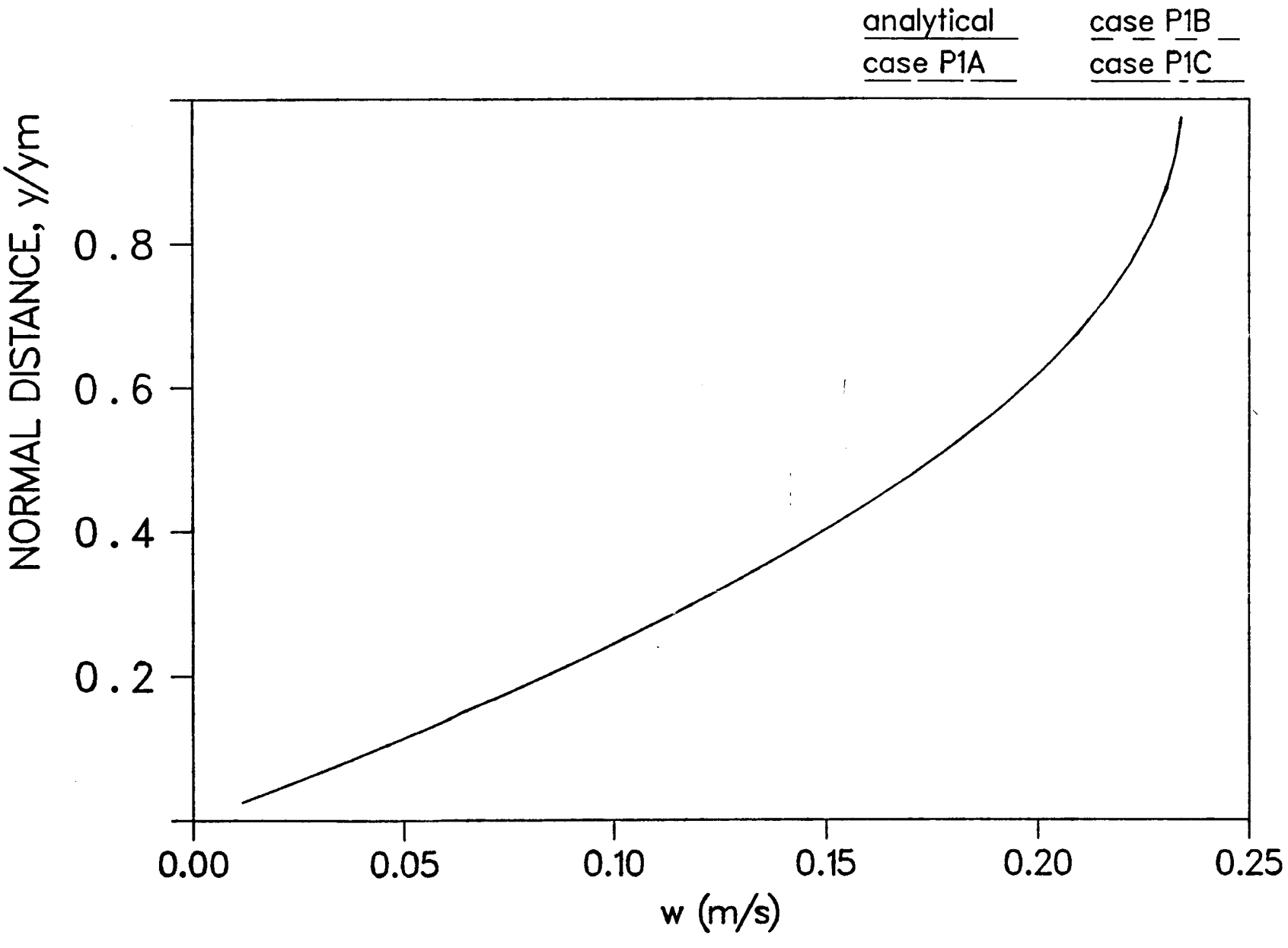

Fig.1.10 Film height for plane horizontal flow

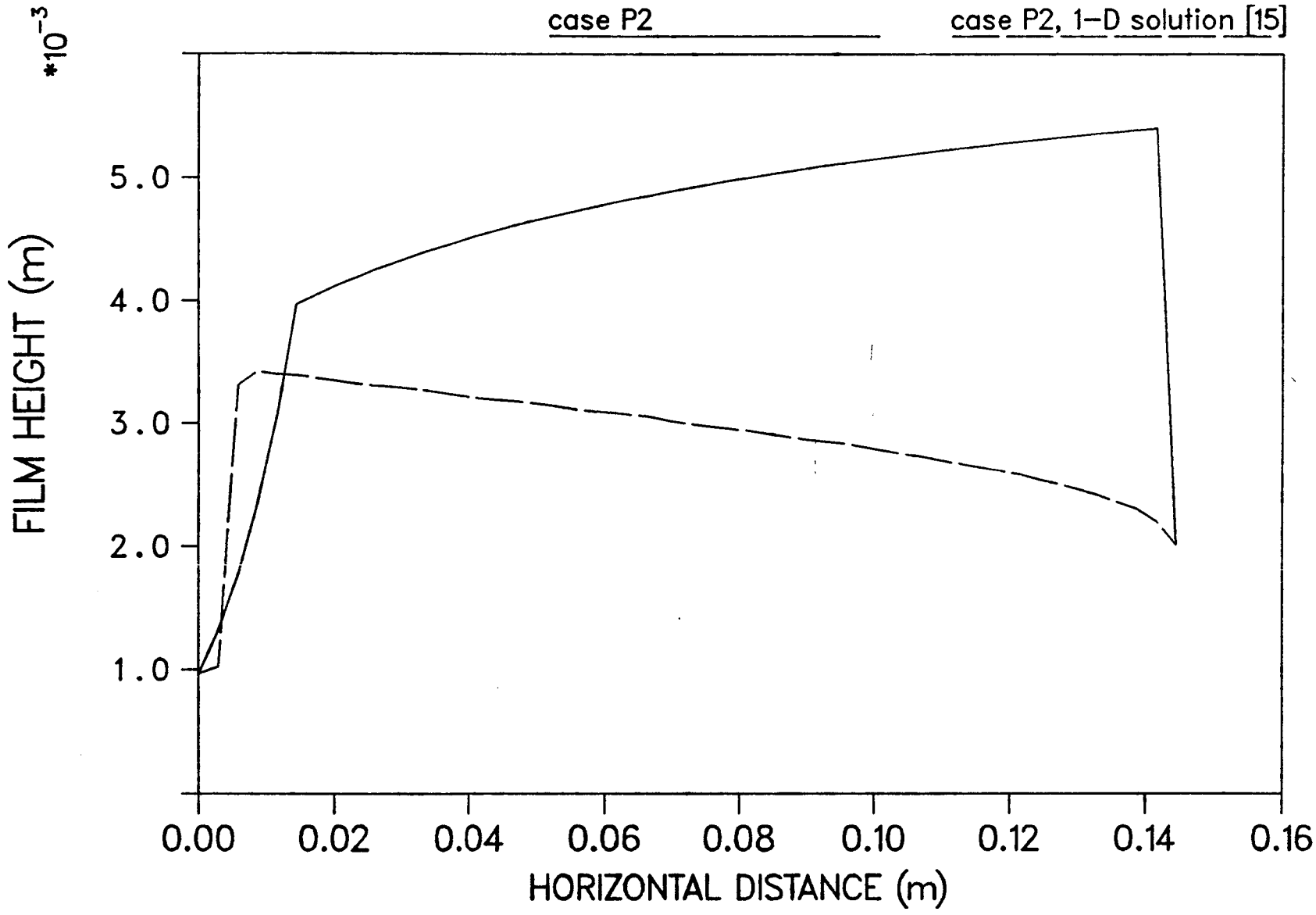

Fig.1.11 Velocity profile for plane horizontal flow

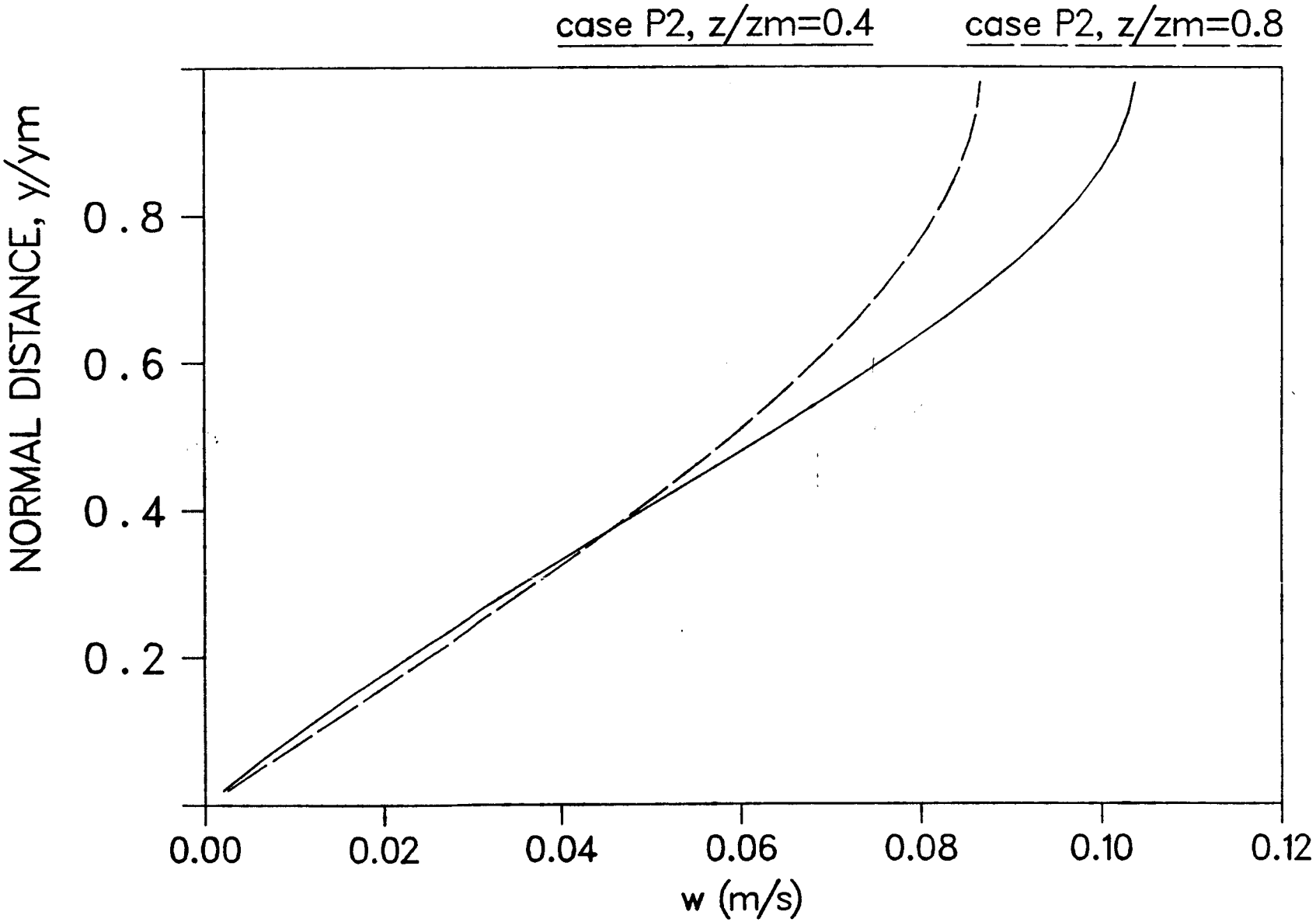

Fig.1.12 Wall shear stress for plane horizontal flow

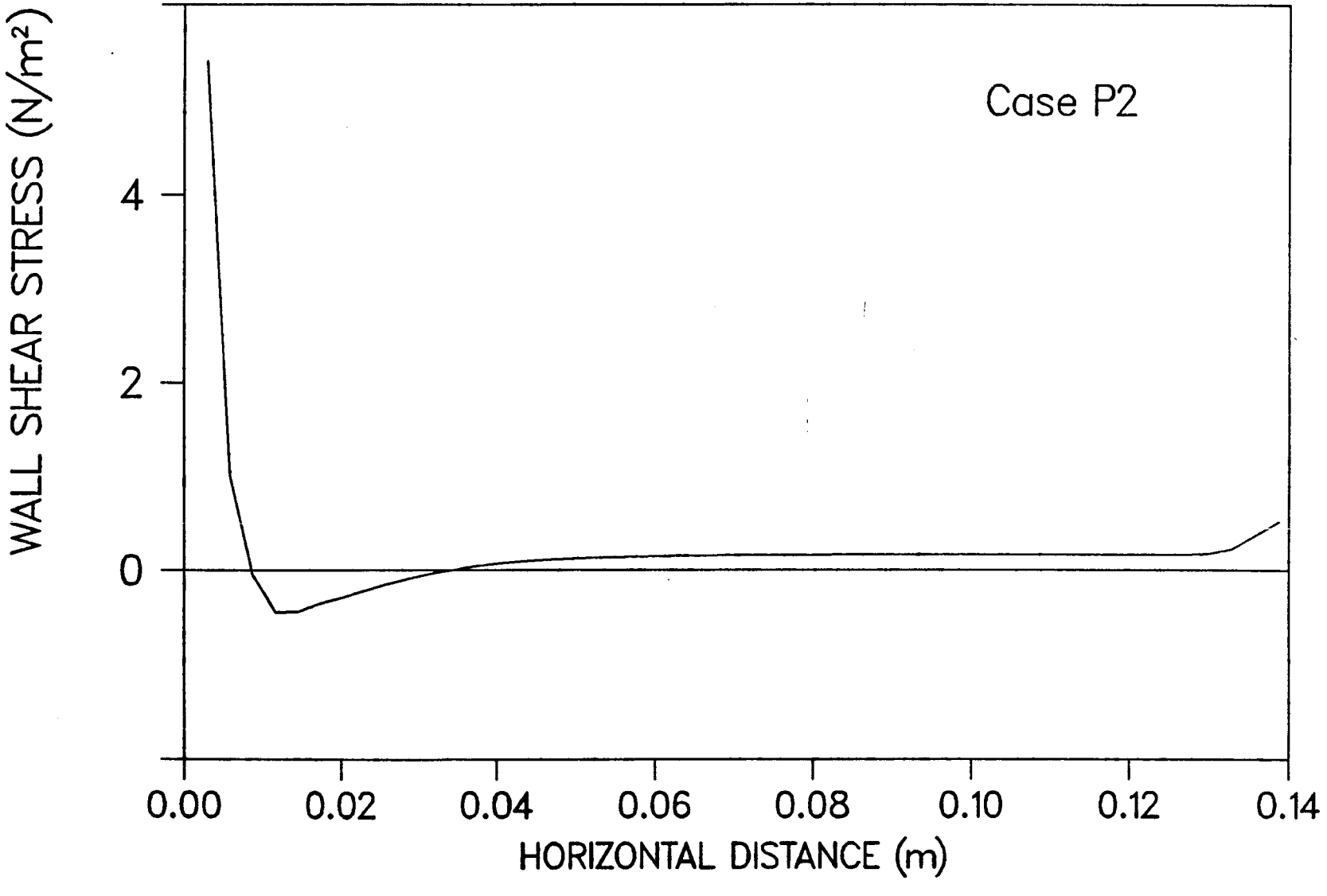

Fig.1.13 Friction coefficient for plane horizontal flow

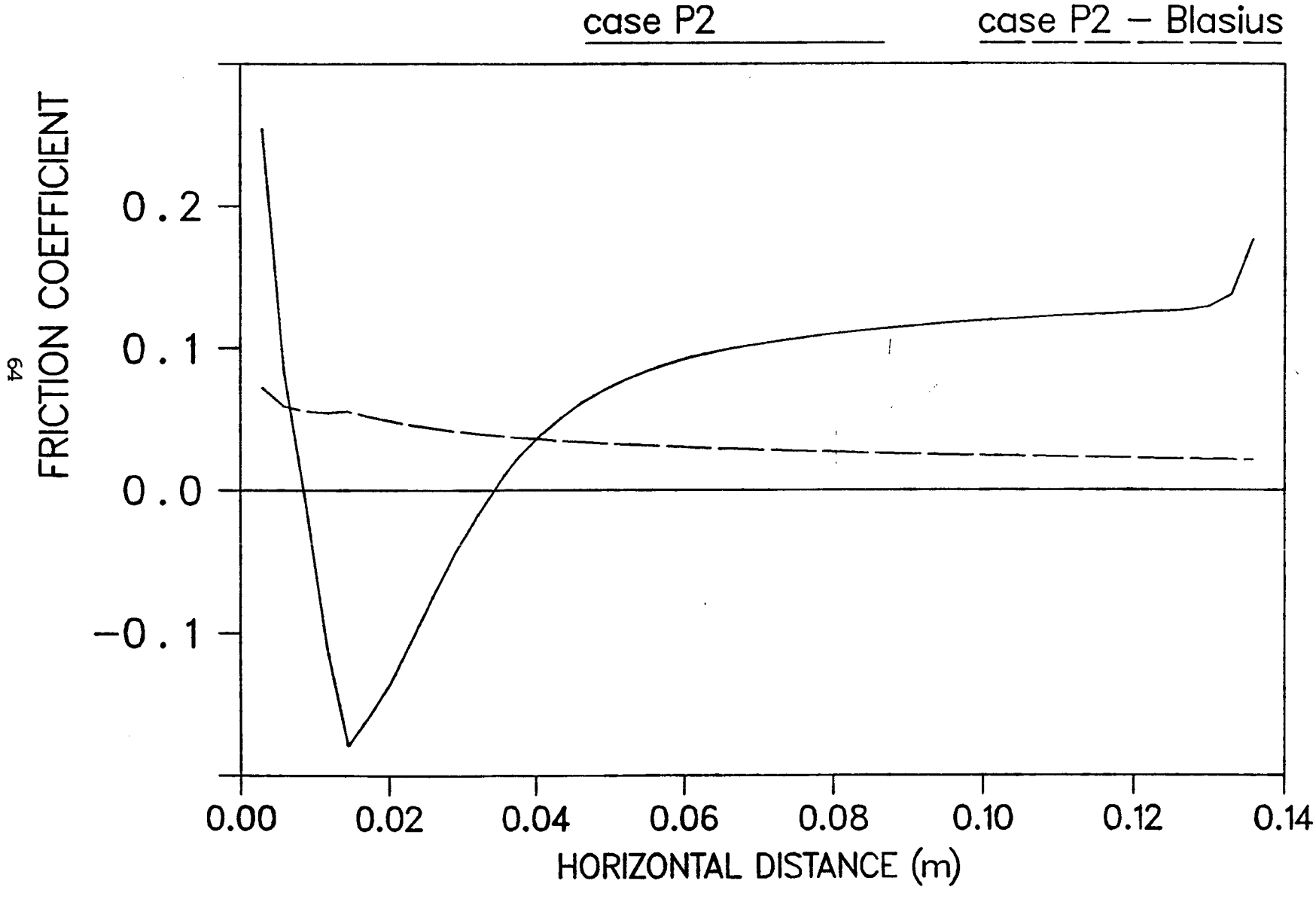

Fig.1.14 Film height for plane flow under zero gravit\

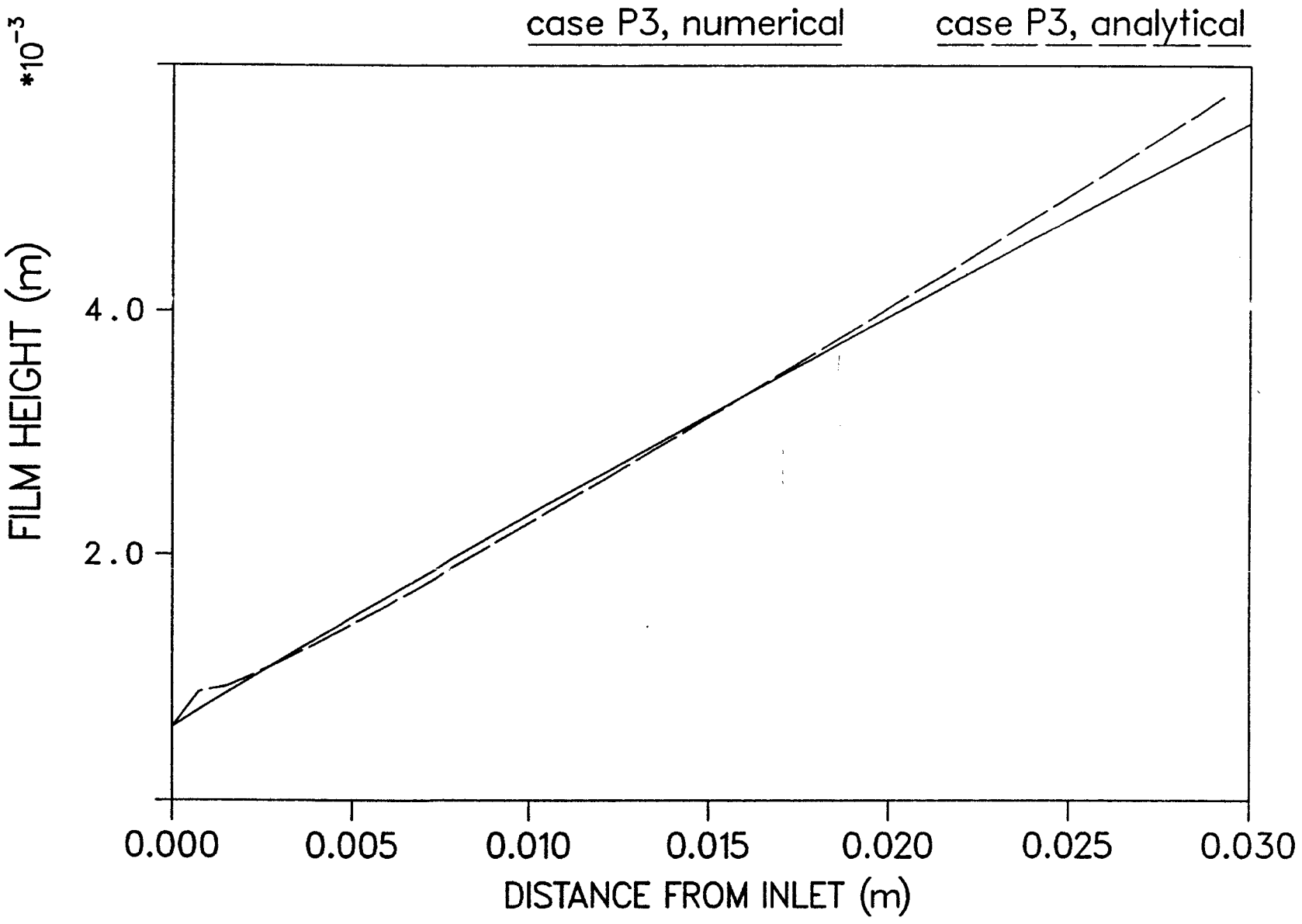

Fig.1.15 Free surface pressure for plane flow under zero gravity

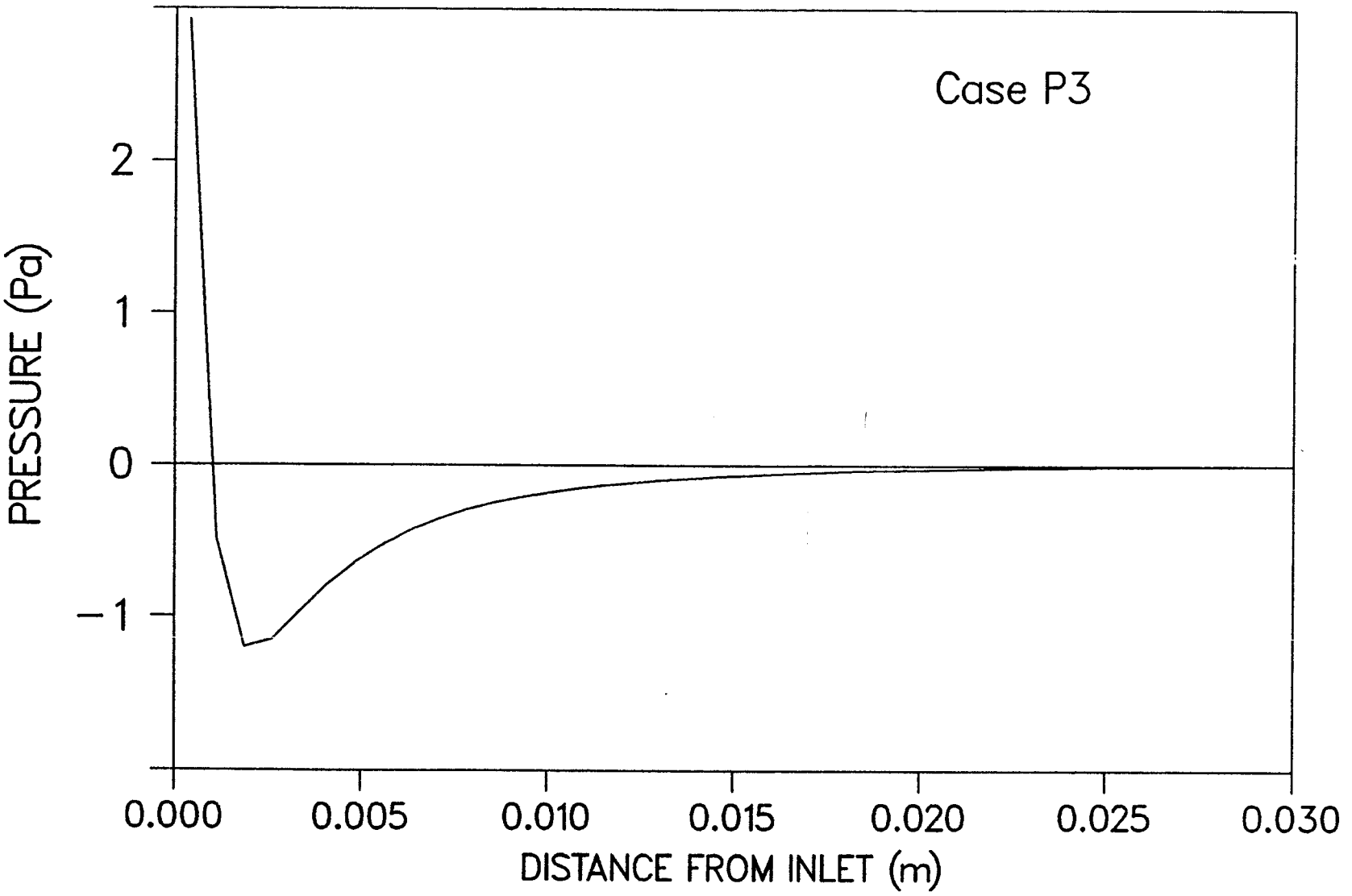

Fig.1.16 Velocity profile for plane flow under zero gravity

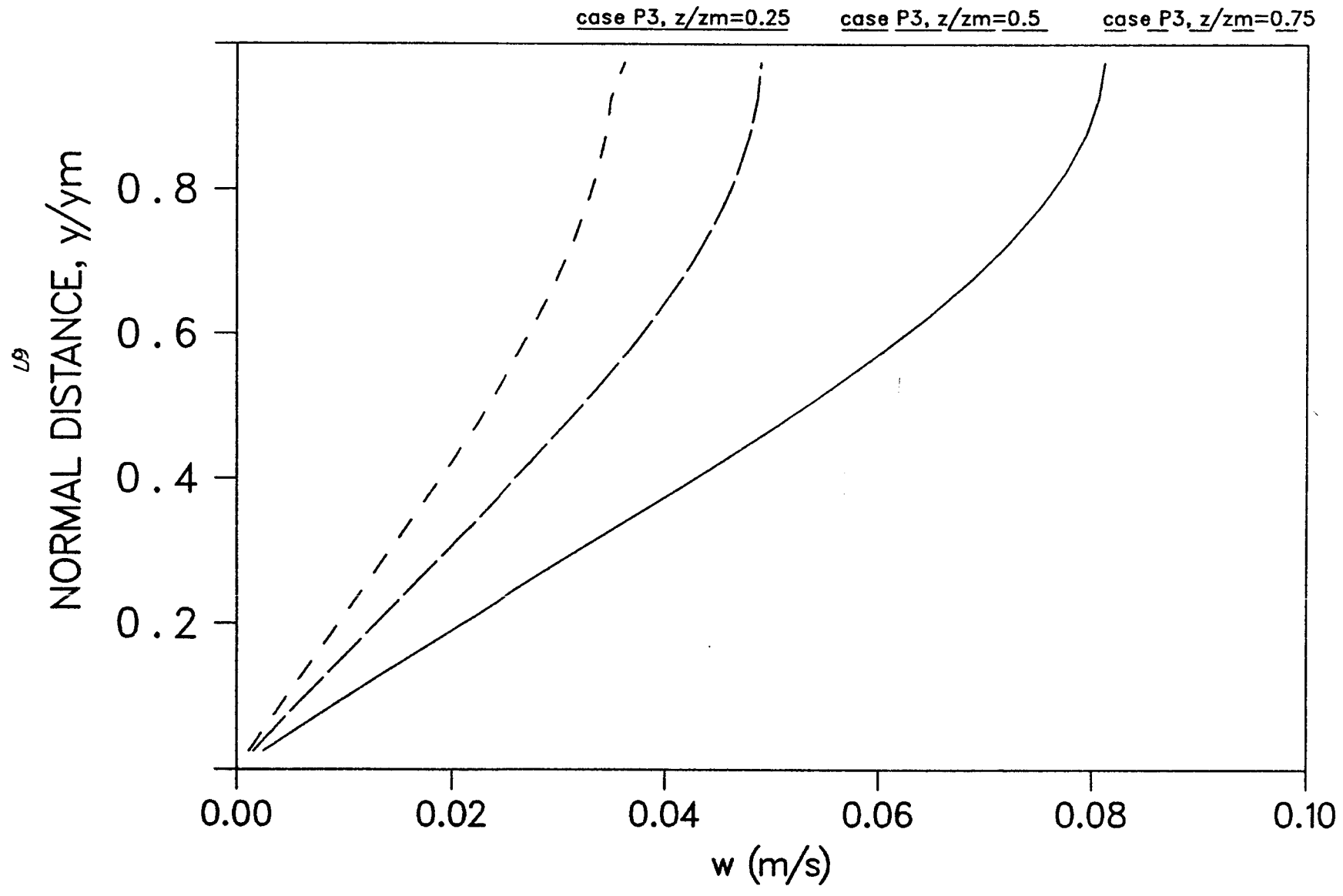

Fig.1.17 Wall shear stress for plane flow under zero gravity

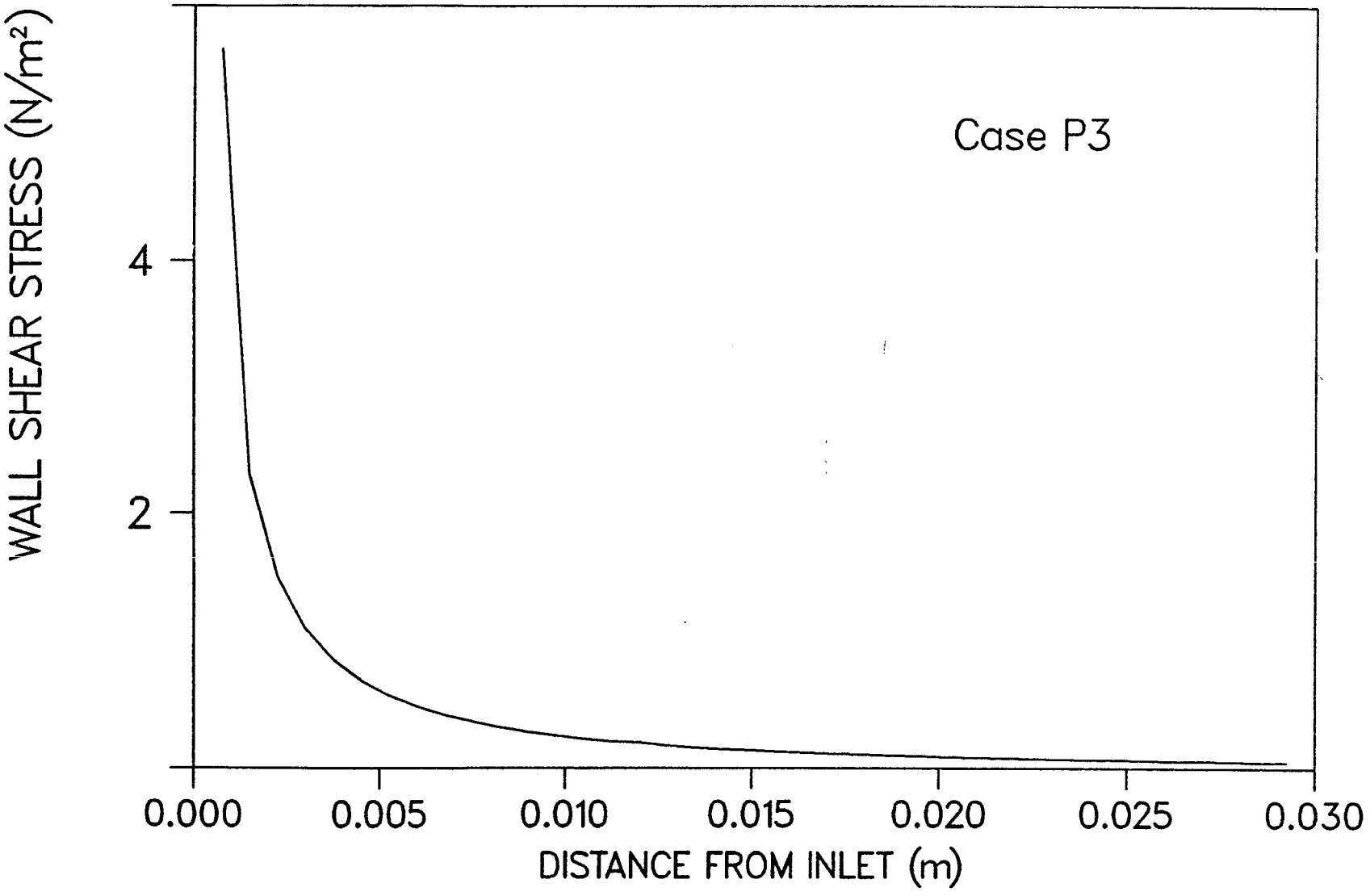

Fig.1.18 Friction coefficient for plane flow under zero gravity

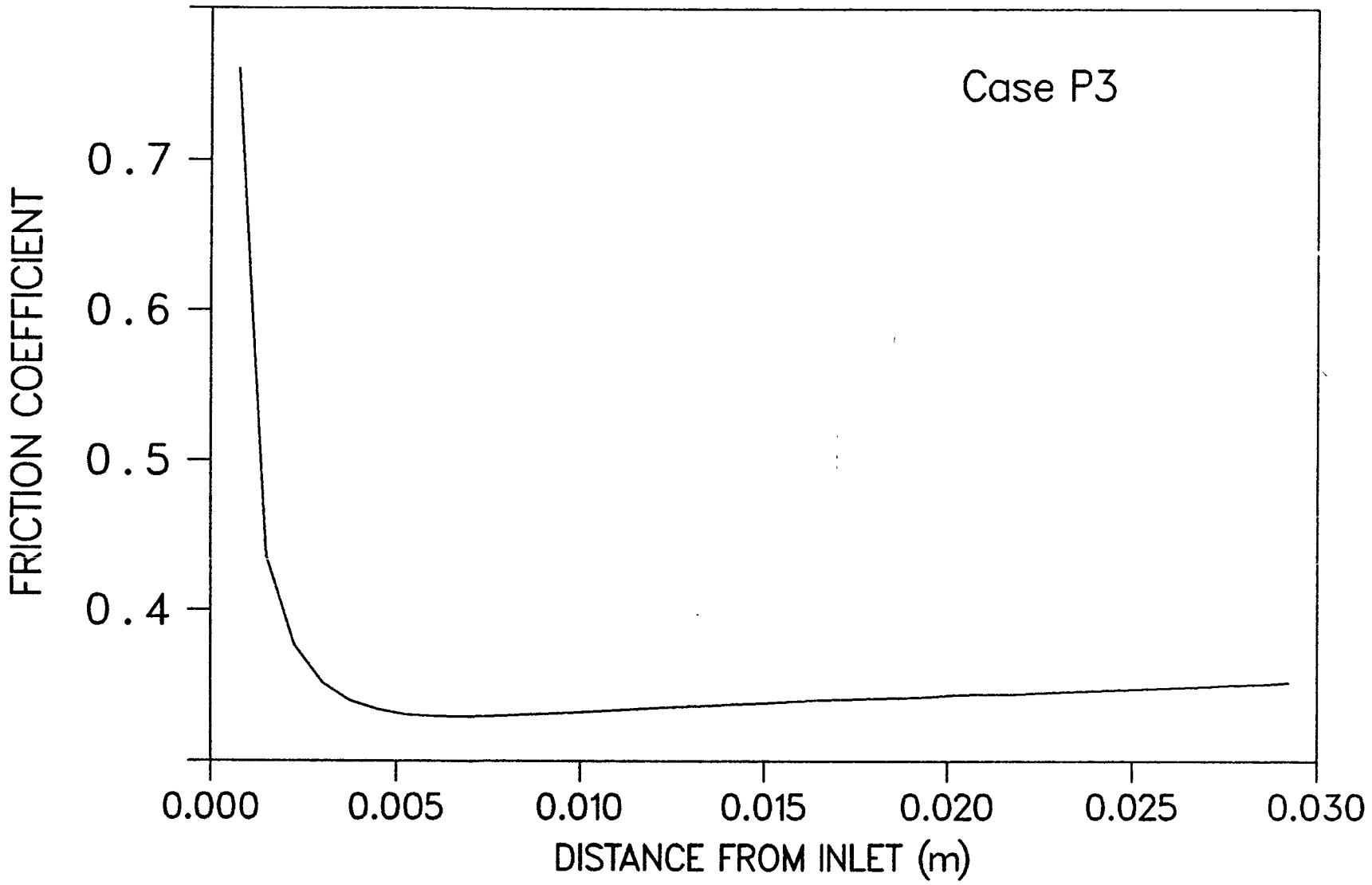

Fig.1.19 Film height for radial flow (Cases R1A and R2A)

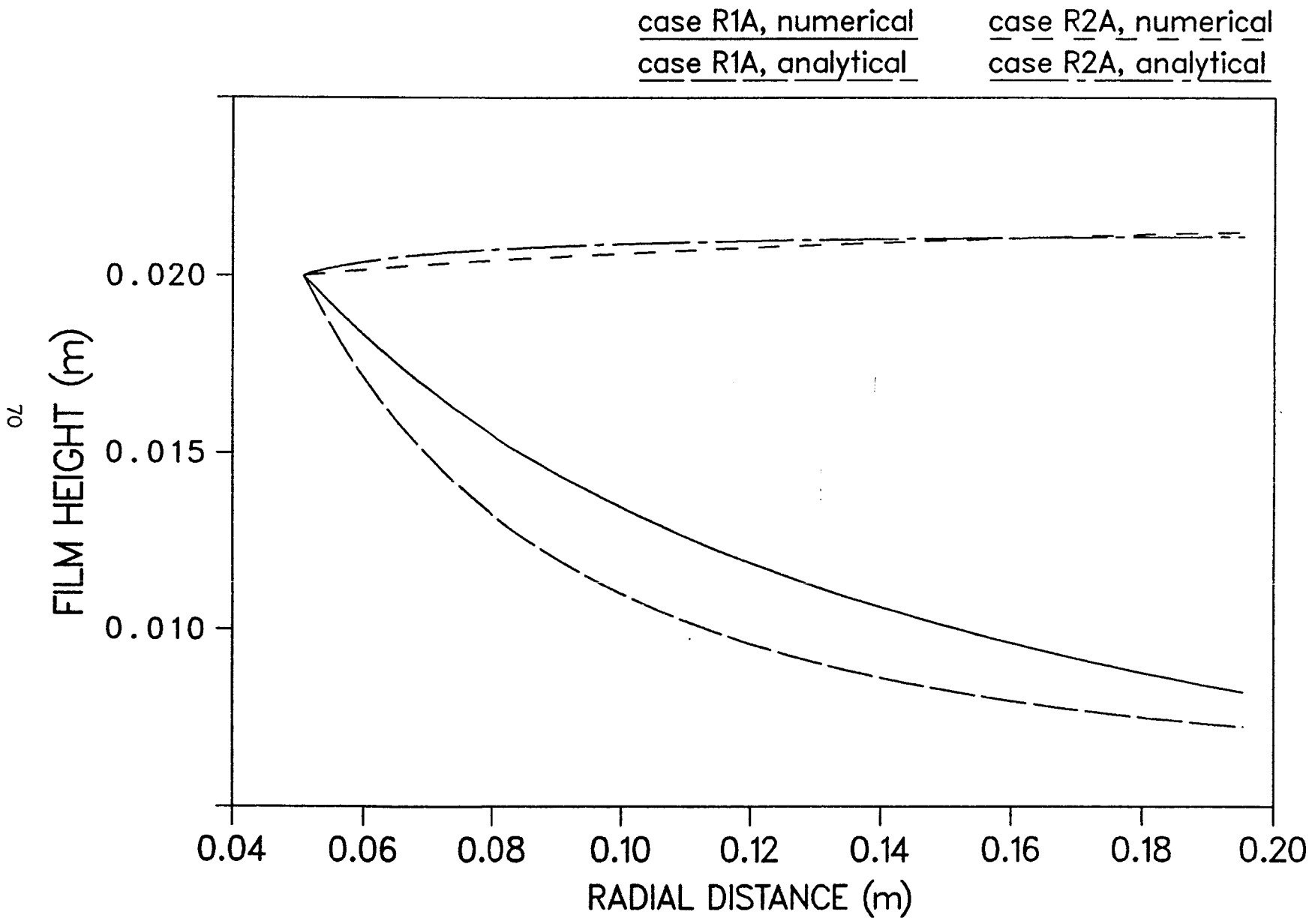

Fig.I.20 Velocity profile for radial flow (Cases R1A and R2A

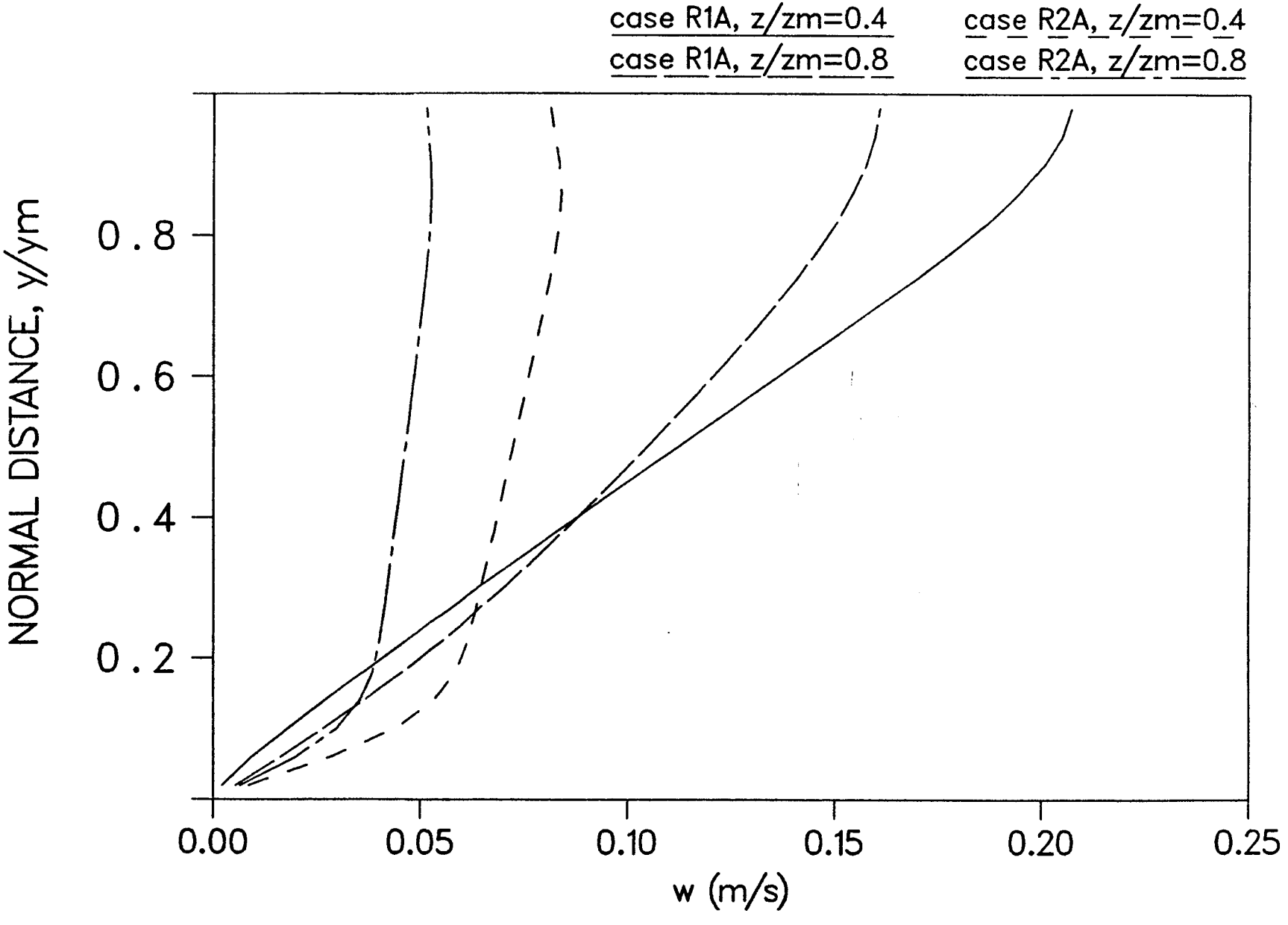

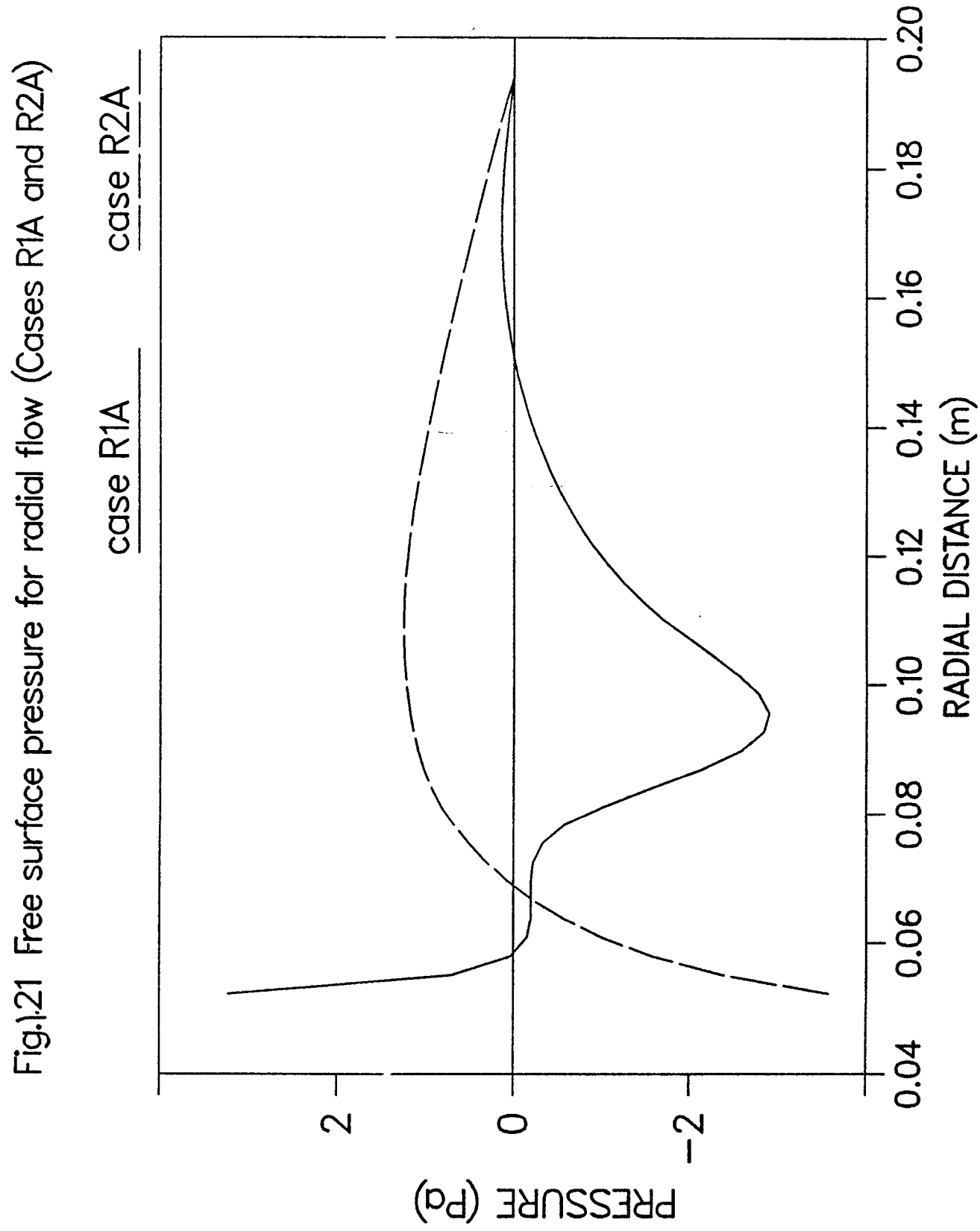

Fig.1.21 Free surface pressure for radial flow (Cases R1A and R2A)

Fig.1.22 Wall shear stress for radial flow (Cases R1A and R2A)

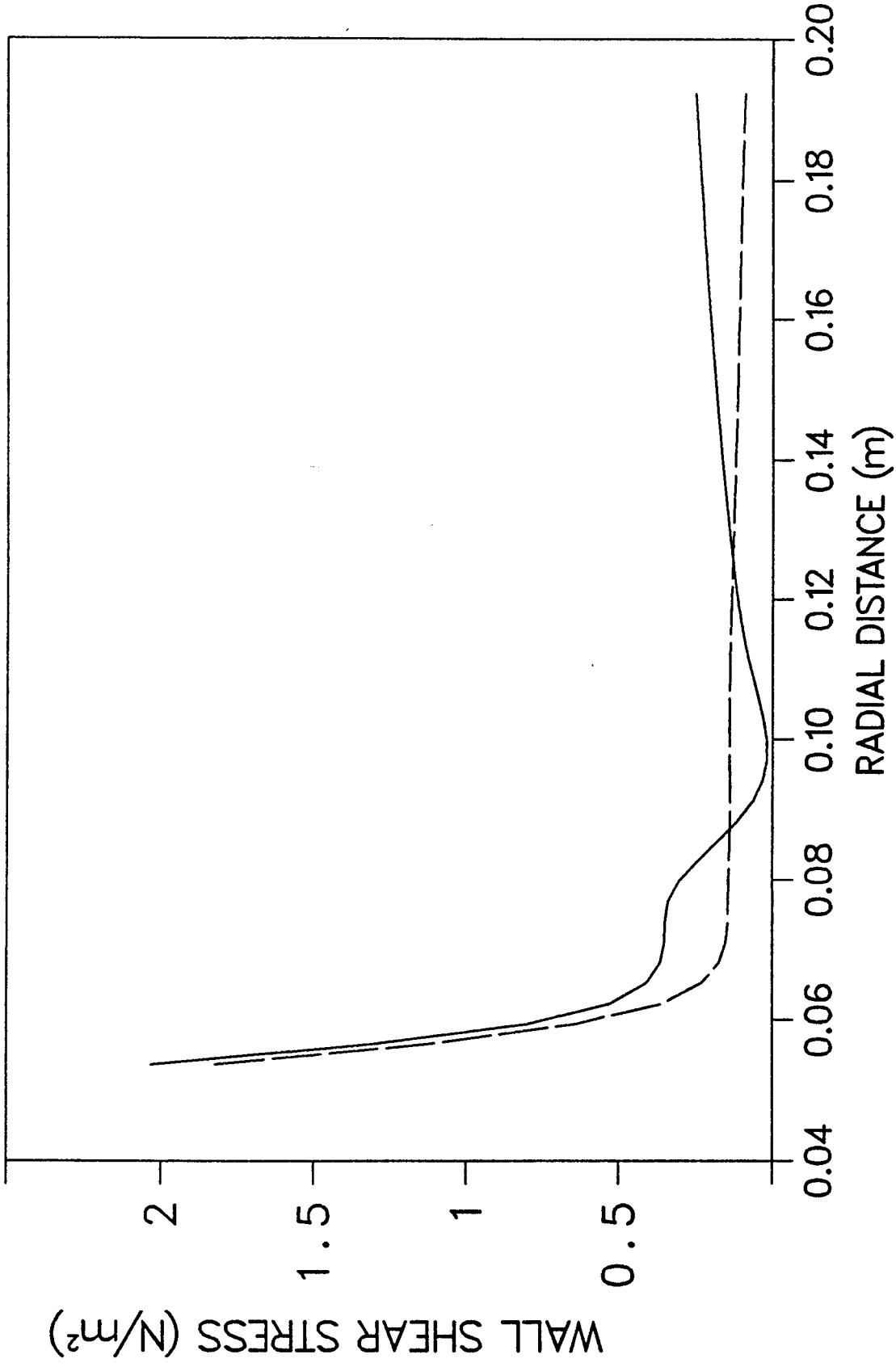

Fig.I.23 Friction coefficient for radial flow (Cases R1A and R2A)

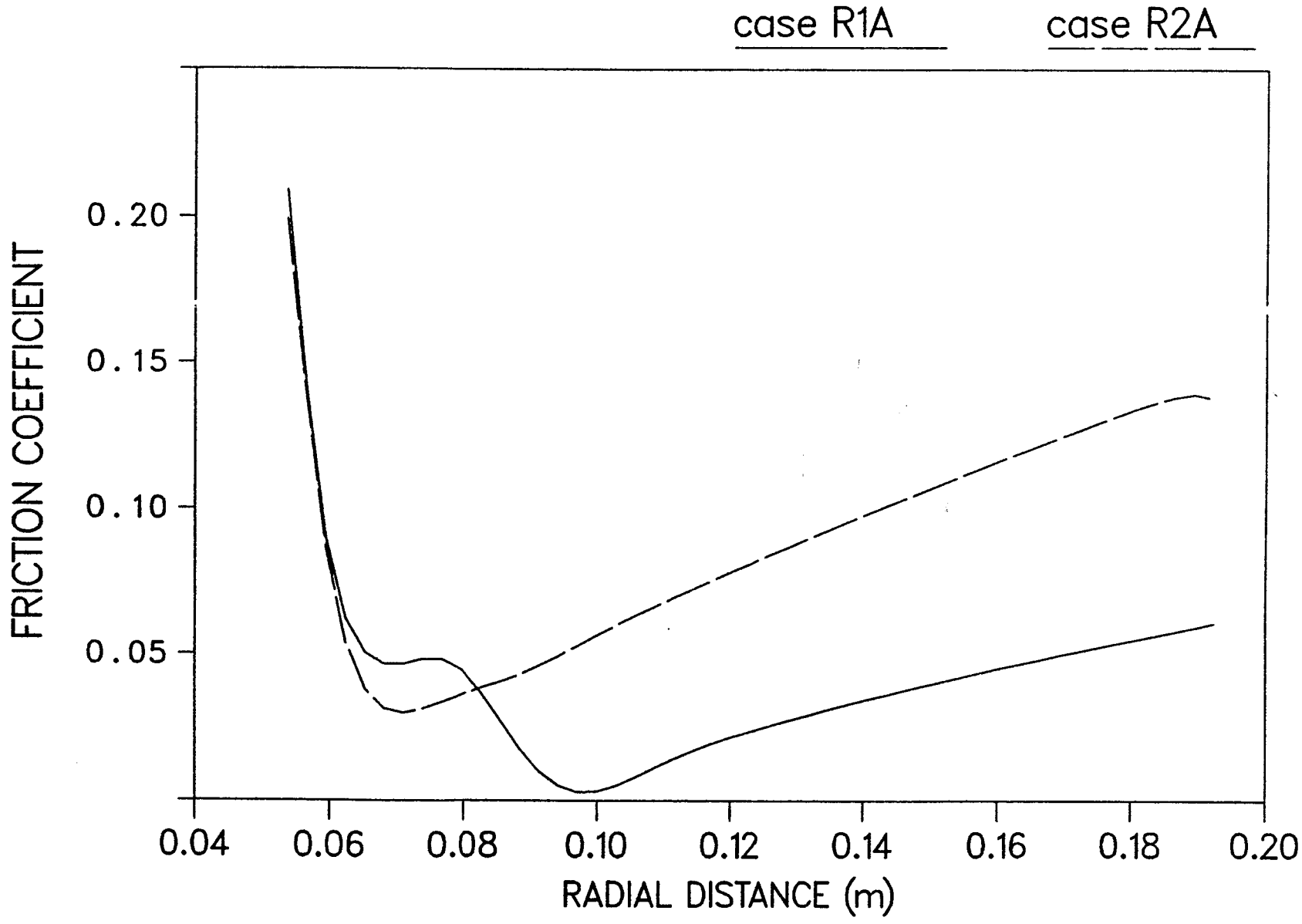

Fig.1.24 Film height for radial flow (Cases R1B, R2B and R2C)

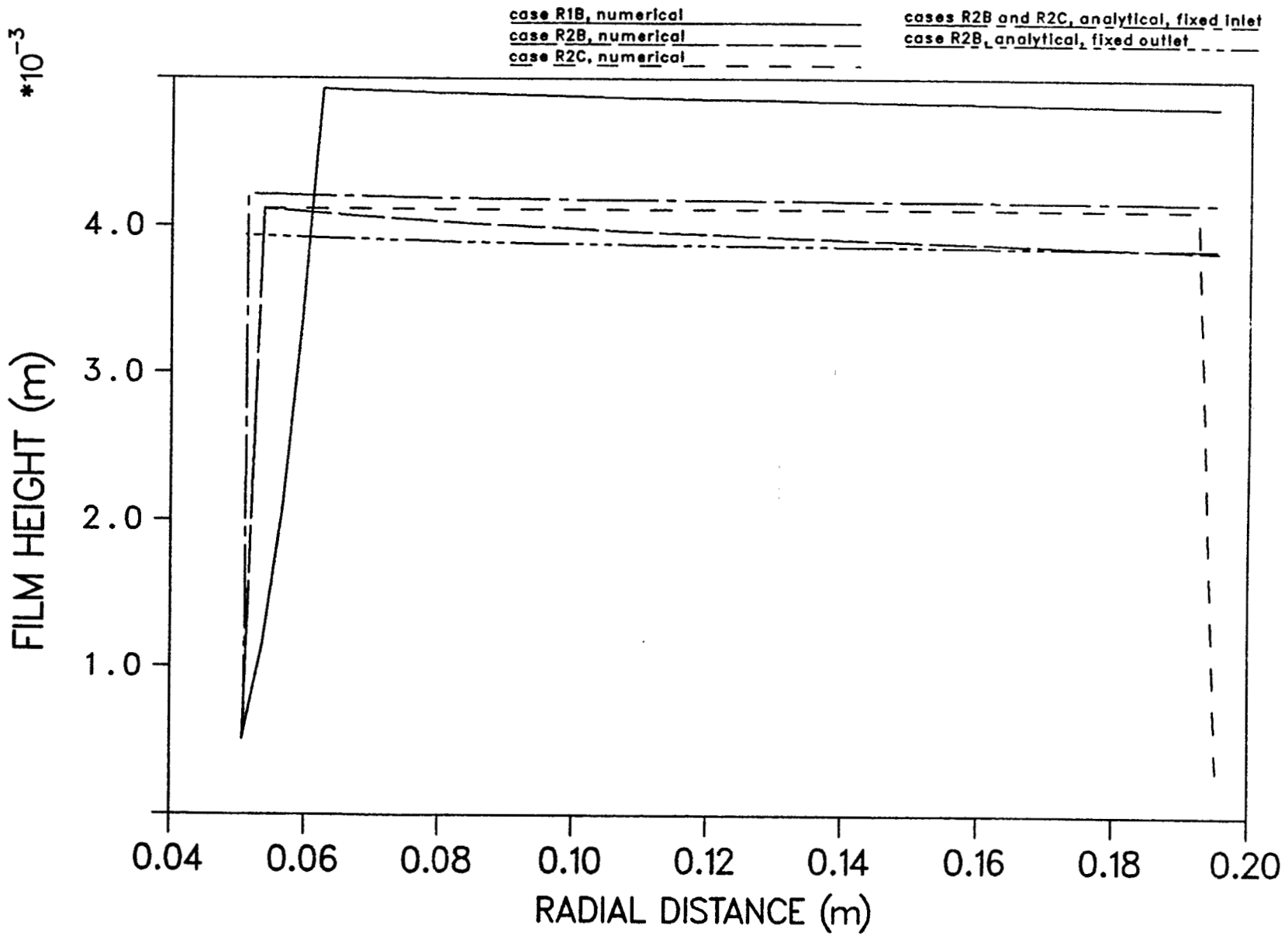

Fig.I.25 Velocity profile for radial flow (Cases R1B and R2B)

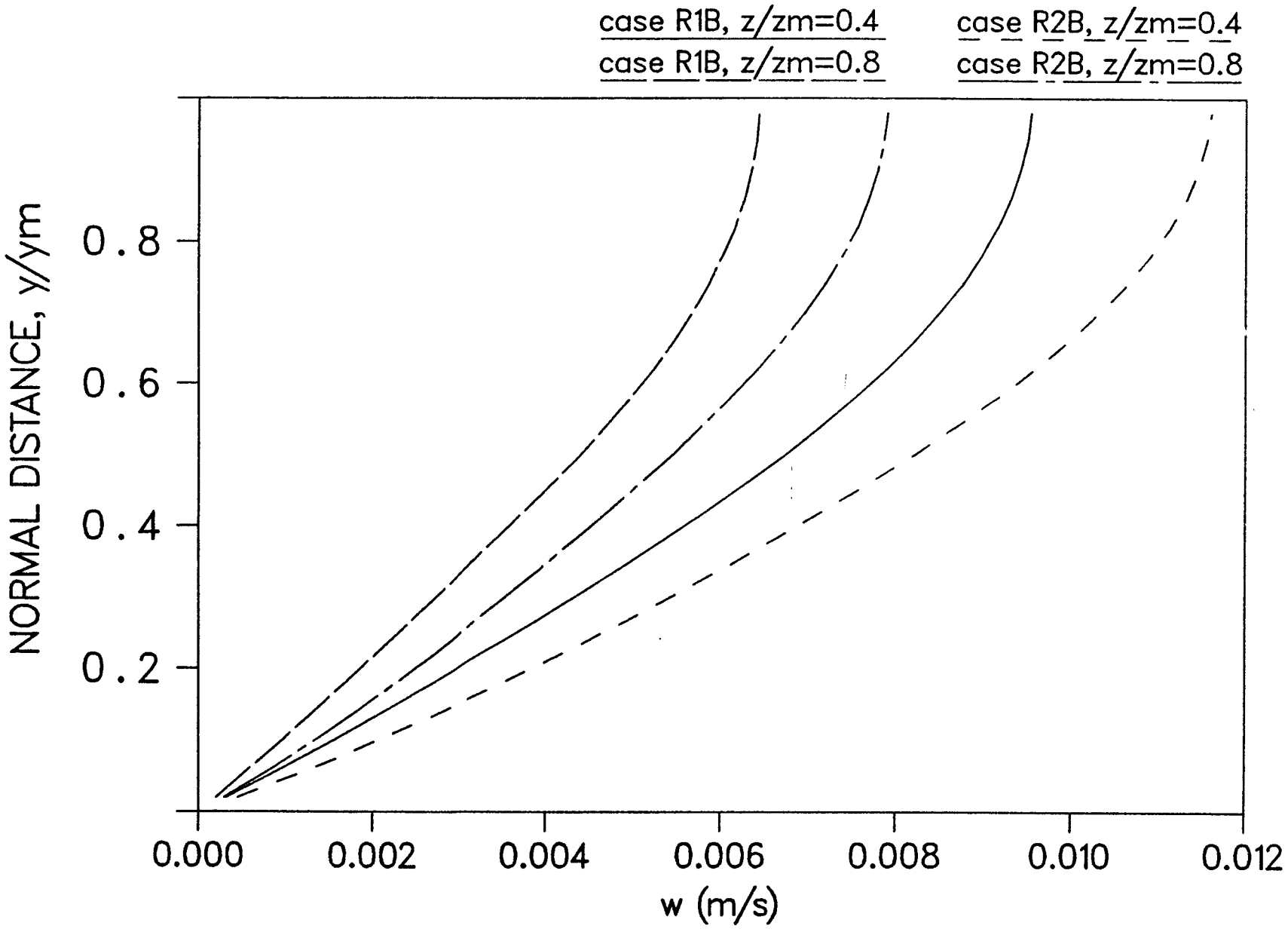

Fig.1.26 Free surface pressure for radial flow (Cases R1B, R2B and R2C)

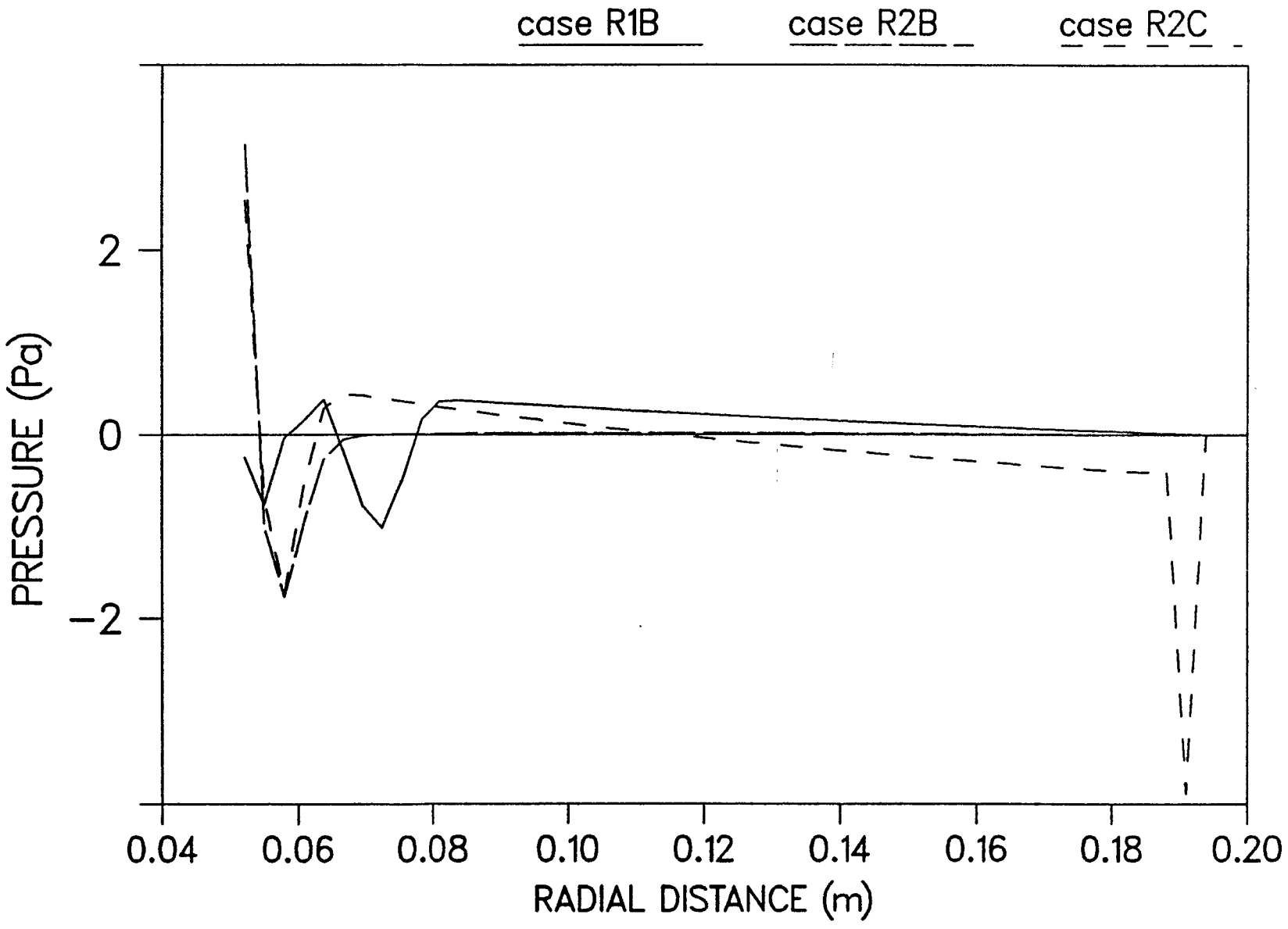

Fig.I.27 Wall shear stress for radial flow (Cases R1B, R2B and R2C)

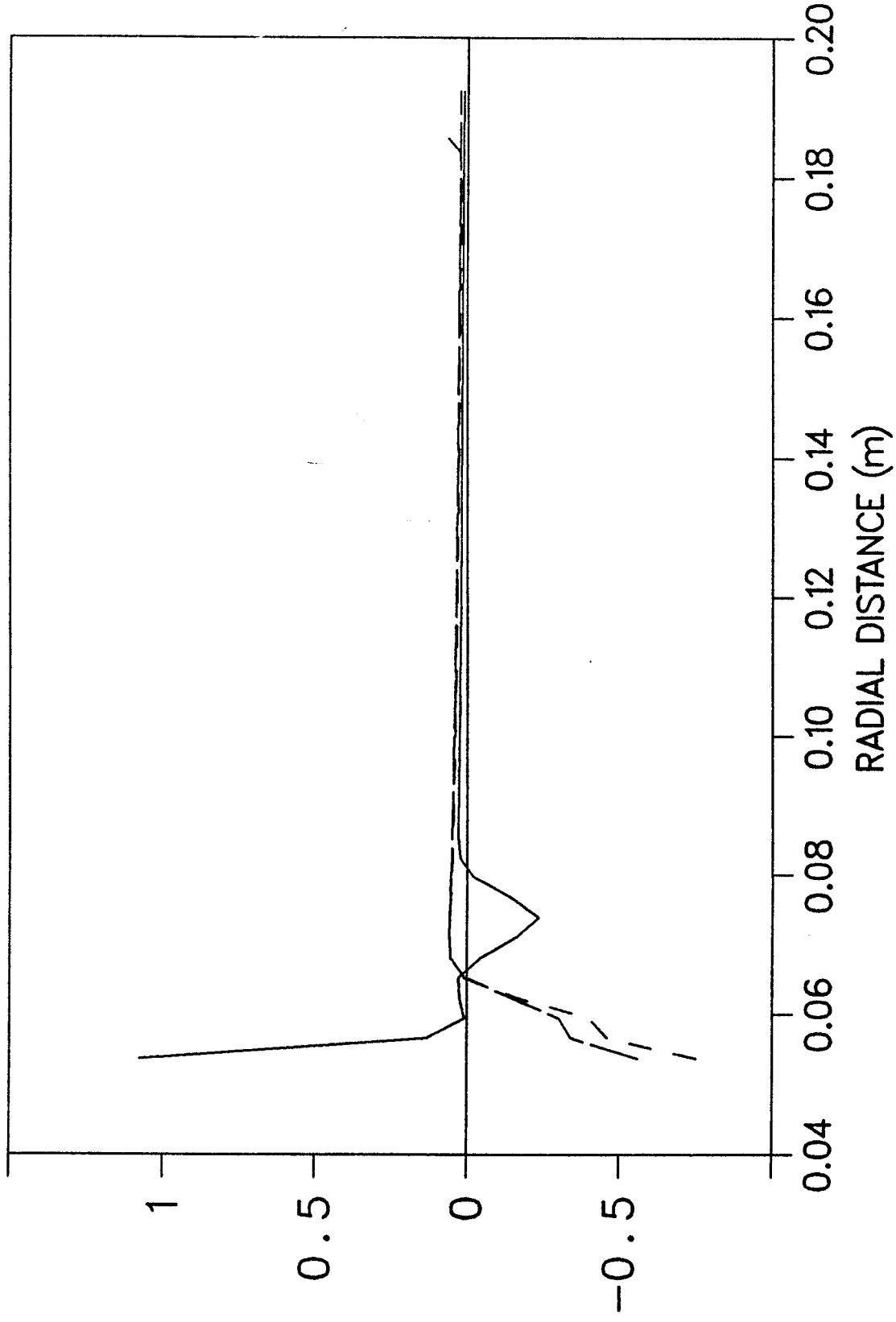

Fig.1.28 Friction coefficient for radial flow (Cases R1B, R2B and R2C)

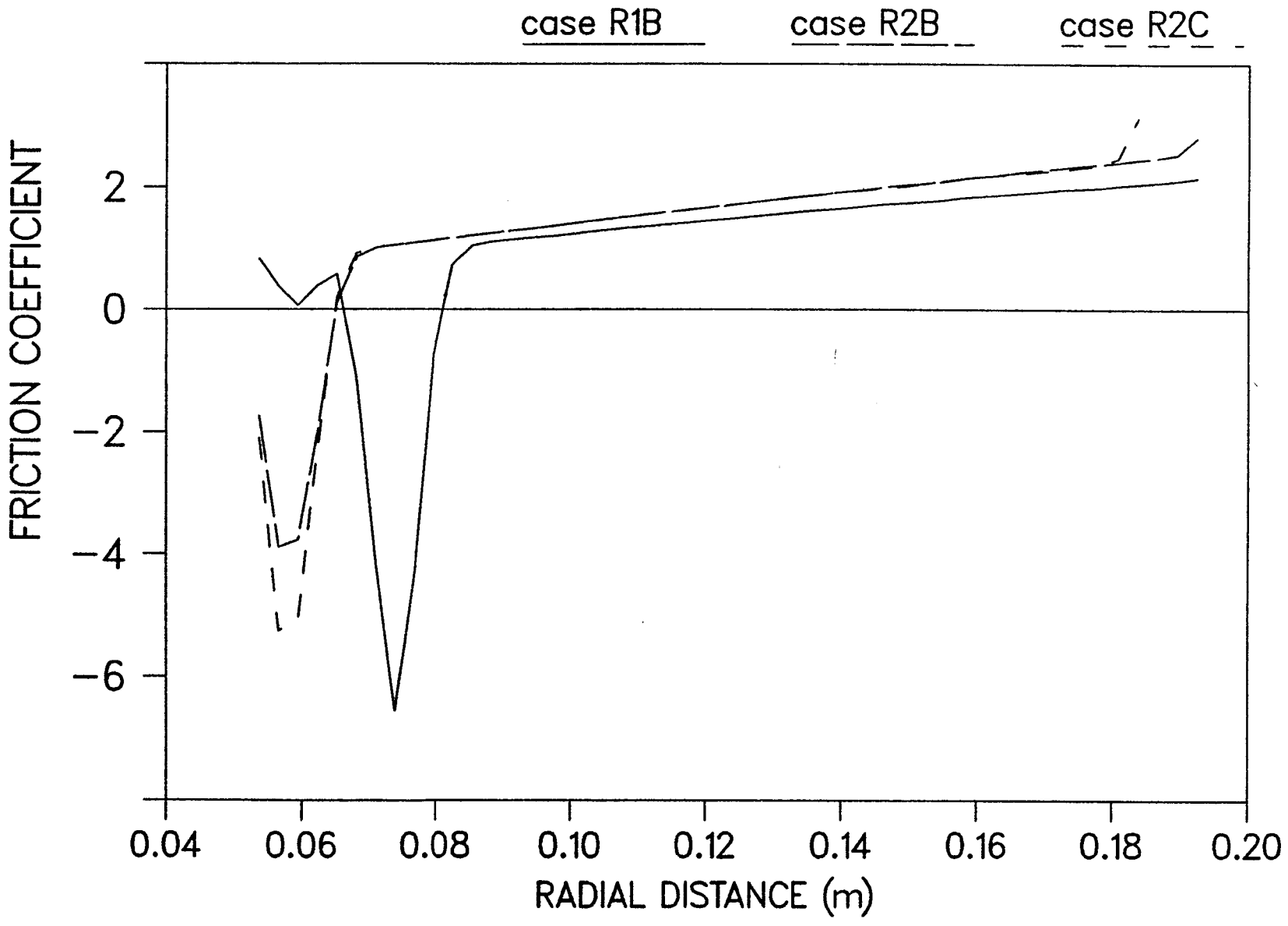

One-dimensional plane flow analysis under 1-g and 0-g

2.1. Introduction

The governing equations and boundary conditions are presented for the situation of a thin liquid layer emanating from a pressurized vessel and traveling along a horizontal plate with a constant initial height and uniform initial velocity as shown in Fig. 2.1. This situation is the same as channel flow, but since the liquid height is very thin the effect of viscosity must be accounted for. It is desired to find the liquid height at any distance down the length of the plate for different Froude numbers and Reynolds numbers specified at the inlet. Since the inlet Froude number will usually be greater than unity, it is possible that a hydraulic jump will occur at some point in the computational domain. A hydraulic jump is when the flow suddenly changes from supercritical (Fr > 1) to subcritical (Fr < 1) flow, which is accompanied by a sudden increase in the liquid height. This is analogous to the shock wave in gas dynamics when the flow changes from supersonic (M > 1) to subsonic (M < 1) flow in a very short distance. The similarity between the hydraulic jump and the shock wave in gas dynamics suggests using the familiar approach of modeling the flow as a transient phenomena and allowing the solution to march in time to achieve the desired steady state results. The effects of microgravity on the flow is also examined.

2.2. Mathematical Modeling

The generalized governing equations for an incompressible fluid with constant properties are as follows:

Continuity equation:

$$\frac{\partial \rho}{\partial t} + \frac{\partial}{\partial x}(\rho u) + \frac{\partial}{\partial y}(\rho v) + \frac{\partial}{\partial z}(\rho w) = 0$$

y-direction momentum equation:

$$\rho\left(\frac{\partial v}{\partial t}+u\frac{\partial v}{\partial x}+v\frac{\partial v}{\partial y}+w\frac{\partial v}{\partial z}\right)=-\frac{\partial P}{\partial y}-\left(\frac{\partial \tau_{xy}}{\partial x}+\frac{\partial \tau_{yy}}{\partial y}+\frac{\partial \tau_{zy}}{\partial z}\right)+\rho g_y$$

x-direction momentum equation:

$$\rho\left(\frac{\partial u}{\partial t}+u\frac{\partial u}{\partial x}+v\frac{\partial u}{\partial y}-w\frac{\partial u}{\partial z}\right)=-\frac{\partial P}{\partial x}-\left(\frac{\partial \tau_{xx}}{\partial x}+\frac{\partial \tau_{xy}}{\partial y}+\frac{\partial \tau_{zx}}{\partial z}\right)+\rho g_x$$

The general boundary conditions for these equations are those on the flat plate and on the free surface of the liquid:

y=0: u=0, v=0

y=h: $v=\frac{\partial h}{\partial t}+u\frac{\partial h}{\partial x}$

y=h: $P+\frac{\sigma}{\left(1+\left(\frac{\partial h}{\partial x}\right)^2\right)^{3/2}}\frac{\partial h}{\partial x}+\frac{2\rho\nu(1+\delta^2)}{(1-h^2)}\frac{\partial u}{\partial x}=0$

y=h: $p_{n\tau}=0$

where h is the film thickness; $p_{n\tau}$ is the stress tangent to the film surface; and σ is the surface tension.

The following assumptions are introduced to reduce the complexity of the governing equations:

Assumptions:

- Incompressible fluid
- $w=\frac{\partial}{\partial z}=g_z=0$
- Boundary layer assumptions
- No surface tension
- No interfacial shear on the free surface

The governing equations and boundary conditions then reduce to the following forms:

Continuity equation:

$$\frac{\partial u}{\partial x} + \frac{\partial v}{\partial y} = 0$$

y-direction momentum equation:

$$\frac{\partial P}{\partial y} = -\rho g$$

x-direction momentum equation:

$$\frac{\partial u}{\partial t} + u\frac{\partial u}{\partial x} + v\frac{\partial u}{\partial y} = -\frac{1}{\rho} \cdot \frac{\partial P}{\partial x} + \nu\frac{\partial^2 u}{\partial y^2}$$

Boundary conditions:

$P(x, h, t) = 0$

$u(x_1, y, t) = u_1$

$u(x, y, 0) = u_0$

$\left(\frac{\partial u}{\partial y}\right)\Big|_{y=h} = 0$

$v(x, 0, t) = 0$

Integrating the conservation equations across the thin layer results in quasi - one-dimensional governing equations:

Continuity equation:

$$\frac{\partial u}{\partial x} + \frac{\partial v}{\partial y} = 0$$

$$\int_0^h \left(\frac{\partial u}{\partial x}\right) dy + \int_0^h \left(\frac{\partial v}{\partial y}\right) dy = 0$$

Leibniz's rule:

$$\frac{d}{dx}\int_A^B f(x,t)dt = \int_A^B \frac{\partial f(x,t)}{\partial x} dt + f(x,B) \cdot \frac{dB}{dx} - f(x,A) \cdot \frac{dA}{dx}$$

$$\int_0^h \left(\frac{\partial u}{\partial x}\right) dy = \frac{\partial}{\partial x}\int_0^h u dy - (u|_h) \cdot \frac{\partial h}{\partial x}$$

The kinematic condition at the free surface for unsteady problems is used as one of the free surface boundary conditions:

$$\frac{\partial h}{\partial t} + u|_h \cdot \frac{\partial h}{\partial x} = v|_h$$

$$u|_h \cdot \frac{\partial h}{\partial x} = v|_h - \frac{\partial h}{\partial t}$$

$$\frac{\partial}{\partial x}\int_0^h u dy - \left(v|_h - \frac{\partial h}{\partial t}\right) + v|_h - v|_0 = 0$$

$$\bar{u} = \frac{1}{h}\int_0^h u dy$$

$$\frac{\partial}{\partial x}(\bar{u}h) + \frac{\partial h}{\partial t} = 0 \tag{2.1}$$

y-direction momentum equation -

$$\frac{\partial P}{\partial y} = -\rho g$$

$$\int_0^h \left(\frac{\partial P}{\partial y}\right) dy = -\rho g \int_0^h dy$$

$$P = -\rho g y + C$$

$$P = \rho g(h - y) \tag{2.2}$$

x-direction - momentum equation -

$$\frac{\partial u}{\partial t} + u\frac{\partial u}{\partial x} + v\frac{\partial u}{\partial y} = -\frac{1}{\rho}\cdot\frac{\partial P}{\partial x} + \nu\frac{\partial^2 u}{\partial y^2}$$

$$\int_0^h \left(\frac{\partial u}{\partial t}\right)dy + \int_0^h \left(u\frac{\partial u}{\partial x}\right)dy + \int_0^h \left(v\frac{\partial u}{\partial y}\right)dy = -\frac{1}{\rho}\int_0^h \left(\frac{\partial P}{\partial x}\right)dy + \nu\int_0^h \left(\frac{\partial^2 u}{\partial y^2}\right)dy$$

$$\begin{aligned}
\int_0^h \left(\frac{\partial u}{\partial t}\right)dy =& \frac{\partial}{\partial t}\int_0^h u dy - u|_h \cdot \frac{\partial h}{\partial t} \\
=& \frac{\partial}{\partial t}(\bar{u}h) - u|_h \cdot \frac{\partial h}{\partial t} \\
\int_0^h \left(\frac{\partial P}{\partial x}\right)dy =& \frac{\partial}{\partial x}\int_0^h P dy - P|_h \cdot \frac{\partial h}{\partial x} \\
=& \frac{\partial}{\partial x}\int_0^h \rho g(h-y)dy \\
=& \frac{\partial}{\partial x}\left(\frac{1}{2}\rho g h^2\right)
\end{aligned}$$

$$\begin{aligned}
\int_0^h \left(\frac{\partial^2 u}{\partial y^2}\right)dy &= \int_0^h \frac{\partial}{\partial y}\left(\frac{\partial u}{\partial y}\right)dy \\
&= \int_0^h d\left(\frac{\partial u}{\partial y}\right)
\end{aligned}$$

$$\int_0^h \left(v\frac{\partial u}{\partial y}\right)dy = \int_0^h \frac{\partial (uv)}{\partial y}dy - \int_0^h \left(u\frac{\partial v}{\partial y}\right)dy$$

$$\frac{\partial}{\partial t}(\bar{u}h) - u|_h \cdot \frac{\partial h}{\partial t} + \int_0^h \left(u\frac{\partial u}{\partial x}\right)dy + \int_0^h \frac{\partial (uv)}{\partial y}dy - \int_0^h \left(u\frac{\partial v}{\partial y}\right)dy = -\frac{\partial}{\partial x}\left(\frac{1}{2}gh^2\right) + \nu\int_0^h d\left(\frac{\partial u}{\partial y}\right)$$

From the continuity equation

$$\int_0^h \left(u\frac{\partial v}{\partial y}\right)dy = -\int_0^h \left(u\frac{\partial u}{\partial x}\right)dy$$

$$\frac{\partial}{\partial t}(\bar{u}h) - u|_h \cdot \frac{\partial h}{\partial t} + \int_0^h \left(u\frac{\partial u}{\partial x}\right)dy + (uv)|_h - (uv)|_0 + \int_0^h \left(u\frac{\partial u}{\partial x}\right)dy$$

$$= -\frac{\partial}{\partial x}\left(\frac{1}{2}gh^2\right) + \nu\left(\frac{\partial u}{\partial y}\right)\Big|_h - \nu\left(\frac{\partial u}{\partial y}\right)\Big|_0$$

$$\begin{aligned}(uv)|_h &= u|_h \cdot v|_h \\ &= u|_h\left(u|_h \cdot \frac{\partial h}{\partial x} + \frac{\partial h}{\partial t}\right) \\ &= (u|_h)^2 \cdot \frac{\partial h}{\partial x} + u|_h \cdot \frac{\partial h}{\partial t}\end{aligned}$$

$$\int_0^h \left(2u\frac{\partial u}{\partial x}\right)dy = \int_0^h \left[\frac{\partial(u^2)}{\partial x}\right]dy$$

$$\frac{\partial}{\partial t}(\bar{u}h) - u|_h \cdot \frac{\partial h}{\partial t} + \int_0^h \left[\frac{\partial(u^2)}{\partial x}\right]dy + (u|_h)^2 \cdot \frac{\partial h}{\partial x} + u|_h \cdot \frac{\partial h}{\partial t} = -\frac{\partial}{\partial x}\left(\frac{1}{2}gh^2\right) - \nu\left(\frac{\partial u}{\partial y}\right)\Big|_0$$

$$\int_0^h \left[\frac{\partial(u^2)}{\partial x}\right]dy = \frac{\partial}{\partial x}\int_0^h u^2 dy - (u|_h)^2 \cdot \frac{\partial h}{\partial x}$$

$$\frac{\partial}{\partial t}(\bar{u}h) + \frac{\partial}{\partial x}\int_0^h u^2 dy = -\frac{\partial}{\partial x}\left(\frac{1}{2}gh^2\right) - \nu\left(\frac{\partial u}{\partial y}\right)\Big|_0$$

$$\frac{\partial}{\partial t}(\bar{u}h) + \frac{\partial}{\partial x}\left[\int_0^h u^2 dy + \frac{1}{2}gh^2\right] = -\nu\left(\frac{\partial u}{\partial y}\right)\Big|_0 \tag{2.3}$$

The following assumptions were made to simplify the governing equations:

$$\int_0^h u^2 dy \simeq \bar{u}^2 h$$

with an analogy to the Blasius solution of frictional flow over a flat plate where u_∞ is replaced by $\bar{u}$:

$$-\nu\left(\frac{\partial u}{\partial y}\right)\Big|_0 \simeq -\frac{0.332\bar{u}^2}{\sqrt{\bar{u}x/\nu}}$$

In addition:

$$\frac{\partial h}{\partial t} \simeq 0$$

$$\frac{\partial}{\partial t}(\bar{u}h) = \bar{u}\frac{\partial h}{\partial t} + h\frac{\partial \bar{u}}{\partial t} = h\frac{\partial \bar{u}}{\partial t}$$

which resulted in the following governing equations:

$$\bar{u}h = Q = \text{ constant} \tag{2.4}$$

$$h\frac{\partial \bar{u}}{\partial t} + \frac{\partial}{\partial x}\left[\bar{u}^2 h + \frac{1}{2}gh^2\right] = -\frac{0.332\bar{u}^2}{\sqrt{\bar{u}x/\nu}} \tag{2.5}$$

These equations form a system of nonlinear partial differential equations. After the equations are nondimensionalized, the dimensionless liquid height is eliminated from the momentum equation which leaves one nonlinear partial differential equation with one dependent variable which is the dimensionless velocity. The assumption involving the term $\partial h/\partial t$ was made to simplify the governing equations so that the height of the liquid film could be eliminated. By using this assumption, it is understood that the unsteady solutions with respect to time are not accurate, but the accuracy of the steady state solution is not affected. An analysis concerning the term $\int_0^h u^2 dy$ is given in Appendix 2.1.

Dimensionless variables:

$$\frac{\bar{u}}{\bar{u}_1} = V \qquad \frac{h}{h_1} = \delta \qquad \frac{x}{h_1} = \xi$$

$$t\frac{\bar{u}_1}{h_1} = \tau \qquad \frac{\bar{u}_1^2}{gh_1} = Fr_1^2 \qquad \frac{\bar{u}_1 h_1}{\nu} = Re_1$$

$$\bar{u} = \bar{u}_1 V \qquad h = h_1\delta \qquad x = h_1\xi \qquad t = \frac{h_1\tau}{\bar{u}_1}$$

x-direction momentum equation:

$$h(\bar{u})_t + (\bar{u}^2 h + \frac{1}{2} g h^2)_x = -\frac{0.332\bar{u}^2}{\sqrt{\bar{u}x/\nu}}$$

$$(h_1\delta)\frac{\partial(\bar{u}_1 V)}{\partial(h_1\tau/\bar{u}_1)} + \frac{\partial}{\partial(h_1\xi)}\left[(\bar{u}_1 V)^2(h_1\delta) + \frac{1}{2}g(h_1\delta)^2\right] = -0.332(\bar{u}_1 V)^2 \Big/ \sqrt{\frac{(\bar{u}_1 V)(h_1\xi)}{\nu}}$$

$$\bar{u}_1^2 \cdot \delta\frac{\partial V}{\partial \tau} + \bar{u}_1^2 \cdot \frac{\partial}{\partial \xi}\left(V^2\delta + \frac{g h_1 \delta^2}{2\bar{u}_1^2}\right) = -0.332\bar{u}_1^2 V^2 \Big/ \sqrt{\frac{\bar{u}_1 h_1}{\nu} \cdot V\xi}$$

$$\delta(V)_\tau + \left(V^2\delta + \frac{1}{2Fr_1^2} \cdot \delta^2\right)_\xi = -\frac{0.332V^2}{\sqrt{Re_1 V\xi}}$$

$$\delta(V)_\tau + \left(V^2\delta + \frac{1}{2Fr_1^2} \cdot \delta^2\right)_\xi = -\frac{0.332V^{3/2}}{\sqrt{Re_1\xi}}$$

Continuity equation:

$$\bar{u}h = Q$$

$$(\bar{u}_1 V)(h_1\delta) = Q$$

$V\delta$ = constant =1 or $\delta = \frac{1}{V}$. Substituting and dividing by $\frac{1}{\delta}$ gives:

$$(V)_\tau + \frac{1}{\delta}\left(V + \frac{1}{2Fr_1^2} \cdot \frac{1}{V^2}\right)_\xi = \frac{1}{\delta}\left(\frac{-0.332V^{3/2}}{\sqrt{Re_1\xi}}\right)$$

$$(V)_\tau + V\left(V + \frac{1}{2Fr_1^2} \cdot \frac{1}{V^2}\right)_\xi = -\frac{0.332V^{5/2}}{\sqrt{Re_1\xi}}$$

Dimensionless governing equation:

$$V_\tau + VG_\xi = H \tag{2.6}$$

where

$$G = V + \frac{1}{2Fr_1^2} \cdot \frac{1}{V^2} \qquad ; \qquad H = -\frac{0.332V^{5/2}}{\sqrt{Re_1 \xi}} \tag{2.7}$$

For the case when the gravity is zero, the equation for G is as follows:

$$G = V$$

The governing equation has one time derivative and one space derivative, so an initial condition and a boundary value are needed.

Initial condition:

$\tau = 0 : \qquad V = V_0 = 1.0$ for $\xi_1 \leq \xi \leq \xi_n$

Boundary condition:

$\xi = \xi_1 : \qquad Fr = Fr_1, \quad V = 1$

2.3. Numerical solution procedure

Due to the similarity between the hydraulic jump and the shock wave in gas dynamics the MacCormack explicit method, which is quite often used for the solution of compressible flow problems, will be used in the present numerical analysis. Since it is an explicit method, the unknown variables are found in terms of known quantities, as opposed to implicit methods which must solve a matrix equation to obtain the solution of the problem.

The MacCormack method is a two-step scheme that uses first-order finite-difference approximations. The scheme first predicts the solution at the next time step with a forward time, forward space (FTFS) differencing scheme and then corrects the prediction with a forward time, backward space (FTBS) scheme. This results in a approximation that is second-order accurate in both time and space (Hankey, 1982).

When applied to the one-dimensional linear convection equation,

$$\frac{\partial u}{\partial t} + c\frac{\partial u}{\partial x} = 0$$

the MacCormack method yields (Anderson et al., 1984)

$$\overline{u_j^{n+1}} = u_j^n - c\frac{\Delta t}{\Delta x}(u_{j+1}^n - u_j^n) \qquad \text{Forward predictor}$$

$$u_j^{n+1} = \frac{1}{2}\left[u_j^n + \overline{u_j^{n+1}} - c\frac{\Delta t}{\Delta x}(\overline{u_j^{n+1}} - \overline{u_{j-1}^{n+1}})\right] \qquad \text{Backward corrector}$$

The backward corrector can be seen as an arithmetic average of the old solution, u_j^n, and the new solution based on the predicted solution, $\overline{u_j^{n+1}} - c\frac{\Delta t}{\Delta x}(\overline{u_j^{n+1}} - \overline{u_{j-1}^{n+1}})$, which uses a backward difference.

The governing equation for the present problem is as follows:

$$V_\tau + VG_\xi = H \quad , \quad G = V + \frac{1}{2Fr_1^2}\cdot\frac{1}{V^2} \quad , \quad H = -\left(\frac{0.332V^{5/2}}{\sqrt{Re_1\xi}}\right)$$

Forward predictor: FTFS

$$\frac{\overline{V_j^{n+1}} - V_j^n}{\Delta\tau} + V_j^n\left[\frac{G_{j+1}^n - G_j^n}{\Delta\xi}\right] = H_j^n$$

$$\overline{V_j^{n+1}} = V_j^n - V_j^n\cdot\frac{\Delta\tau}{\Delta\xi}(G_{j+1}^n - G_j^n) + \Delta\tau H_j^n$$

$$\overline{V_j^{n+1}} = V_j^n\left[1 - \frac{\Delta\tau}{\Delta\xi}(G_{j+1}^n - G_j^n)\right] + \Delta\tau H_j^n \qquad (2.8)$$

Backward corrector: FTBS

The finite-difference equation based on the predicted solution using a forward time, backward space differencing scheme is as follows

$$\frac{(\overline{V_j^{n+1}})' - \overline{V_j^{n+1}}}{\Delta\tau} + \overline{V_j^{n+1}}\left[\frac{\overline{G_j^{n+1}} - \overline{G_{j-1}^{n+1}}}{\Delta\xi}\right] = \overline{H_j^{n+1}}$$

$$(\overline{V_j^{n+1}})' = \overline{V_j^{n+1}} - \frac{\Delta\tau}{\Delta\xi} \cdot \overline{V_j^{n+1}}\left(\overline{G_j^{n+1}} - \overline{G_{j-1}^{n+1}}\right) + \Delta\tau \overline{H_j^{n+1}}$$

$$(\overline{V_j^{n+1}})' = \overline{V_j^{n+1}}\left[1 - \frac{\Delta\tau}{\Delta\xi}\left(\overline{G_j^{n+1}} - \overline{G_{j-1}^{n+1}}\right)\right] + \Delta\tau \overline{H_j^{n+1}}$$

The corrected solution is the arithmetic average of the past and predicted solutions

$$V_j^{n-1} = \frac{1}{2}[V_j^n + (\overline{V_j^{n+1}})']$$

$$V_j^{n+1} = \frac{1}{2}\left\{V_j^n + \overline{V_j^{n+1}}\left[1 - \frac{\Delta\tau}{\Delta\xi}\left(\overline{G_j^{n+1}} - \overline{G_{j-1}^{n+1}}\right)\right] + \Delta\tau \overline{H_j^{n+1}}\right\} \tag{2.9}$$

where

$$G_j^n = V_j^n + \frac{1}{2Fr_1^2}\left(\frac{1}{V_j^n}\right)^2 \tag{2.10}$$

$$H_j^n = -\frac{0.332(V_j^n)^{5/2}}{\sqrt{Re_1 \xi_j}} \tag{2.11}$$

$$\overline{G_j^{n+1}} = \overline{V_j^{n+1}} + \frac{1}{2Fr_1^2}\left(\frac{1}{\overline{V_j^{n+1}}}\right)^2 \tag{2.12}$$

$$\overline{H_j^{n+1}} = -\frac{0.332(\overline{V_j^{n+1}})^{5/2}}{\sqrt{Re_1 \xi_j}} \tag{2.13}$$

Since the forward predictor velocity is in terms of a forward-space approximation, an outlet boundary condition on the velocity is needed. For the case of 1-g, it is assumed that the Froude number at the outlet is unity, which is a common boundary condition when a liquid falls over an edge because the liquid accelerates from a subcritical velocity to the critical velocity. The Froude number and the dimensionless velocity are related as follows:

$$Fr_1^2 = \frac{\bar{u}_1^2}{gh_1} \qquad Fr^2 = \frac{\bar{u}^2}{gh}$$

$$\frac{Fr^2}{Fr_1^2} = \frac{(\bar{u}_1 V)^2}{g(h_1\delta)} \cdot \frac{gh_1}{\bar{u}_1^2} = \frac{V^2}{\delta} = V^3$$

$$V = \left(\frac{Fr}{Fr_1}\right)^{2/3}$$

$$V_n = \left(\frac{Fr_n}{Fr_1}\right)^{2/3} = \left(\frac{1}{Fr_1}\right)^{2/3} = Fr_1^{-2/3}$$

For the microgravity case, the slope at the last node is set equal to the slope at the next to last node.

The solution of the governing equation using the MacCormack explicit method proceeds as follows:

- The parameters pertaining to the numerical domain and the inlet and outlet boundary conditions are specified.
- The initial velocity distribution is input to the program.
- The variables G and H are computed using the velocity profile at the old time step as given in eqs. (2.10, 2.11).
- The velocity distribution at the midpoint time step is calculated in terms of the velocity, G, and H at the old time step as shown in eq. (2.8). An outlet boundary condition is needed at this step because of the forward-space approximation.
- The variables G and H are computed again by using the velocity profile at the midpoint time step as presented in eqs. (2.12, 2.13).
- The velocity distribution at the new time step is calculated using eq. (2.9). The inlet boundary condition is used in this step because of the backward-space approximation.

- The values of the velocity distribution at the new time step are used as the initial velocity profile for the next iteration.
- The process is repeated until steady values are reached.

PSEUDO-CODE FOR CHANNEL FLOW

---

* Input parameters *

$Fr_1,\ Re_1,\ V_1,\ \xi_1,\ \xi_n,\ \Delta\tau,\ \Delta\xi$

---

* Input initial velocity distribution at the old time step *

$VOLD(I) = 1$

---

* Compute G and H at the old time step *

10 $GOLD(I) = GOLD(VOLD(I),\ Fr_1)$

$HOLD(I) = HOLD(VOLD(I),\ Re_1,\ \xi(I))$

---

* Compute V at the mid time step *

$VMID(I) = VMID(VOLD(I),\ \Delta\tau,\ \Delta\xi,\ GOLD(I+1),\ HOLD(I))$

---

* Compute G and H at the mid time step *

$GMID(I) = GMID(VMID(I),\ Fr_1)$

$HMID(I) = HMID(VMID(I),\ Re_1,\ \xi(I))$

---

* Compute V at the new time step *

$VNEW(I) = VNEW(VOLD(I),\ VMID(I),\ GMID(I),\ GMID(I-1),\ HMID(I))$

---

* Test for convergence *

---

* Let V at the new time step be V at the old time step *

VOLD(I) = VNEW(I)

GOTO 10

---

* Print results *

2.4. Analytical Solution for Microgravity

The gravity term in the conservation of axial momentum equation can be set to zero to simulate a microgravity situation. For one-dimensional steady flow, the conservation of mass and axial momentum are as follows:

$$Q = uh = \text{constant}$$

$$\frac{d}{dx}\left(\frac{u^2}{2} + gh\right) = -\frac{C_f}{2}\frac{u^2}{h}$$

where

$$\begin{aligned} C_f &= 0.664\sqrt{\frac{\nu}{xu}} \\ &= 0.664\sqrt{\frac{\nu h}{xu_1 h_1}} \end{aligned}$$

Setting g = 0 results in:

$$u\frac{du}{dx} = -\frac{C_f}{2}\frac{u^2}{h}$$

The liquid film height can be eliminated from both equations with the following result:

$$u^{-2}\,du = -\frac{C_f}{2Q}\,dx$$

Integrating this equation gives:

$$\frac{C_f}{2Q}x - \frac{1}{u} = C_1$$

The integration constant is found with the following boundary condition:

$$x = x_1: \quad u = u_1, \quad h = h_1$$

$$\frac{u}{u_1} = \frac{1 - \frac{C_f}{2}\frac{x}{h}}{1 - \frac{C_f}{2}\frac{x_1}{h_1}} = \frac{h_1}{h}$$

This equation is solved for h:

$$\frac{h}{h_1} = \frac{C_f}{2}\frac{x_1}{h_1}\frac{x}{x_1} + \left(1 - \frac{C_f}{2}\frac{x_1}{h_1}\right)$$

$$h = \frac{C_f}{2}x - \frac{C_f}{2}x_1 + h_1$$

$$h = \frac{C_f}{2}(x - x_1) + h_1$$

$$h = 0.332\sqrt{\frac{\nu h}{x u_1 h_1}}(x - x_1) + h_1$$

This equation has been solved for the following conditions:

$\nu = 1.55 \times 10^{-3} \ \frac{\text{in}^2}{\text{sec}}$

$u_1 = 3.93 \ \frac{\text{in}}{\text{sec}}$

$h_1 = 0.01$ in

$x_1 = 2.0$ in

which corresponds to an inlet Reynolds number of $\text{Re}_1 = 25.36$.

2.5. Results and Discussion

The results of the computer program for 1-g are shown Figures 2.2 - 2.7. The figures show the converged solutions of the problem with inlet Froude numbers ranging from 1.0 to 6.0 and inlet Reynolds ranging from 12.68 to 76.06. In the 1-g situation, it is observed that a hydraulic jump is predicted and the location of the jump changes with the Froude number. At very low Froude numbers, the jump is located almost at the liquid inlet. As the Froude

number increases, the jump is pushed back away from where the liquid enters the numerical domain, which is what has been seen experimentally.

Figures 2.8 - 2.10 present solutions of the problem under microgravity conditions for inlet Reynolds numbers of 25.36, 50.71, and 101.4. Figure 2.8 also presents the analytical results of the case under 0-g. For the microgravity simulation, the results are quite different than the results of the 1-g simulation because a hydraulic jump is not predicted. The liquid film height increases monotonically along the length of the plate. It is shown in the graphs that as the Reynolds number increases, the liquid film height becomes smaller. Figure 2.8 shows the excellent agreement between the analytical and numerical solutions for 0-g.

Figure 2.11 presents the dimensionless liquid film height for the case when the slope at the outlet is set equal to the slope of the node just inside the computational domain. It was found that the solution did not converge with this outlet boundary condition.

Figures 2.12 - 2.15 present the results of the 1-g simulation when the friction at the wall is increased by a factor of three. The graphs show that as the friction increases, two phenomena occur: the thickness of the film increases, and the location of the hydraulic jump is closer to the entrance than when the friction is less. This is what one would expect in a physical situation.

C-2

2.6 References

Hankey, W.L., 1982, "Introduction to Computational Aerodynamics," AFWAL-TR-82-3031.

Anderson, D.A., Tannehill, J.C. and Pletcher, R.H., 1984, *Computational Fluid Mechanics and Heat Transfer*, Hemisphere Publishing Corp.

Appendix 2.1

The following is an analysis of the validity of the assumption concerning the term $\int_0^h u^2 dy$. The following approximation is given:

$$\int_0^h u^2 dy \simeq \bar{u}^2 h$$

whereas by the definition of the mean velocity:

$$\bar{u} = \frac{1}{h}\int_0^h u dy$$

$$\bar{u}^2 h = \frac{1}{h}\left[\int_0^h u dy\right]^2$$

It is therefore necessary to determine whether the following equation is accurate:

$$\int_0^h u^2 dy \stackrel{?}{=} \frac{1}{h}\left[\int_0^h u dy\right]^2$$

Since the flow situation is similar to boundary layer flow, a modified approximate solution to the boundary layer velocity profile will be used to examine the approximation.

$$u = V_\infty sin\left(\frac{\pi}{2}\cdot\frac{y}{h}\right)$$

$$\int_0^h u^2 dy = \int_0^h \left[V_\infty sin\left(\frac{\pi}{2}\cdot\frac{y}{h}\right)\right]^2 dy$$

$$= V_\infty^2 \int_0^h sin^2\left(\frac{\pi}{2}\cdot\frac{y}{h}\right) dy$$

$$U = \frac{\pi}{2}\cdot\frac{y}{h}$$

$$dU = \frac{\pi}{2}\cdot\frac{dy}{h}$$

$$dy = \frac{2h}{\pi} dU$$

$$\int_0^h u^2 dy = V_\infty^2 \int_0^{\pi/2} sin^2 U\left(\frac{2h}{\pi} dU\right)$$

$$= \frac{2hV_\infty^2}{\pi}\int_0^{\pi/2} sin^2 U dU$$

$$= \frac{2hV_\infty^2}{\pi}\left[\frac{1}{2}U - \frac{1}{4}sin2U\right]_0^{\pi/2}$$

$$= \frac{hV_\infty^2}{2} = 0.5hV_\infty^2$$

$$\int_0^h u^2 dy = 0.5hV_\infty^2 \tag{5}$$

$$\begin{aligned}
\int_0^h u dy &= \int_0^h V_\infty sin\left(\frac{\pi}{2} \cdot \frac{y}{h}\right) dy \\
&= \int_0^{\pi/2} V_\infty sinU\left(\frac{2h}{\pi} dU\right) \\
&= \frac{2hV_\infty}{\pi} \int_0^{\pi/2} sinU\, dU \\
&= \frac{2hV_\infty}{\pi}
\end{aligned}$$

$$\begin{aligned}
\frac{1}{h}\left[\int_0^h u dy\right]^2 &= \frac{1}{h}\left[\frac{2hV_\infty}{\pi}\right]^2 \\
&= \frac{4hV_\infty^2}{\pi^2}
\end{aligned}$$

$$\frac{1}{h}\left[\int_0^h u dy\right]^2 = \frac{4hV_\infty^2}{\pi^2} = 0.405hV_\infty^2 \tag{6}$$

For this particular velocity profile, the approximation for the term $\int_0^h u^2 dy$ is within 20% of the exact value. Therefore, it is recommended that the approximation be used in the present analysis.

Fig. 2.1 The coordinate system for channel flow

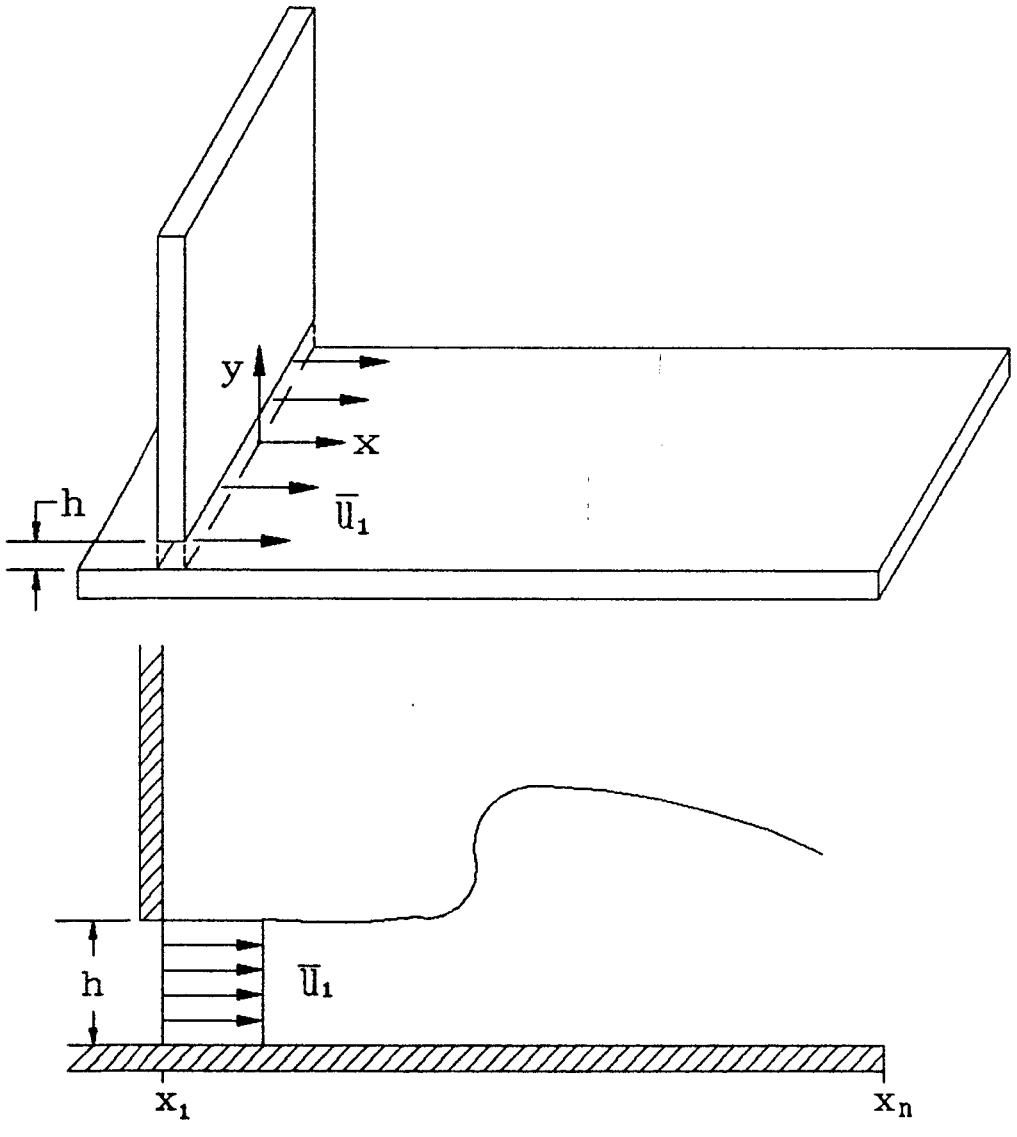

Fig. 2.2 Dimensionless liquid height versus dimensionless distance for channel flow with FR1=1.0, RE1=12.68, $Fr_n = 1.0$

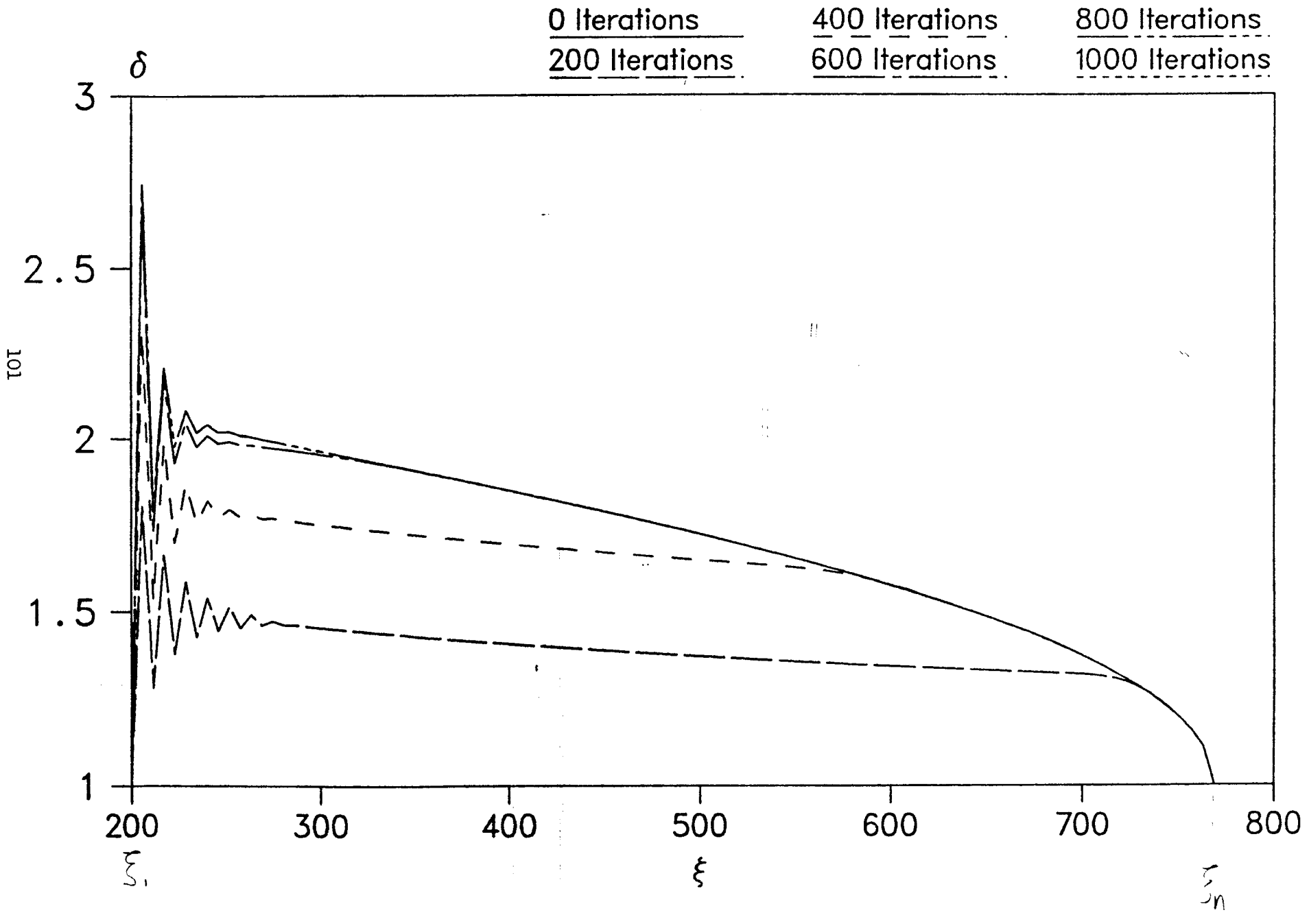

Fig. 2.3 Dimensionless liquid height versus dimensionless distance for channel flow with FR1=2.0, RE1=25.36, $Fr_n = 1.0$

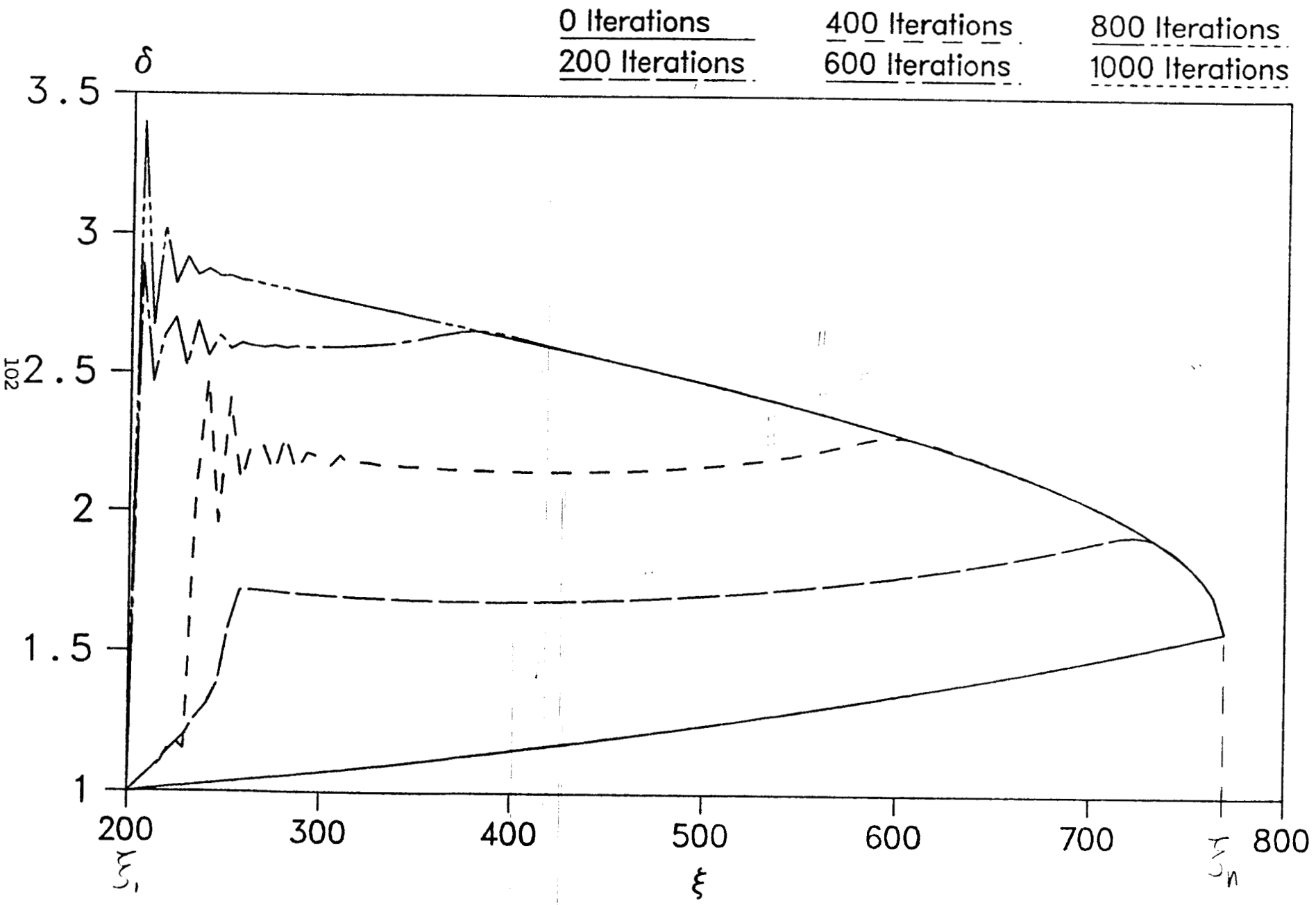

Fig. 2.4 Dimensionless liquid height versus dimensionless distance for channel flow with FR1=3.0, RE1=38.04, $Fr_n = 1.0$

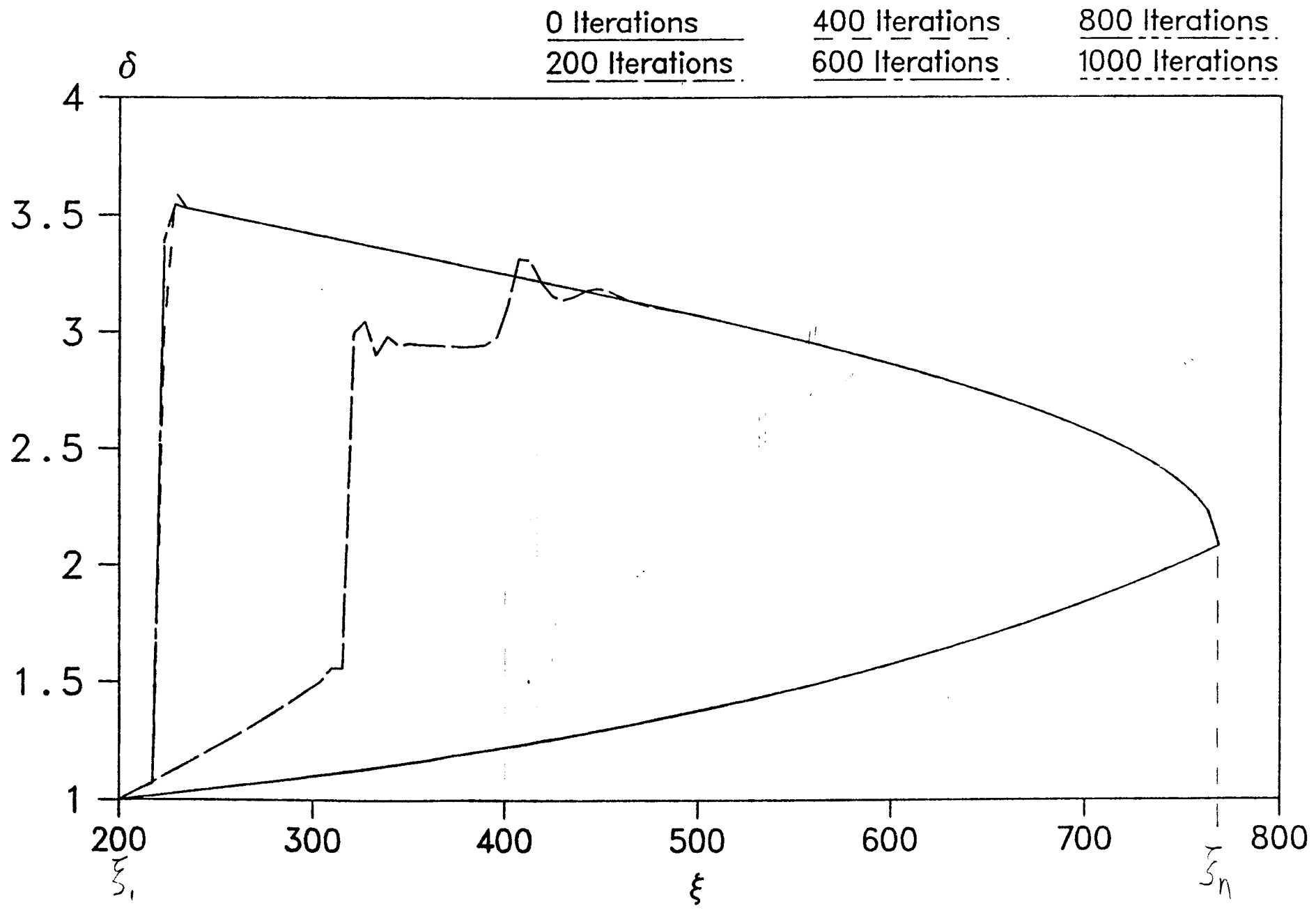

Fig 2.5 Dimensionless liquid height versus dimensionless distance for channel flow with FR1=4.0, RE1=50.72, $Fr_n = 1.0$

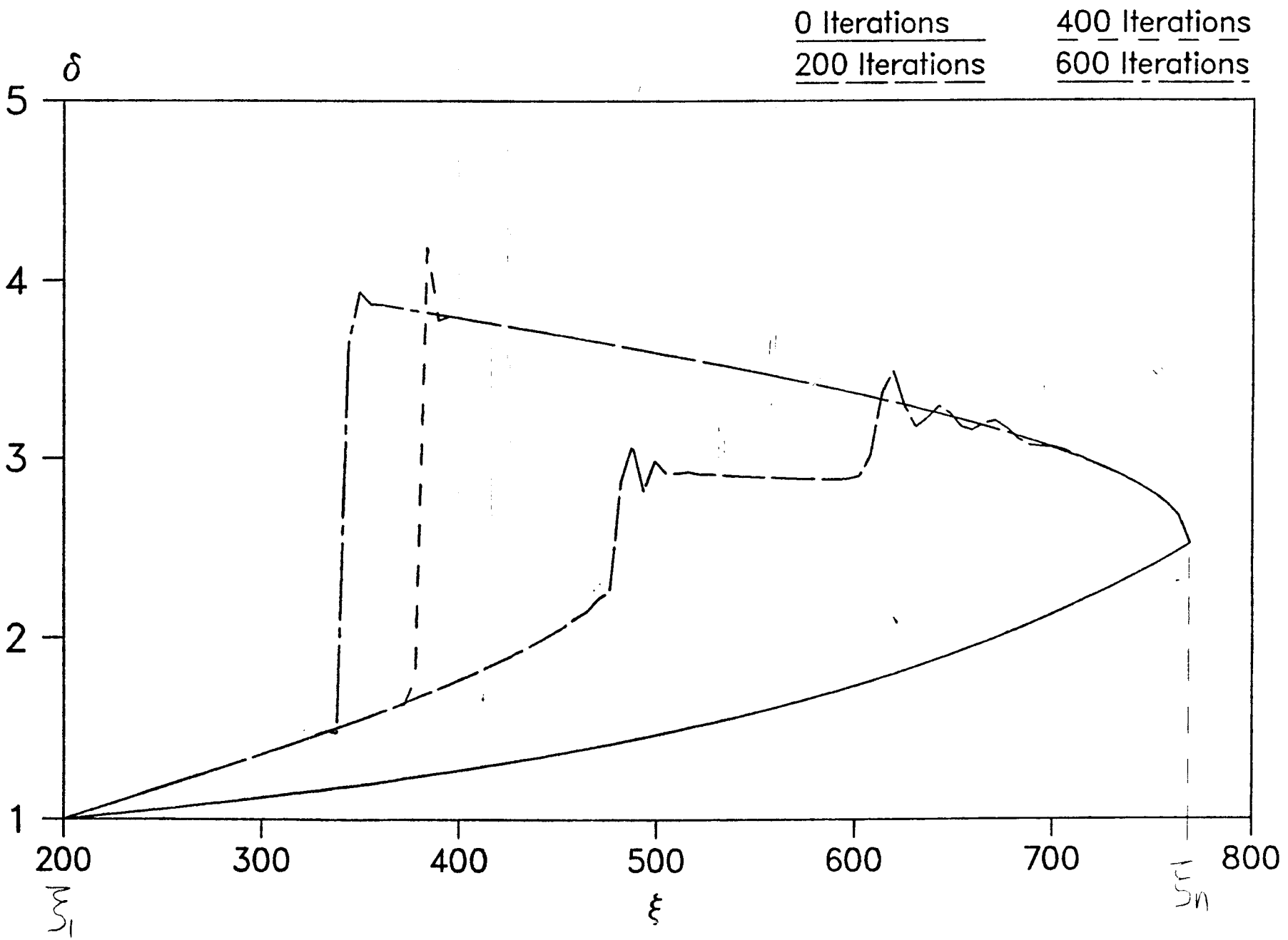

Fig. 2.6. Dimensionless liquid height versus dimensionless distance for channel flow with FR1=5.0, RE1=63.41, $Fr_n = 1.0$

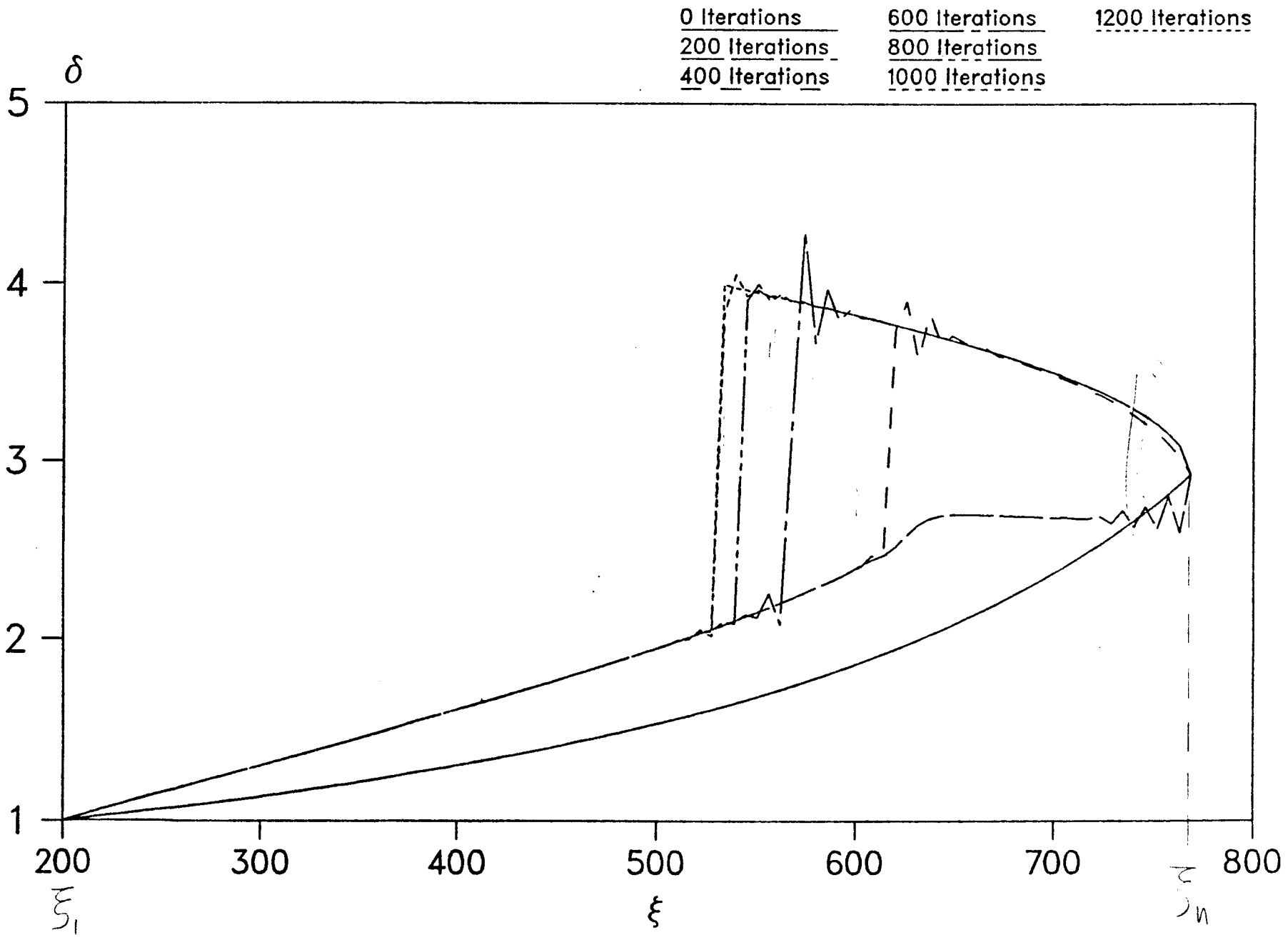

Fig 3.27 Dimensionless liquid height versus dimensionless distance for channel flow with FR1=6.0, RE1=76.06, $Fr_n = 1.0$

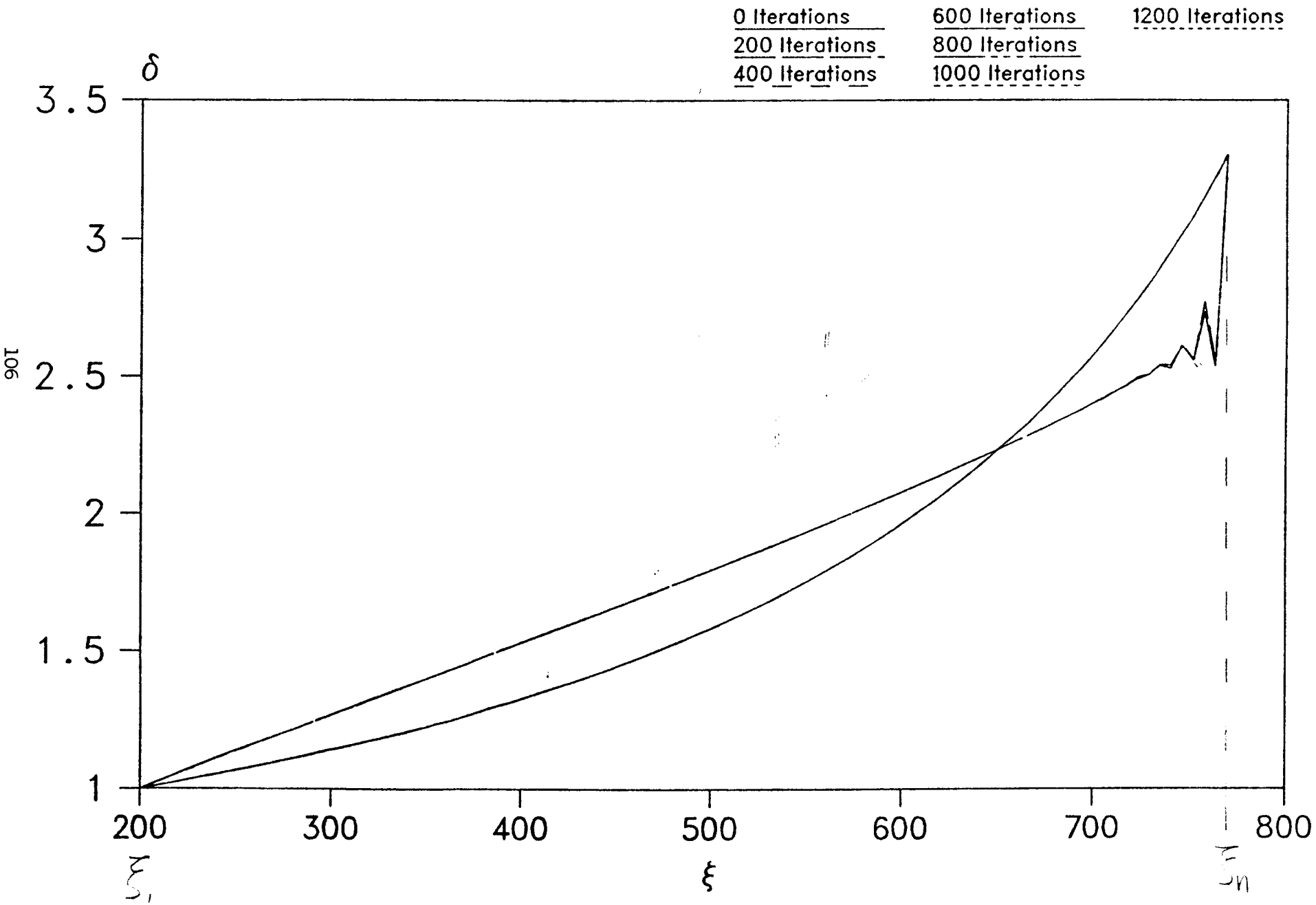

Fig. 2.9 Dimensionless liquid height versus dimensionless distance for channel flow for microgravity simulation with RE1=25.36

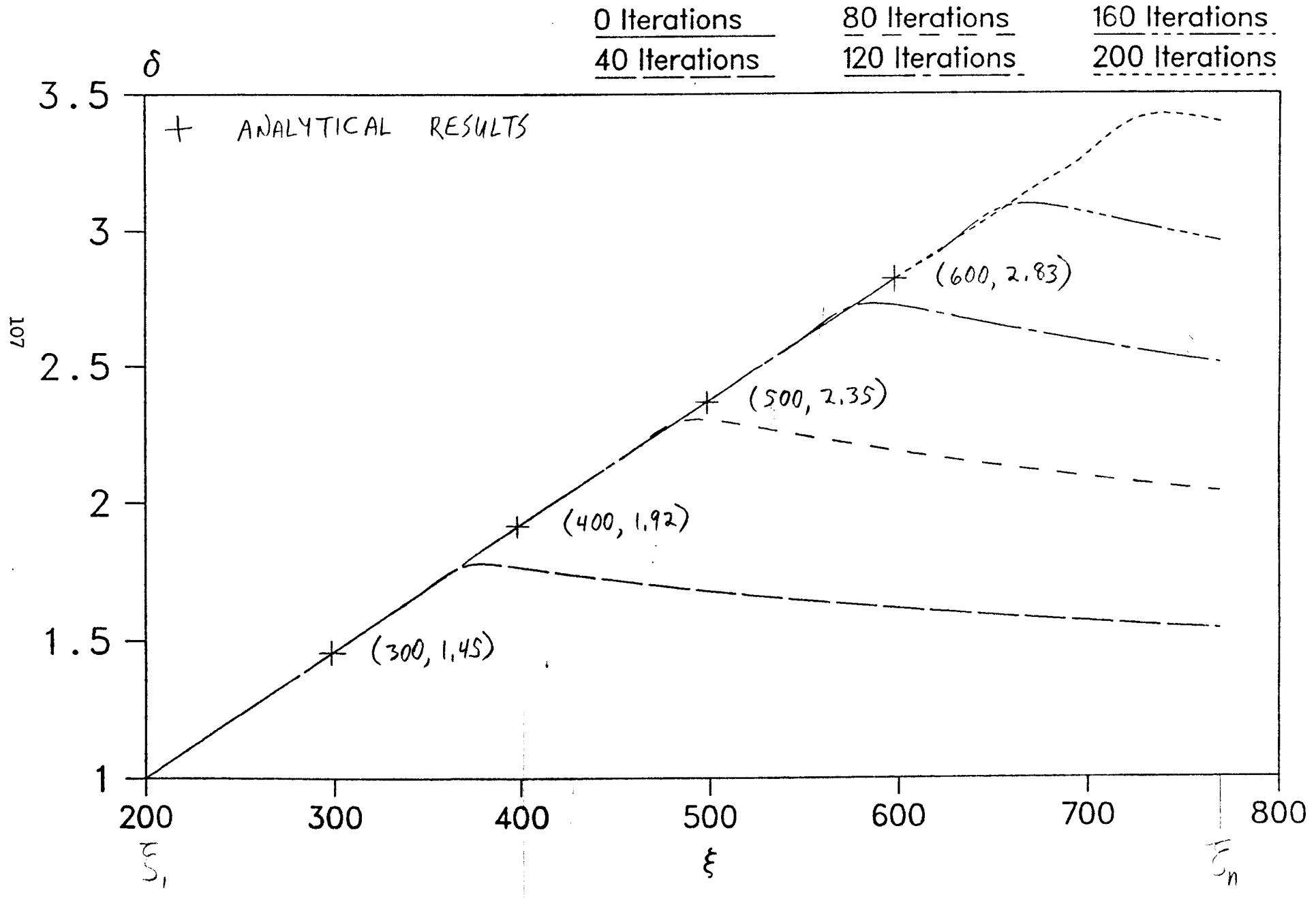

Fig. 2.9 Dimensionless liquid height versus dimensionless distance for channel flow with RE1=50.71 and microgravity simulation

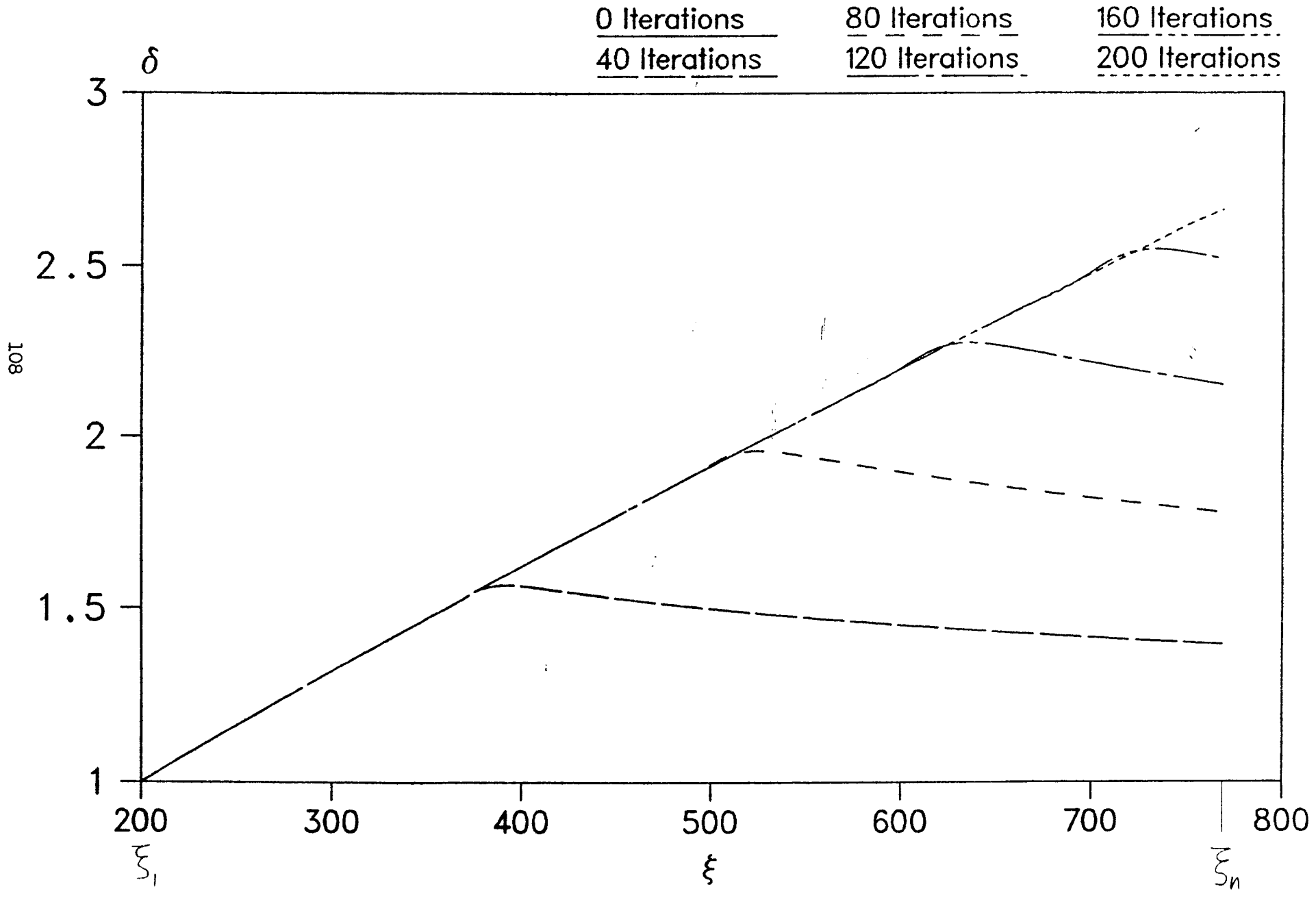

Fig. 2.10 Dimensionless liquid height versus dimensionless distance for channel flow for microgravity simulation with RE1=101.4

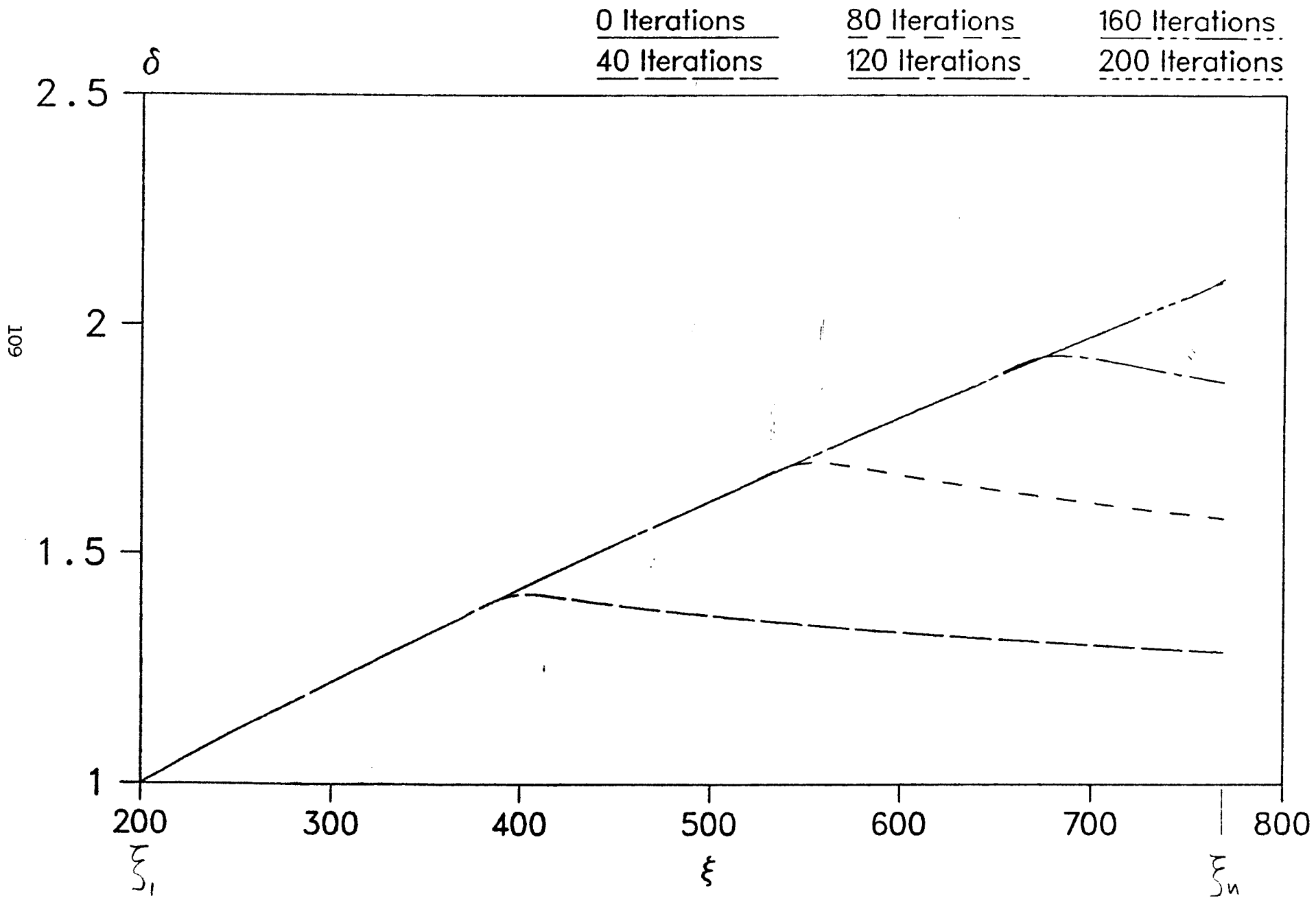

Dimensionless liquid height versus dimensionless distance for channel flow $Fr_1 = 4.0$

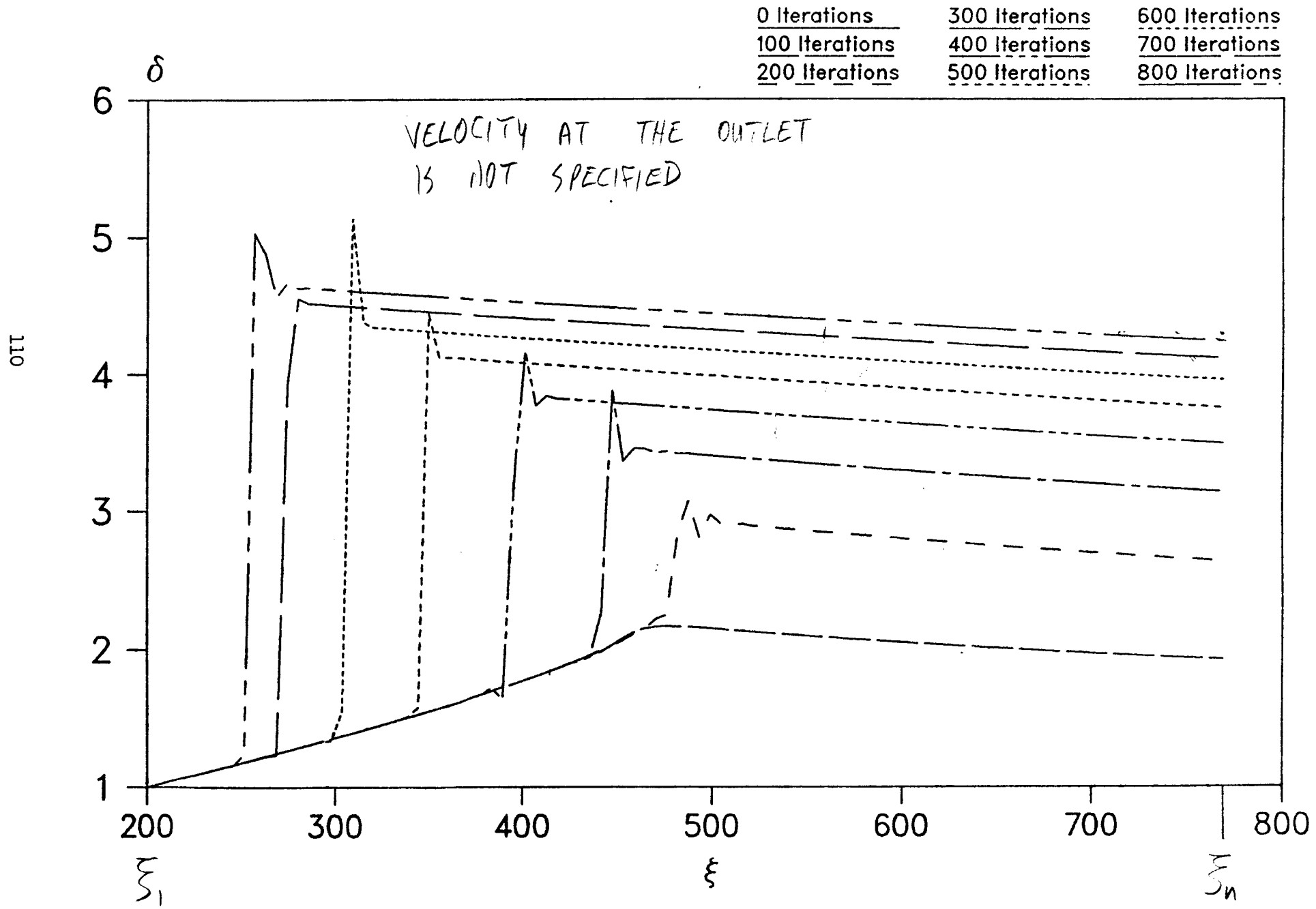

Dimensionless liquid height versus dimensionless distance
for channel flow with the Blasius friction factor increased with
Fr_1=2.0, Fr_n=1.0, Re_1=25.36, ξ_1=200.0, ξ_n=768.6,

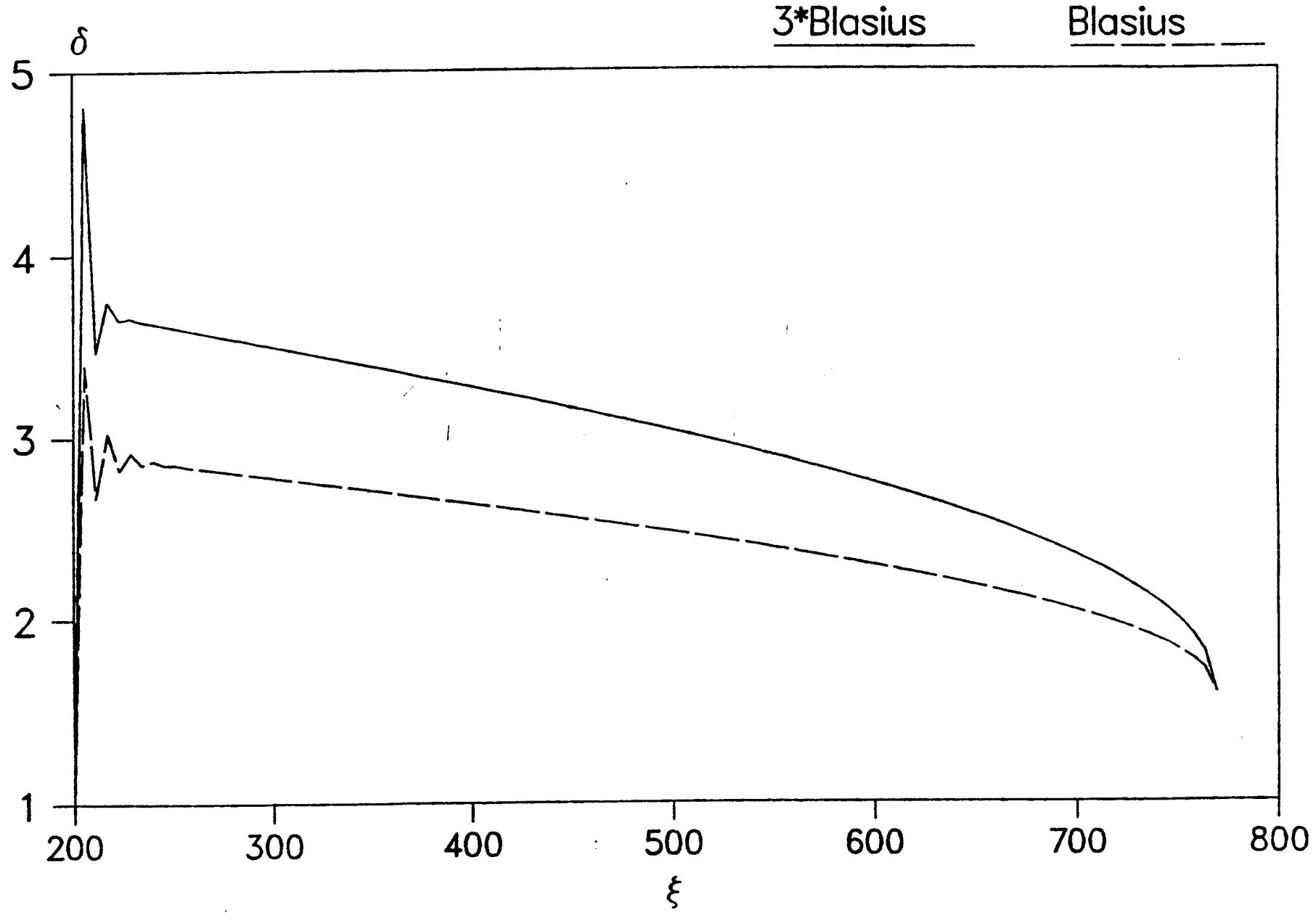

Dimensionless liquid height versus dimensionless distance for channel flow with the Blasius friction factor increased with Fr_1=3.0, Fr_n=1.0, Re_1=38.04, ξ_1=200.0, ξ_n=768.9

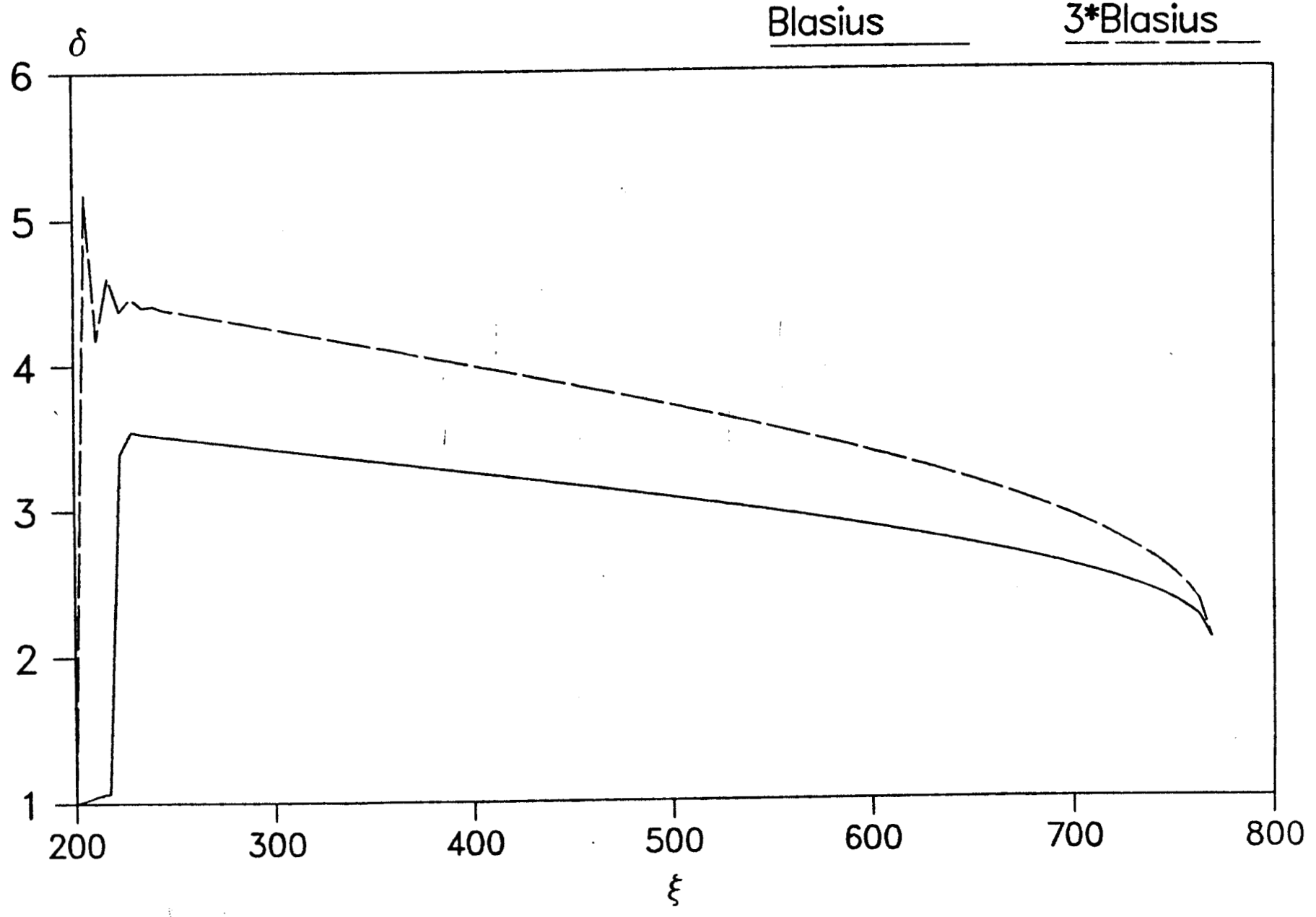

Dimensionless liquid height versus dimensionless distance
for channel flow with the Blasius friction factor increased with
Fr_1=4.0, Fr_n=1.0, Re_1=50.72, ξ_1=200.0, ξ_n=768.9

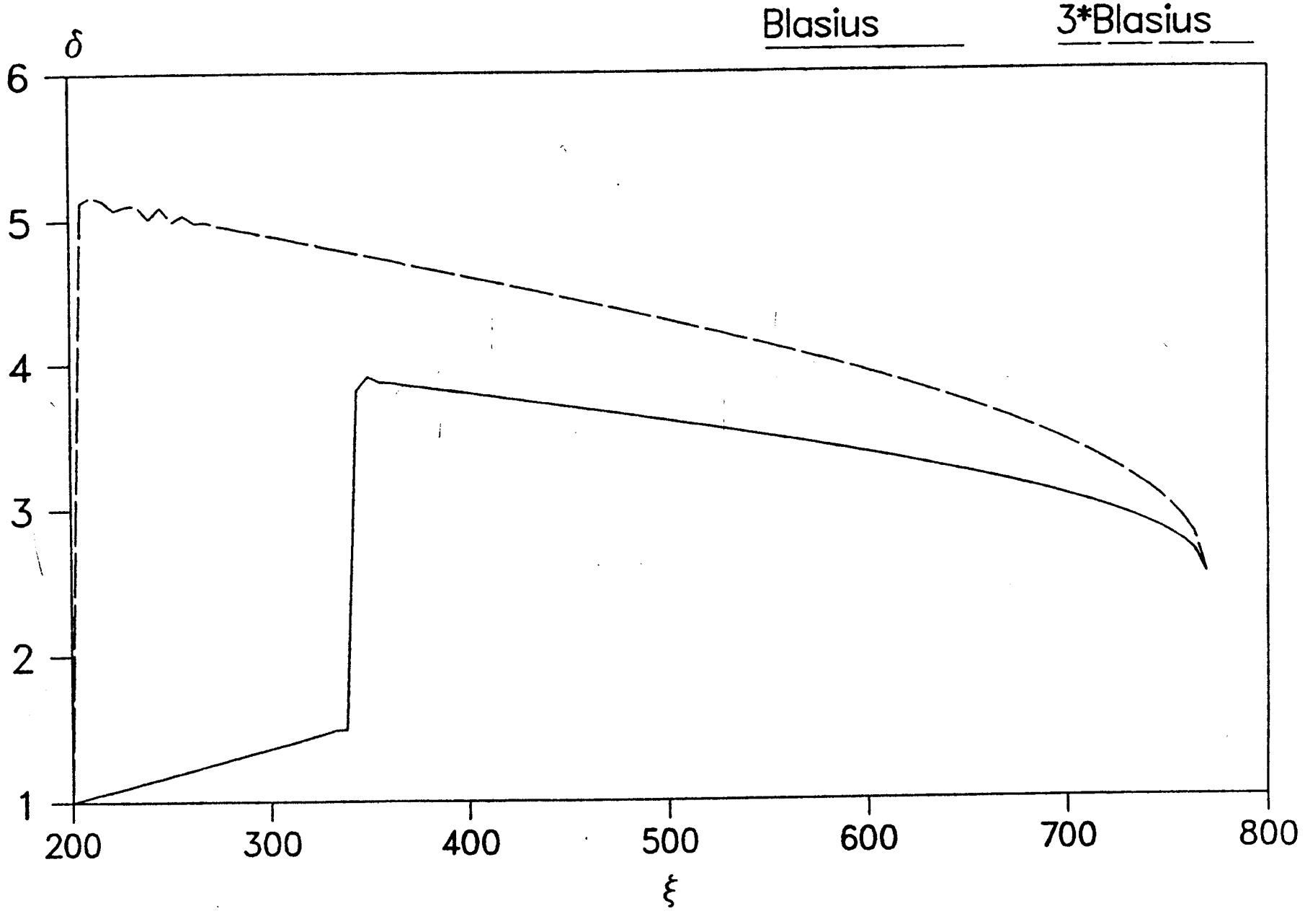

Fig. 2.15 Dimensionless liquid height versus dimensionless distance for channel flow with the Blasius friction factor increased with Fr_1=8.0, Fr_n=1.0, Re_1=101.4, ξ_1=200.0, ξ_n=768.9

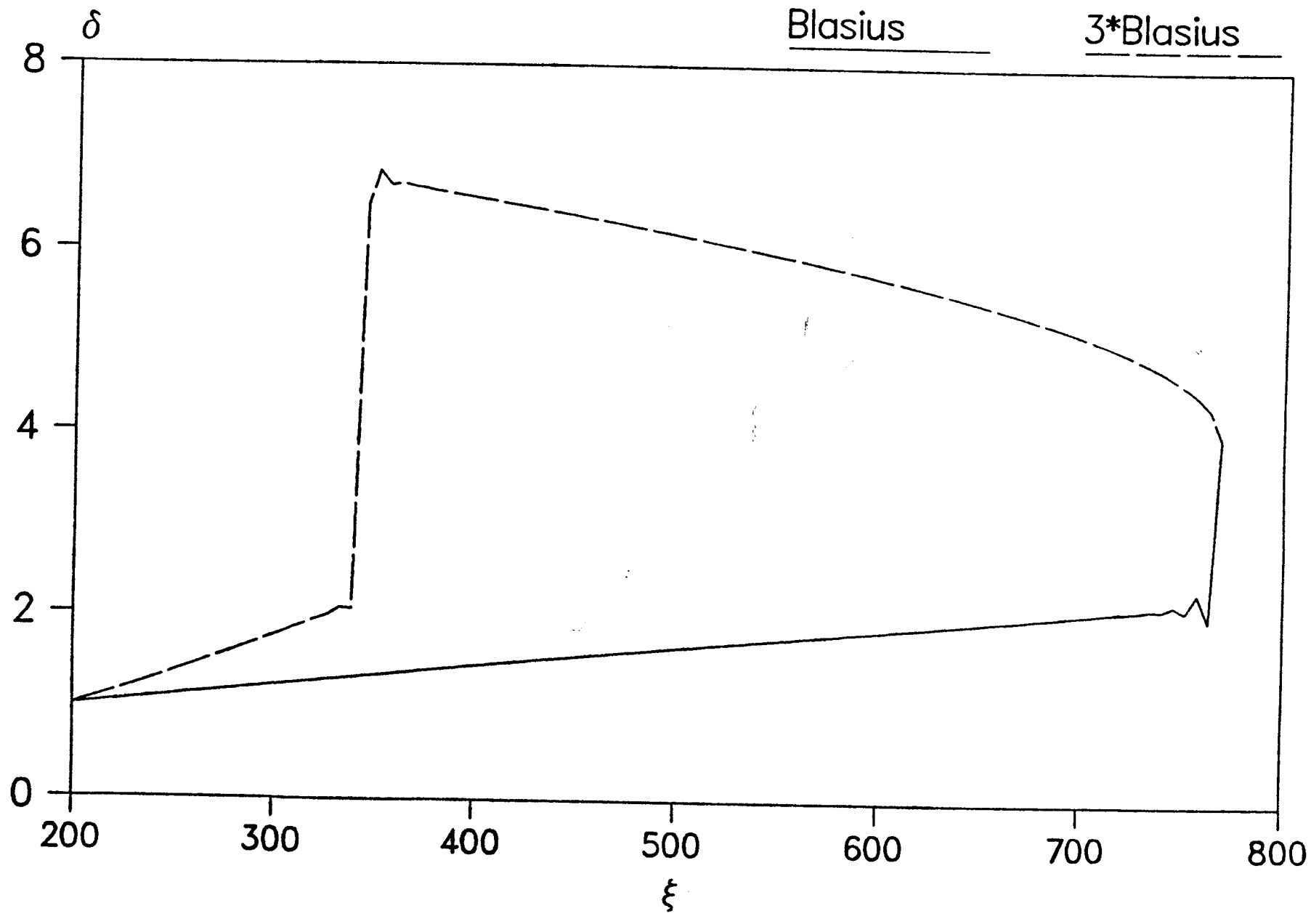

One-dimensional radial flow analysis including solid-body rotation under 1-g and 0-g

3.1. Introduction

The governing equations and boundary conditions are presented for the situation of a thin liquid layer emanating from a pressurized vessel and traveling radially along a horizontal disk with a constant initial height and uniform initial velocity as shown in Fig. 3.1. It is desired to find the liquid height at any distance along the radius of the disk for different Froude numbers and Reynolds numbers specified at the inlet. Since the inlet Froude number will usually be greater than unity, it is possible that a hydraulic jump will occur at some point in the computational domain. A hydraulic jump is when the flow suddenly changes from supercritical (Fr > 1) to subcritical (Fr < 1) flow, which is accompanied by a sudden increase in the height of the liquid. This is analogous to the shock wave in gas dynamics when the flow changes from supersonic (M > 1) to subsonic (M < 1) flow in a very short distance. The similarity between the hydraulic jump and the shock wave in gas dynamics suggests using the familiar approach of modeling the flow as a transient phenomena and allowing the solution to march in time to achieve the desired steady state results. The effects of microgravity and solid-body rotation on the flow are examined.

3.2. Mathematical Modeling

The generalized governing equations for an incompressible fluid with constant properties are as follows:

r-direction momentum equation:

$$\rho\left(\frac{\partial u}{\partial t}+u\frac{\partial u}{\partial r}+\frac{v}{r}\frac{\partial u}{\partial \theta}-\frac{v^2}{r}+w\frac{\partial u}{\partial z}\right)=-\frac{\partial P}{\partial r}+\mu\left(\frac{\partial^2 u}{\partial r^2}+\frac{1}{r}\frac{\partial u}{\partial r}-\frac{u}{r^2}+\frac{1}{r^2}\frac{\partial^2 u}{\partial \theta^2}-\frac{2}{r^2}\frac{\partial v}{\partial \theta}+\frac{\partial^2 u}{\partial z^2}\right)+\rho g_r$$

θ-direction momentum equation:

$$\rho\left(\frac{\partial v}{\partial t}-u\frac{\partial v}{\partial r}+\frac{v}{r}\frac{\partial v}{\partial \theta}+\frac{uv}{r}+w\frac{\partial v}{\partial z}\right)=-\frac{1}{r}\frac{\partial P}{\partial \theta}+\mu\left(\frac{\partial^2 v}{\partial r^2}+\frac{1}{r}\frac{\partial v}{\partial r}-\frac{v}{r^2}+\frac{1}{r^2}\frac{\partial^2 v}{\partial \theta^2}+\frac{2}{r^2}\frac{\partial u}{\partial \theta}+\frac{\partial^2 v}{\partial z^2}\right)+\rho g_\theta$$

z-direction momentum equation:

$$\rho\left(\frac{\partial w}{\partial t}+u\frac{\partial w}{\partial r}+\frac{v}{r}\frac{\partial w}{\partial \theta}+w\frac{\partial w}{\partial z}\right)=-\frac{\partial P}{\partial z}+\mu\left(\frac{\partial^2 w}{\partial r^2}+\frac{1}{r}\frac{\partial w}{\partial r}+\frac{1}{r^2}\frac{\partial^2 w}{\partial \theta^2}+\frac{\partial^2 w}{\partial z^2}\right)+\rho g_z$$

continuity equation:

$$\frac{\partial u}{\partial r}+\frac{u}{r}+\frac{1}{r}\frac{\partial v}{\partial \theta}+\frac{\partial w}{\partial z}=0$$

The general boundary conditions for these equations are those on the disk and on the free surface of the liquid:

z=0: u=0, w=0, v=ωr

z=h: $w=\frac{\partial h}{\partial t}+u\frac{\partial h}{\partial r}$

$p_{nr}=0, \quad p_{nn}=-p_h+\frac{\sigma}{r}\frac{\partial}{\partial r}\left(r\frac{\partial h}{\partial r}\right)$

where h is the film thickness; p_{nr}, stress tangent to the film surface; p_{nn}, normal stress; σ, surface tension;.

The following assumptions are introduced to reduce the complexity of the governing equations:

- Incompressible fluid
- $\frac{\partial}{\partial \theta}=g_r=g_\theta=0$
- Boundary layer assumptions
- No surface tension
- No interfacial shear on the free surface

- Solid body rotation, $v = \omega r$, but neglect the contribution made by the azimuthal momentum equation.

The last assumption was made as a first step to include the effect of rotation on the flow. In the future, the azimuthal momentum equation will be included in the analysis.

The governing equations and boundary conditions then reduce to the following forms:

continuity equation:

$$\frac{\partial u}{\partial r} + \frac{u}{r} + \frac{\partial w}{\partial z} = 0$$

z-direction momentum equation:

$$\frac{\partial P}{\partial z} = -\rho g$$

r-direction momentum equation:

$$\frac{\partial u}{\partial t} + u\frac{\partial u}{\partial r} + w\frac{\partial u}{\partial z} - r\omega^2 = -\frac{1}{\rho}\frac{\partial P}{\partial r} + \nu\frac{\partial^2 u}{\partial z^2}$$

Boundary conditions:

$P(r,h,t) = 0$

$u(r_1,z,t) = u_1$

$u(r,z,0) = u_0$

$\left(\frac{\partial u}{\partial z}\right)\Big|_{z=h} = 0$

$w(r,0,t) = 0$

Integrating the conservation equations across the thin layer results in quasi - one-dimensional governing equations:

Continuity equation:

$$\frac{\partial u}{\partial r} + \frac{u}{r} + \frac{\partial w}{\partial z} = 0$$

$$\int_0^h \left(\frac{\partial u}{\partial r}\right) dz + \int_0^h \left(\frac{u}{r}\right) dz + \int_0^h \left(\frac{\partial w}{\partial z}\right) dz = 0$$

Leibniz's rule:

$$\frac{d}{dx}\int_A^B f(x,t)dt = \int_A^B \frac{\partial f(x,t)}{\partial x} dt + f(x,B)\cdot\frac{dB}{dx} - f(x,A)\cdot\frac{dA}{dx}$$

$$\int_0^h \left(\frac{\partial u}{\partial r}\right) dz = \frac{\partial}{\partial r}\int_0^h u\, dz - u|_h \cdot \frac{\partial h}{\partial r}$$

The kinematic condition at the free surface for unsteady problems is used as one of the free surface boundary conditions:

$$\frac{\partial h}{\partial t} + u|_h \cdot \frac{\partial h}{\partial r} = w|_h$$

$$-u|_h \cdot \frac{\partial h}{\partial r} = \frac{\partial h}{\partial t} - w|_h$$

$$\int_0^h \left(\frac{\partial u}{\partial r}\right) dz = \frac{\partial}{\partial r}\int_0^h u\, dz + \frac{\partial h}{\partial t} - w|_h$$

$$\bar{u} = \frac{1}{h}\int_0^h u\, dz$$

$$\int_0^h \left(\frac{\partial u}{\partial r}\right) dz = \frac{\partial}{\partial r}(\bar{u}h) + \frac{\partial h}{\partial t} - w|_h$$

$$\int_0^h \left(\frac{u}{r}\right) dz = \frac{1}{r}\int_0^h u\, dz = \frac{\bar{u}h}{r}$$

$$\int_0^h \left(\frac{\partial w}{\partial z}\right) dz = w|_h - w|_0$$

$$\frac{\partial}{\partial r}(\bar{u}h) + \frac{\partial h}{\partial t} - w|_h + \frac{\bar{u}h}{r} + w|_h - w|_0 = 0$$

$$\frac{\partial}{\partial r}(\bar{u}h) + \frac{\bar{u}h}{r} + \frac{\partial h}{\partial t} = 0$$

$$\frac{1}{r}\frac{\partial(r\bar{u}h)}{\partial r} + \frac{\partial h}{\partial t} = 0 \tag{3.1}$$

z-direction momentum equation:

$$\frac{\partial P}{\partial z} = -\rho g$$

$$\int_0^h \left(\frac{\partial P}{\partial z}\right) dz = -\rho g \int_0^h dz$$

$$P = -\rho g z + C$$

$$P = \rho g(h - z) \tag{3.2}$$

r-direction momentum equation:

$$\frac{\partial u}{\partial t} + u\frac{\partial u}{\partial r} + w\frac{\partial u}{\partial z} - r\omega^2 = -\frac{1}{\rho}\frac{\partial P}{\partial r} + \nu\frac{\partial^2 u}{\partial z^2}$$

$$\int_0^h \left(\frac{\partial u}{\partial t}\right) dz + \int_0^h \left(u\frac{\partial u}{\partial r}\right) dz + \int_0^h \left(w\frac{\partial u}{\partial z}\right) dz - \int_0^h (r\omega^2) dz = -\frac{1}{\rho}\int_0^h \left(\frac{\partial P}{\partial r}\right) dz + \nu \int_0^h \left(\frac{\partial^2 u}{\partial z^2}\right) dz$$

$$\int_0^h \left(\frac{\partial u}{\partial t}\right) dz = \frac{\partial}{\partial t}\int_0^h u\, dz - u|_h \cdot \frac{\partial h}{\partial t}$$
$$= \frac{\partial}{\partial t}(\bar{u}h) - u|_h \cdot \frac{\partial h}{\partial t}$$

$$\int_0^h \left(w\frac{\partial u}{\partial z}\right) dz = \int_0^h \frac{\partial (uw)}{\partial z} dz - \int_0^h \left(u\frac{\partial w}{\partial z}\right) dz$$
$$= (uw)|_h - (uw)|_0 - \int_0^h \left(u\frac{\partial w}{\partial z}\right) dz$$
$$= (uw)|_h - \int_0^h \left(u\frac{\partial w}{\partial z}\right) dz$$

$$\int_0^h \left(\frac{\partial P}{\partial r}\right) dz = \frac{\partial}{\partial r}\int_0^h P\, dz - P|_h \cdot \frac{\partial h}{\partial r}$$
$$= \frac{\partial}{\partial r}\int_0^h \rho g(h-z) dz$$
$$= \frac{\partial}{\partial r}\left(\frac{1}{2}\rho g h^2\right)$$

$$\int_0^h \left(\frac{\partial^2 u}{\partial z^2}\right) dz = \int_0^h \frac{\partial}{\partial z}\left(\frac{\partial u}{\partial z}\right) dz$$
$$= \int_0^h d\left(\frac{\partial u}{\partial z}\right)$$
$$= \left(\frac{\partial u}{\partial z}\right)\Big|_h - \left(\frac{\partial u}{\partial z}\right)\Big|_0$$
$$= -\left(\frac{\partial u}{\partial z}\right)\Big|_0$$

$$\frac{\partial}{\partial t}(\bar{u}h) - u|_h \cdot \frac{\partial h}{\partial t} + \int_0^h \left(u\frac{\partial u}{\partial r}\right) dz + (uw)|_h - \int_0^h \left(u\frac{\partial w}{\partial z}\right) dz - rh\omega^2 = -\frac{\partial}{\partial r}\left(\frac{1}{2}gh^2\right) - \nu\left(\frac{\partial u}{\partial z}\right)\Big|_0$$

From the continuity equation:

$$-\int_0^h \left(u\frac{\partial w}{\partial z}\right) dz = \int_0^h \left(u\frac{\partial u}{\partial r}\right) dz + \int_0^h \left(\frac{u^2}{r}\right) dz$$

Using the kinematic condition at the free surface:

$$(uw)|_h = u|_h\left(\frac{\partial h}{\partial t} + u|_h \cdot \frac{\partial h}{\partial r}\right)$$
$$= u|_h \cdot \frac{\partial h}{\partial t} + (u|_h)^2 \cdot \frac{\partial h}{\partial r}$$

$$\frac{\partial}{\partial t}(\bar{u}h) - u|_h \cdot \frac{\partial h}{\partial t} + \int_0^h \left(u\frac{\partial u}{\partial r}\right)dz + u|_h \cdot \frac{\partial h}{\partial t} + (u|_h)^2 \cdot \frac{\partial h}{\partial r} + \int_0^h \left(u\frac{\partial u}{\partial r}\right)dz + \int_0^h \left(\frac{u^2}{r}\right)dz - rh\omega^2$$

$$= -\frac{\partial}{\partial r}\left(\frac{1}{2}gh^2\right) - \nu\left(\frac{\partial u}{\partial z}\right)\Big|_0$$

$$\frac{\partial}{\partial t}(\bar{u}h) + 2\int_0^h \left(u\frac{\partial u}{\partial r}\right)dz + (u|_h)^2 \cdot \frac{\partial h}{\partial r} + \int_0^h \left(\frac{u^2}{r}\right)dz - rh\omega^2 = -\frac{\partial}{\partial r}\left(\frac{1}{2}gh^2\right) - \nu\left(\frac{\partial u}{\partial z}\right)\Big|_0$$

$$\frac{\partial}{\partial t}(\bar{u}h) + \int_0^h \left(2u\frac{\partial u}{\partial r} + \frac{u^2}{r}\right)dz + (u|_h)^2 \cdot \frac{\partial h}{\partial r} - rh\omega^2 = -\frac{\partial}{\partial r}\left(\frac{1}{2}gh^2\right) - \nu\left(\frac{\partial u}{\partial z}\right)\Big|_0$$

$$2u\frac{\partial u}{\partial r} + \frac{u^2}{r} = \frac{1}{r} \cdot \frac{\partial (ru^2)}{\partial r}$$

$$\frac{\partial}{\partial t}(\bar{u}h) + \frac{1}{r}\int_0^h \frac{\partial (ru^2)}{\partial r}dz + (u|_h)^2 \cdot \frac{\partial h}{\partial r} - rh\omega^2 = -\frac{\partial}{\partial r}\left(\frac{1}{2}gh^2\right) - \nu\left(\frac{\partial u}{\partial z}\right)\Big|_0$$

$$\int_0^h \frac{\partial (ru^2)}{\partial r}dz = \frac{\partial}{\partial r}\int_0^h ru^2\, dz - (ru^2)|_h \cdot \frac{\partial h}{\partial r}$$

$$\frac{\partial}{\partial t}(\bar{u}h) + \frac{1}{r}\left(\frac{\partial}{\partial r}\int_0^h ru^2\, dz - (ru^2)|_h \cdot \frac{\partial h}{\partial r}\right) + (u|_h)^2 \cdot \frac{\partial h}{\partial r} - rh\omega^2 = -\frac{\partial}{\partial r}\left(\frac{1}{2}gh^2\right) - \nu\left(\frac{\partial u}{\partial z}\right)\Big|_0$$

$$\frac{\partial}{\partial t}(\bar{u}h) + \frac{1}{r}\frac{\partial}{\partial r}\left(r\int_0^h u^2\, dz\right) - (u|_h)^2 \cdot \frac{\partial h}{\partial r} + (u|_h)^2 \cdot \frac{\partial h}{\partial r} - rh\omega^2 = -\frac{\partial}{\partial r}\left(\frac{1}{2}gh^2\right) - \nu\left(\frac{\partial u}{\partial z}\right)\Big|_0$$

$$\frac{\partial}{\partial t}(\bar{u}h) + \frac{1}{r}\frac{\partial}{\partial r}\left(r\int_0^h u^2\, dz\right) - rh\omega^2 = -\frac{\partial}{\partial r}\left(\frac{1}{2}gh^2\right) - \nu\left(\frac{\partial u}{\partial z}\right)\Big|_0$$

Assumption:

$$\int_0^h u^2\, dz \simeq \bar{u}^2 h$$

$$\frac{\partial}{\partial t}(\bar{u}h) + \frac{1}{r}\frac{\partial}{\partial r}(r\bar{u}^2 h) - rh\omega^2 = -\frac{\partial}{\partial r}\left(\frac{1}{2}gh^2\right) - \nu\left(\frac{\partial u}{\partial z}\right)\Big|_0$$

$$\begin{aligned}\frac{1}{r}\frac{\partial}{\partial r}(r\bar{u}^2 h) &= \frac{1}{r}\left[r\frac{\partial}{\partial r}(\bar{u}^2 h) + \bar{u}^2 h\right] \\ &= \frac{\partial}{\partial r}(\bar{u}^2 h) + \frac{\bar{u}^2 h}{r}\end{aligned}$$

$$\frac{\partial}{\partial t}(\bar{u}h) + \frac{\partial}{\partial r}(\bar{u}^2 h) + \frac{\partial}{\partial r}\left(\frac{1}{2}gh^2\right) + \frac{\bar{u}^2 h}{r} - rh\omega^2 = -\nu\left(\frac{\partial u}{\partial z}\right)\Big|_0$$

$$\frac{\partial}{\partial t}(\bar{u}h) + \frac{\partial}{\partial r}\left(\bar{u}^2 h + \frac{1}{2}gh^2\right) = h\left(r\omega^2 - \frac{\bar{u}^2}{r}\right) - \nu\left(\frac{\partial u}{\partial z}\right)\Big|_0$$

Assumption:

$$u_\infty = \bar{u}$$

$$\nu\left(\frac{\partial u}{\partial z}\right)\Big|_0 \simeq \frac{0.332\bar{u}^2}{\sqrt{\bar{u}r/\nu}}$$

$$\frac{\partial}{\partial t}(\bar{u}h) + \frac{\partial}{\partial r}\left(\bar{u}^2 h + \frac{1}{2}gh^2\right) = h\left(r\omega^2 - \frac{\bar{u}^2}{r}\right) - \frac{0.332\bar{u}^2}{\sqrt{\bar{u}r/\nu}}$$

Assumption:

$$\frac{\partial h}{\partial t} \simeq 0$$

$$\frac{\partial}{\partial t}(\bar{u}h) = \bar{u}\frac{\partial h}{\partial t} + h\frac{\partial \bar{u}}{\partial t} = h\frac{\partial \bar{u}}{\partial t}$$

r-direction momentum equation:

$$h\frac{\partial \bar{u}}{\partial t} + \frac{\partial}{\partial r}\left(\bar{u}^2 h + \frac{1}{2}gh^2\right) = h\left(r\omega^2 - \frac{\bar{u}^2}{r}\right) - \frac{0.332\bar{u}^2}{\sqrt{\bar{u}r/\nu}} \tag{3.3}$$

Continuity equation:

$$\frac{1}{r}\frac{\partial}{\partial r}(r\bar{u}h) = 0$$

$$r\bar{u}h = \text{ constant } = \text{ Q} \tag{3.4}$$

Dimensionless variables:

$$\frac{\bar{u}}{\bar{u}_1} = V \qquad \frac{h}{h_1} = \delta \qquad \frac{r}{h_1} = \xi \qquad t\frac{\bar{u}_1}{h_1} = \tau \qquad \omega\frac{h_1}{\bar{u}_1} = \Omega$$

$$\frac{\bar{u}_1 h_1}{\nu} = Re_1 \qquad \frac{\bar{u}_1^2}{gh_1} = Fr_1^2$$

$$\bar{u} = \bar{u}_1 V \qquad h = h_1\delta \qquad r = h_1\xi \qquad t = \frac{h_1}{\bar{u}_1}\tau \qquad \omega = \frac{\bar{u}_1}{h_1}\Omega$$

Radial momentum equation:

$$h\frac{\partial \bar{u}}{\partial t} + \frac{\partial}{\partial r}\left(\bar{u}^2 h + \frac{1}{2}gh^2\right) = h\left(r\omega^2 - \frac{\bar{u}^2}{r}\right) - \frac{0.332\bar{u}^2}{\sqrt{\bar{u}r/\nu}}$$

$$(h_1\delta)\frac{\partial(\bar{u}_1 V)}{\partial(h_1\tau/\bar{u}_1)} + \frac{\partial}{\partial(h_1\xi)}\left[(\bar{u}_1 V)^2(h_1\delta) + \frac{1}{2}g(h_1\delta)^2\right]$$

$$= (h_1\delta)\left[(h_1\xi)\left(\frac{\bar{u}_1}{h_1}\Omega\right)^2 - \frac{(\bar{u}_1 V)^2}{(h_1\xi)}\right] - 0.332(\bar{u}_1 V)^2\Big/\sqrt{\frac{(\bar{u}_1 V)(h_1\xi)}{\nu}}$$

$$(\bar{u}_1^2)\delta\frac{\partial V}{\partial \tau}+(\bar{u}_1^2)\frac{\partial}{\partial \xi}\left[V^2\delta+\frac{1}{2}\frac{gh_1}{\bar{u}_1^2}\delta^2\right]\doteq(\bar{u}_1^2)\delta\left[\xi\Omega^2-\frac{V^2}{\xi}\right]-(\bar{u}_1^2)0.332V^2\Big/\sqrt{Re_1V\xi}$$

$$\delta\frac{\partial V}{\partial \tau}+\frac{\partial}{\partial \xi}\left[V^2\delta+\frac{1}{2Fr_1^2}\delta^2\right]=\delta\left[\xi\Omega^2-\frac{V^2}{\xi}\right]-0.332V^{3/2}\Big/\sqrt{Re_1\xi}$$

Continuity equation:

$$r\bar{u}h=Q$$

$$(h_1\xi)(\bar{u}_1V)(h_1\delta)=Q$$

$$\xi V\delta=\frac{Q}{\bar{u}_1h_1^2}=\xi_1$$

Divide both sides by δ and eliminate it from the radial momentum equation with the continuity equation:

$$\frac{\partial V}{\partial \tau}+\frac{1}{\delta}\frac{\partial}{\partial \xi}\left[V^2\delta+\frac{1}{2Fr_1^2}\delta^2\right]=\xi\Omega^2-\frac{V^2}{\xi}-\frac{0.332V^{3/2}}{\delta\sqrt{Re_1\xi}}$$

$$\delta=\frac{\xi_1}{V\xi}$$

$$\frac{\partial V}{\partial \tau}+\frac{V\xi}{\xi_1}\frac{\partial}{\partial \xi}\left[V^2\left(\frac{\xi_1}{V\xi}\right)+\frac{1}{2Fr_1^2}\left(\frac{\xi_1}{V\xi}\right)^2\right]=\xi\Omega^2-\frac{V^2}{\xi}-\left(\frac{V\xi}{\xi_1}\right)\frac{0.332V^{3/2}}{\sqrt{Re_1\xi}}$$

$$\frac{\partial V}{\partial \tau}+V\xi\frac{\partial}{\partial \xi}\left[\frac{V}{\xi}+\frac{\xi_1}{2Fr_1^2}\left(\frac{1}{V\xi}\right)^2\right]=\xi\Omega^2-\frac{V^2}{\xi}-\frac{0.332V^{5/2}}{\xi_1}\sqrt{\frac{\xi}{Re_1}}$$

Dimensionless governing equation:

$$V_\tau + V\xi G_\xi = H \tag{3.5}$$

where

$$G = \frac{V}{\xi} + \frac{\xi_1}{2Fr_1^2}\left(\frac{1}{V\xi}\right)^2 \tag{3.6}$$

$$H = \xi\Omega^2 - \frac{V^2}{\xi} - \frac{0.332V^{5/2}}{\xi_1}\sqrt{\frac{\xi}{Re_1}} \tag{3.7}$$

For the case when gravity is zero, the equation for G is as follows:

$$G = \frac{V}{\xi}$$

The governing equation has one time derivative and one space derivative, so an initial condition and a boundary value are needed.

Initial condition:

$\tau = 0$: $V = V_0 = 1.0$ for $\xi_1 \leq \xi \leq \xi_n$

Boundary condition:

$\xi = \xi_1$: $Fr = Fr_1, \quad V = 1$

3.3. Numerical solution procedure

The MacCormack explicit method is quite often used for the solution of compressible flow problems. Since it is an explicit method, the unknown variables are found in terms of known quantities, as opposed to implicit methods which must solve a matrix equation to obtain the solution of the problem.

The MacCormack method is a two-step scheme that uses first-order finite-difference approximations. The scheme first predicts the solution at the next time step with a forward time, forward space (FTFS) differencing scheme and then corrects the prediction with a

forward time, backward space (FTBS) scheme. This results in a approximation that is second-order accurate in both time and space (Hankey, 1982).

When applied to the one-dimensional linear convection equation,

$$\frac{\partial u}{\partial t} + c\frac{\partial u}{\partial x} = 0$$

the MacCormack method yields (Anderson et al., 1984)

$$\overline{u_j^{n+1}} = u_j^n - c\frac{\Delta t}{\Delta x}(u_{j+1}^n - u_j^n) \qquad \text{Forward predictor}$$

$$u_j^{n+1} = \frac{1}{2}\left[u_j^n + \overline{u_j^{n+1}} - c\frac{\Delta t}{\Delta x}(\overline{u_j^{n+1}} - \overline{u_{j-1}^{n+1}})\right] \qquad \text{Backward corrector}$$

The corrector can be seen as an arithmetic average of the old solution, u_j^n, and the new solution based on the predicted solution, $\overline{u_j^{n+1}} - c\frac{\Delta t}{\Delta x}(\overline{u_j^{n+1}} - \overline{u_{j-1}^{n+1}})$, which uses a backward difference.

The governing equation for the present problem is as follows:

$$V_\tau + V\xi G_\xi = H$$

where

$$G = \frac{V}{\xi} + \frac{\xi_1}{2Fr_1^2}\left(\frac{1}{V\xi}\right)^2$$

$$H = \xi\Omega^2 - \frac{V^2}{\xi} - \frac{0.332V^{5/2}}{\xi_1}\sqrt{\frac{\xi}{Re_1}}$$

Forward predictor: FTFS

$$\frac{\overline{V_j^{n+1}} - V_j^n}{\Delta\tau} + V_j^n\xi_j\left[\frac{G_{j+1}^n - G_j^n}{\Delta\xi}\right] = H_j^n$$

$$\overline{V_j^{n+1}} = V_j^n - V_j^n \xi_j \frac{\Delta\tau}{\Delta\xi}(G_{j+1}^n - G_j^n) + \Delta\tau H_j^n$$

$$\overline{V_j^{n+1}} = V_j^n \left[1 - \xi_j \frac{\Delta\tau}{\Delta\xi}(G_{j+1}^n - G_j^n)\right] + \Delta\tau H_j^n \tag{3.8}$$

Backward corrector: FTBS

The finite-difference equation based on the predicted solution using a forward time, backward space differencing scheme is as follows

$$\frac{(\overline{V_j^{n+1}})' - \overline{V_j^{n+1}}}{\Delta\tau} + \overline{V_j^{n+1}} \xi_j \left[\frac{\overline{G_j^{n+1}} - \overline{G_{j-1}^{n+1}}}{\Delta\xi}\right] = \overline{H_j^{n+1}}$$

$$(\overline{V_j^{n+1}})' = \overline{V_j^{n+1}} - \overline{V_j^{n+1}} \xi_j \frac{\Delta\tau}{\Delta\xi}\left(\overline{G_j^{n+1}} - \overline{G_{j-1}^{n+1}}\right) + \Delta\tau \overline{H_j^{n+1}}$$

$$(\overline{V_j^{n+1}})' = \overline{V_j^{n+1}}\left[1 - \xi_j \frac{\Delta\tau}{\Delta\xi}\left(\overline{G_j^{n+1}} - \overline{G_{j-1}^{n+1}}\right)\right] + \Delta\tau \overline{H_j^{n+1}}$$

The corrected solution is the arithmetic average of the past and predicted solutions

$$V_j^{n+1} = \frac{1}{2}[V_j^n + (\overline{V_j^{n+1}})']$$

$$V_j^{n+1} = \frac{1}{2}\left\{V_j^n + \overline{V_j^{n+1}}\left[1 - \xi_j \frac{\Delta\tau}{\Delta\xi}\left(\overline{G_j^{n+1}} - \overline{G_{j-1}^{n+1}}\right)\right] + \Delta\tau \overline{H_j^{n+1}}\right\} \tag{3.9}$$

where

$$G_j^n = \frac{V_j^n}{\xi_j} + \frac{\xi_1}{2F\tau_1^2}\left(\frac{1}{V_j^n \xi_j}\right)^2 \tag{3.10}$$

$$H_j^n = \xi_j \Omega^2 - \frac{(V_j^n)^2}{\xi_j} - \frac{0.332(V_j^n)^{5/2}}{\xi_1}\sqrt{\frac{\xi_j}{Re_1}} \tag{3.11}$$

$$G_j^{\overline{n+1}} = \frac{V_j^{\overline{n+1}}}{\xi_j} + \frac{\xi_1}{2Fr_1^2}\left(\frac{1}{V_j^{\overline{n+1}}\xi_j}\right)^2 \tag{3.12}$$

$$H_j^{\overline{n+1}} = \xi_j\Omega^2 - \frac{(V_j^{\overline{n+1}})^2}{\xi_j} - \frac{0.332(V_j^{\overline{n+1}})^{5/2}}{\xi_1}\sqrt{\frac{\xi_j}{Re_1}} \tag{3.13}$$

Since the forward predictor velocity is in terms of a forward-space approximation, an outlet boundary condition on the velocity is needed. For the case of 1-g, it is assumed that the Froude number at the outlet is unity, which is a common boundary condition when a liquid falls over an edge. The Froude number and the dimensionless velocity are related as follows:

$$Fr_1^2 = \frac{\bar{u}_1^2}{gh_1} \qquad Fr^2 = \frac{\bar{u}^2}{gh}$$

$$\frac{Fr^2}{Fr_1^2} = \frac{(\bar{u}_1 V)^2}{g(h_1\delta)} \cdot \frac{gh_1}{\bar{u}_1^2} = \frac{V^2}{\delta} = V^2\left(\frac{V\xi}{\xi_1}\right) = \frac{\xi}{\xi_1}V^3$$

$$V = \left(\frac{\xi_1}{\xi} \cdot \frac{Fr^2}{Fr_1^2}\right)^{1/3}$$

$$V_n = \left(\frac{\xi_1}{\xi_n} \cdot \frac{Fr_n^2}{Fr_1^2}\right)^{1/3} = \left(\frac{\xi_1}{\xi_n} \cdot \frac{1}{Fr_1^2}\right)^{1/3}$$

For the microgravity case, the slope at the last node is set equal to the slope at the next to last node since the outlet boundary condition can not be specified by the Froude number.

The solution of the governing equation using the MacCormack explicit method proceeds as follows:

- The parameters pertaining to the numerical domain and the inlet and outlet boundary conditions are specified.
- The initial velocity distribution is input to the program.

- The variables G and H are computed using the velocity profile at the old time step as given in eqs. (3.10, 3.11).
- The velocity distribution at the midpoint time step is calculated in terms of the velocity, G, and H at the old time step as shown in eq. (3.8). An outlet boundary condition is needed at this step because of the forward-space approximation.
- The variables G and H are computed again by using the velocity profile at the midpoint time step as presented in eqs. (3.12, 3.13).
- The velocity distribution at the new time step is calculated using eq. (3.9). The inlet boundary condition is used in this step because of the backward-space approximation.
- The values of the velocity distribution at the new time step are used as the initial velocity profile for the next iteration.
- The process is repeated until steady values are reached.

PSEUDO-CODE FOR RADIAL FLOW

---

* Input parameters *

Fr_1, Re_1, ξ_1, ξ_n, $\Delta\tau$, $\Delta\xi$, Ω

---

* Input initial velocity distribution at the old time step *

$VOLD(I) = 1$

---

* Compute G and H at the old time step *

10 $GOLD(I) = GOLD(VOLD(I),\ Fr_1)$

$HOLD(I) = HOLD(VOLD(I),\ Re_1,\ \xi(I))$

---

* Compute V at the mid time step *

$VMID(I) = VMID(VOLD(I),\ \Delta\tau,\ \Delta\xi,\ GOLD(I+1),\ HOLD(I))$

---

* Compute G and H at the mid time step *

$GMID(I) = GMID(VMID(I),\ Fr_1)$

$HMID(I) = HMID(VMID(I),\ Re_1,\ \xi(I))$

---

* Compute V at the new time step *

$VNEW(I) = VNEW(VOLD(I),\ VMID(I),\ GMID(I),\ GMID(I-1),\ HMID(I))$

---

* Test for convergence *

---

* Let V at the new time step be V at the old time step *

VOLD(I) = VNEW(I)

GOTO 10

---

* Print results *

3.4 Results

The results of the computer program that predicts the height of liquid in radial flow with a free surface on a disk under 1-g are shown in Figures 3.2 - 3.6. These figures show the dimensionless liquid film height under 1-g with no rotation as the initial Froude number changes from $Fr_1 = 2.0$ - 6.0 and the initial Reynolds number changes from $Re_1 = 25.36$ - 76.06. The outlet boundary condition for these cases is $Fr_n = 1.0$, which corresponds to a liquid falling over an edge. For small initial Froude numbers ($Fr_1 \rightarrow 1$), a radial hydraulic jump is predicted very close to the inner radius of the disk. A hydraulic jump is when the liquid film height suddenly increases when the flow changes from supercritical ($Fr > 1$) to subcritical flow ($Fr < 1$). As the initial Froude number increases, the radius of the hydraulic jump increases, which agrees with experimental data. For all of the cases in this set of figures, the liquid film height first decreases and then increases in the supercritical region. As will be shown in other cases, this is not always true if the inlet Reynolds number is sufficiently small.

Figures 3.7 - 3.11 give the results of when the gravity term is set to zero, which corresponds to a microgravity simulation. The inlet condition was specified with the inlet Reynolds number which ranged from $Re_1 = 25.36$ - 76.06. The outlet boundary condition was specified by forcing the slope of the curve at the outlet be equal to the slope just before the outlet. In all of the cases studied, a hydraulic jump did not appear. The trend in all of the cases in these figures was an initial decrease in the liquid height followed by a monotonic increase of the liquid film height. It can be seen that as the initial Reynolds number increases, the liquid film height decreases at all points along the radius.

Figures 3.12 - 3.14 demonstrate the effect of solid-body rotation on the liquid film height. Figure 3.12 shows the flow field without rotation, Fig. 3.13 presents the liquid height with the dimensionless angular velocity set to $\Omega = 10^{-3}$, and the Fig. 3.14 shows the film height with $\Omega = 10^{-2}$. With $\Omega = 10^{-3}$, the shape of the hydraulic jump has been 'stretched' along the radial axis, while with $\Omega = 10^{-2}$ the hydraulic jump has been completely 'washed out.'

Figure 3.15 shows the results of the program when there is gravity, no rotation, and the outlet boundary condition is specified such that the slope at the outlet is equal to the slope just before the outlet. It can be seen that the solution does not converge even when the time step is decreased to 0.1 of the time step with the outlet boundary condition specified.

Figure 3.16 compares the results of the channel flow with that of the radial flow with the same inlet and outlet conditions. The height of the liquid film for channel flow is approximately twice that of radial flow.

Figures 3.17 - 3.19 compare the results of the computer program under 1-g when the friction at the wall is increased by a factor of three. The graphs show that the effect of increasing the friction is the same as in channel flow: the height of the liquid film is increased, and the location of the hydraulic jump is closer to the inlet of the computational domain.

Fig. 3.1 The coordinate system for radial flow

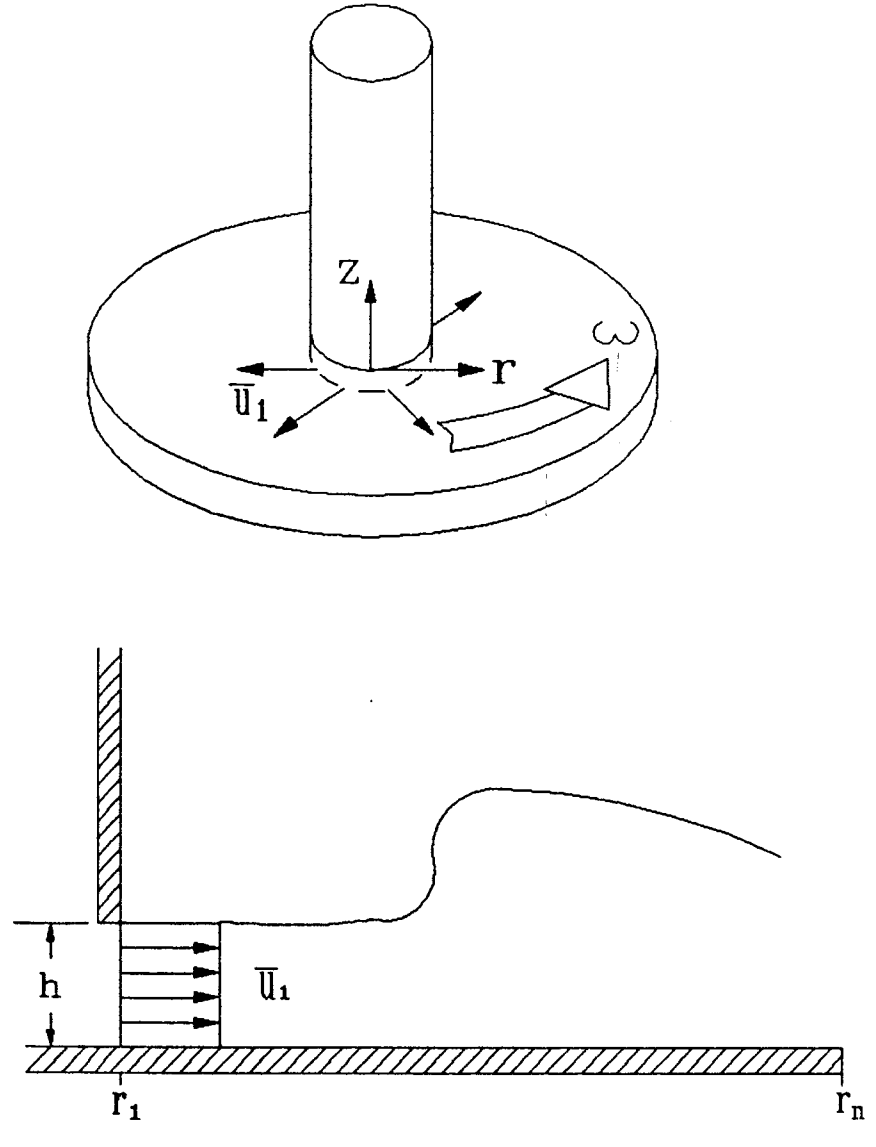

Fig. 3.2 Radial flow – $Fr_1 = 2.0$, $Fr_n = 1.0$, $Re_1 = 25.36$, $\xi_1 = 200.0$, $\xi_n = 768.9$, $\Omega = 0.0$

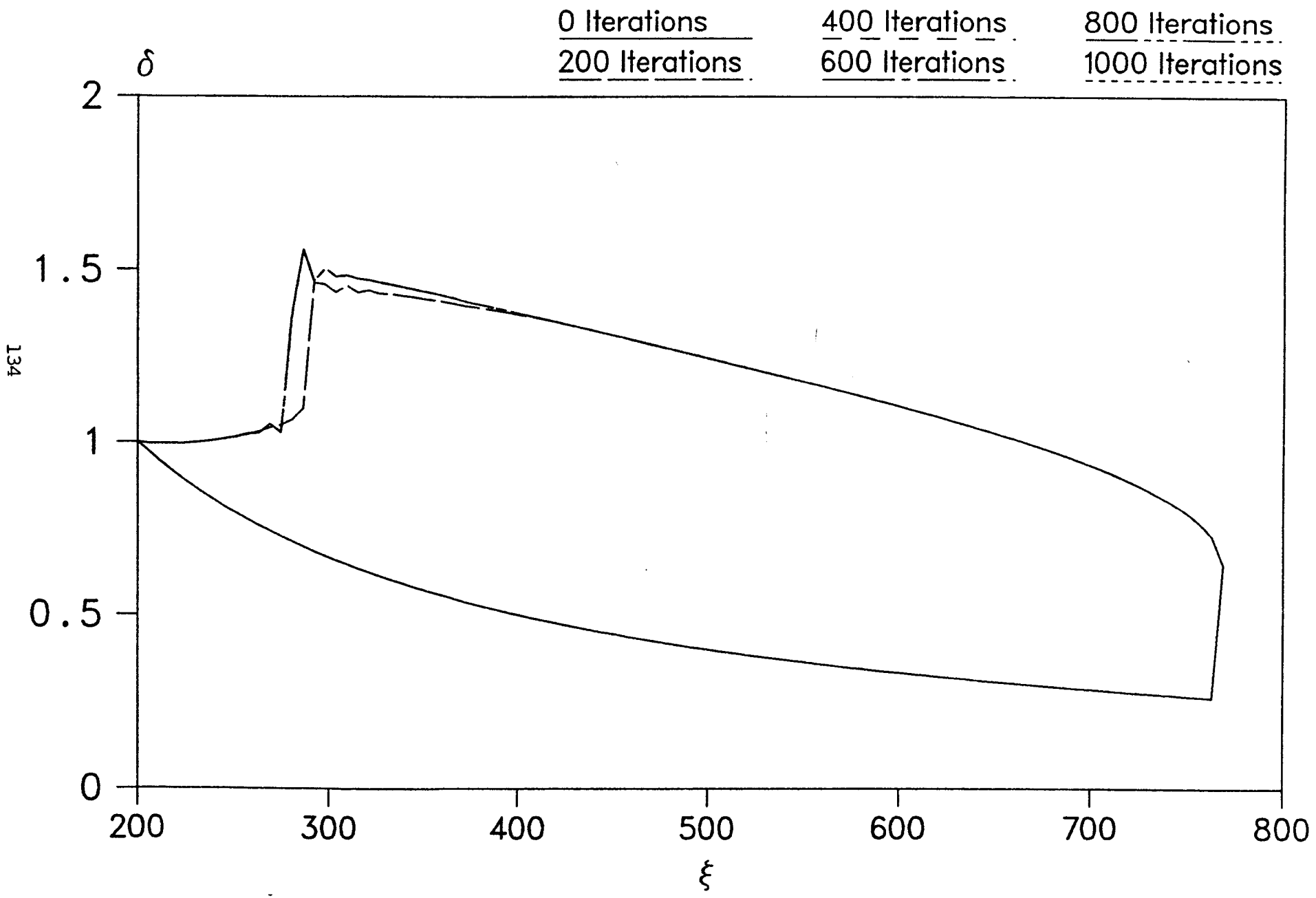

Radial flow – $Fr_1 = 3.0$, $Fr_n = 1.0$, $Re_1 = 38.04$, $\xi_1 = 200.0$, $\xi_n = 768.9$, $\Omega = 0.0$

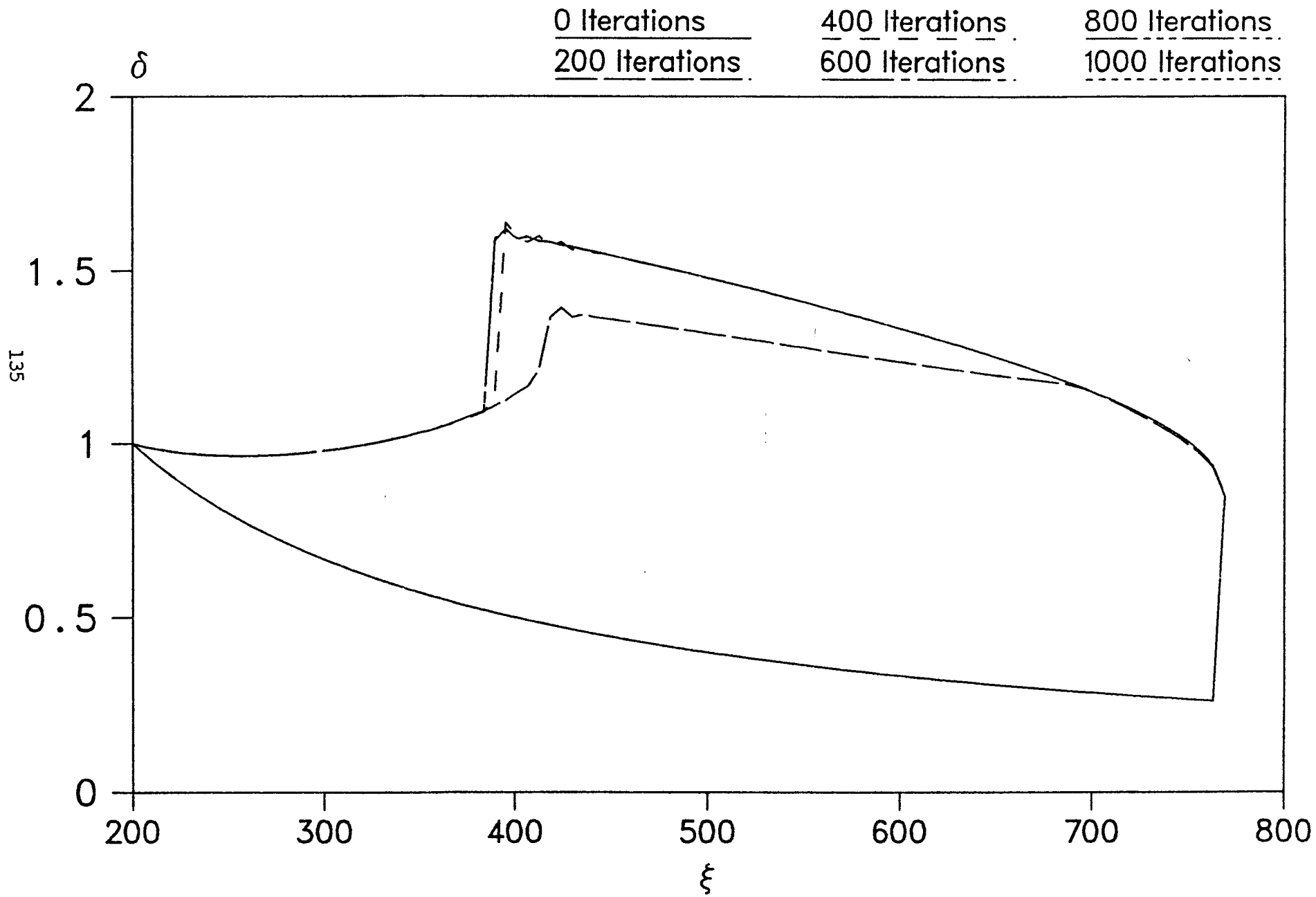

Radial flow — $Fr_1 = 4.0$, $Fr_n = 1.0$, $Re_1 = 50.71$, $\xi_1 = 200.0$, $\xi_n = 768.9$, $\Omega = 0.0$

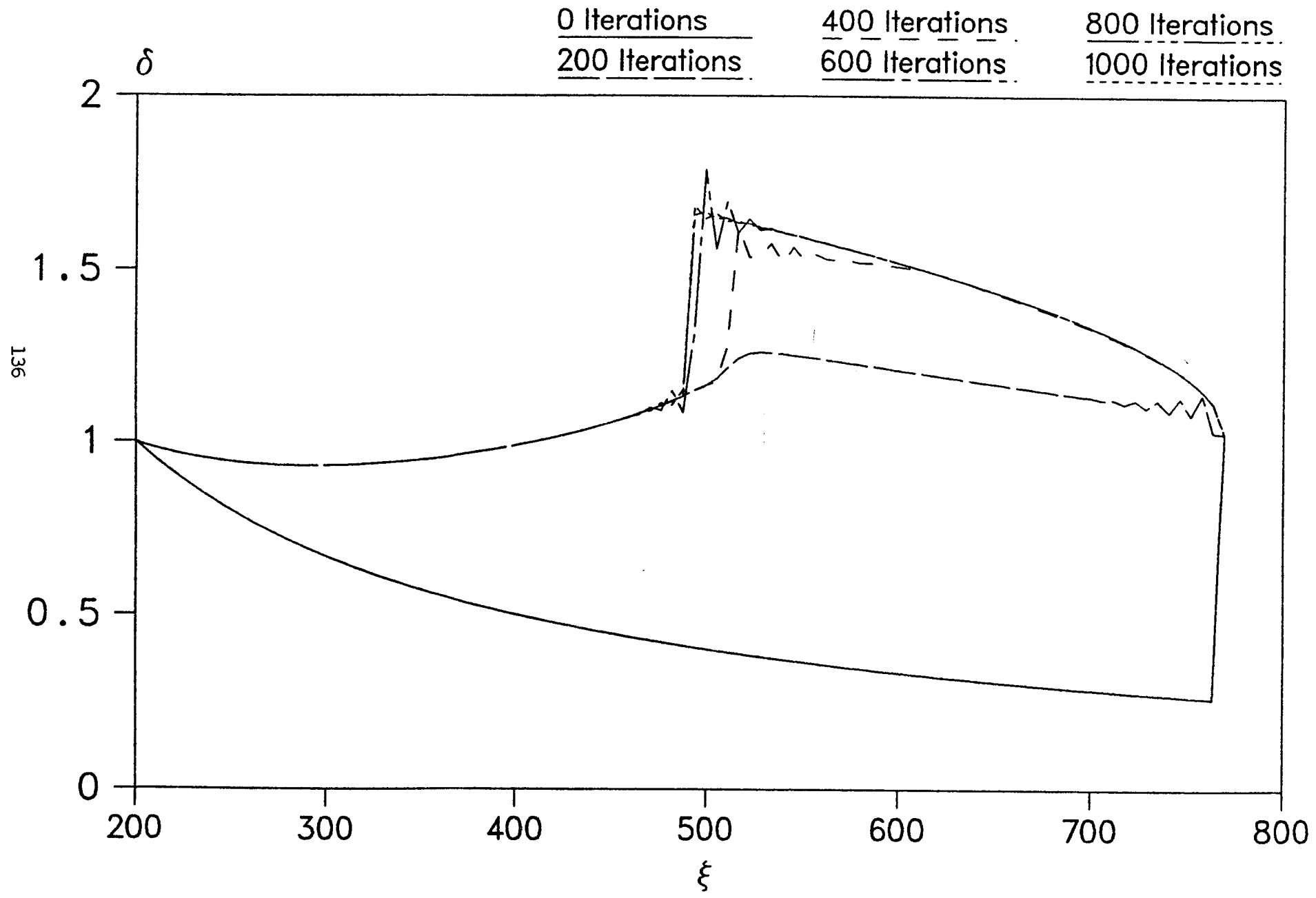

Radial flow – $Fr_1 = 5.0$, $Fr_n = 1.0$, $Re_1 = 63.41$, $\xi_1 = 200.0$, $\xi_n = 768.9$, $\Omega = 0.0$

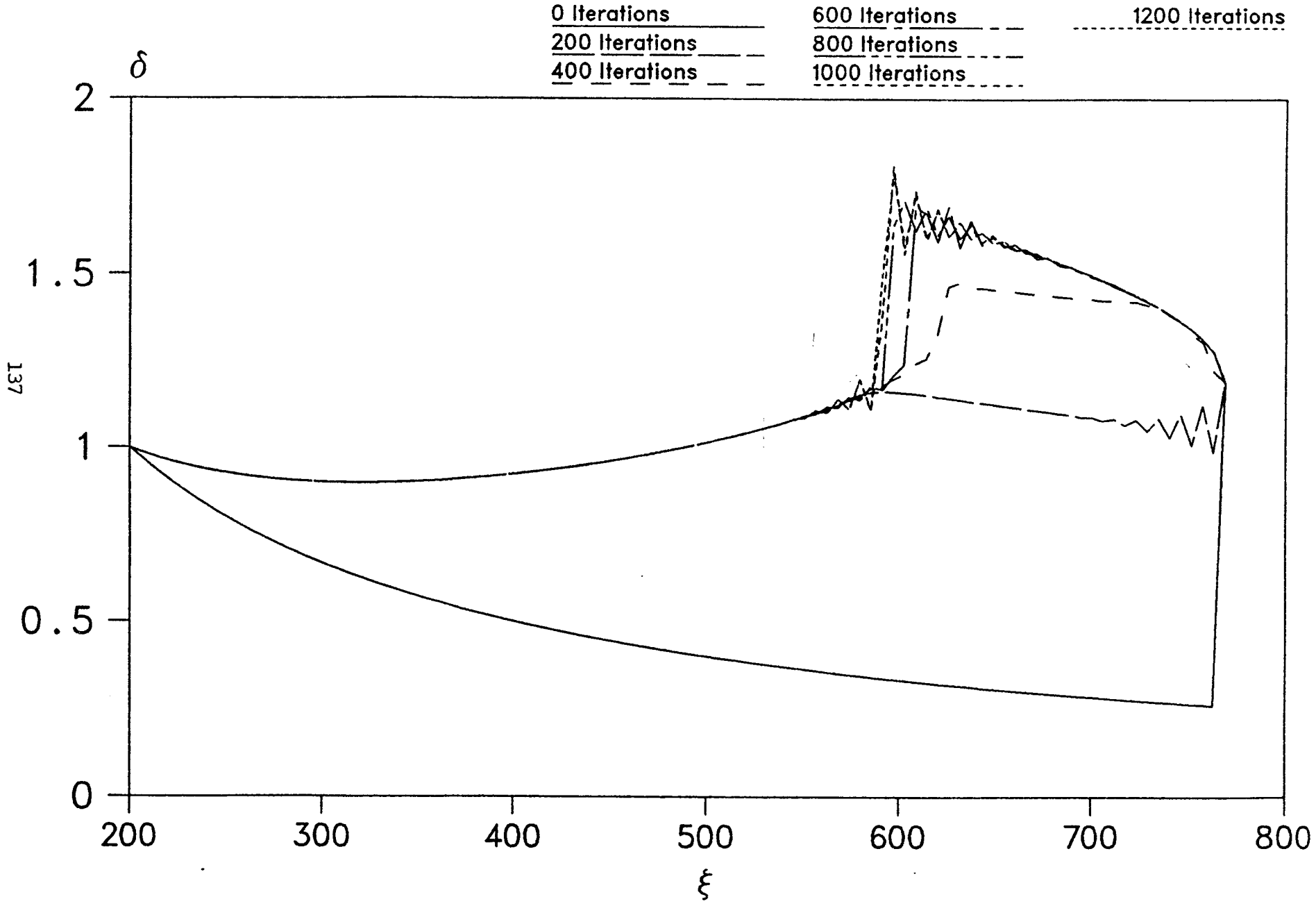

Fig. 3.6 Radial flow — $Fr_1 = 6.0$, $Fr_n = 1.0$, $Re_1 = 76.06$, $\xi_1 = 200.0$, $\xi_n = 768.9$, $\Omega = 0.0$

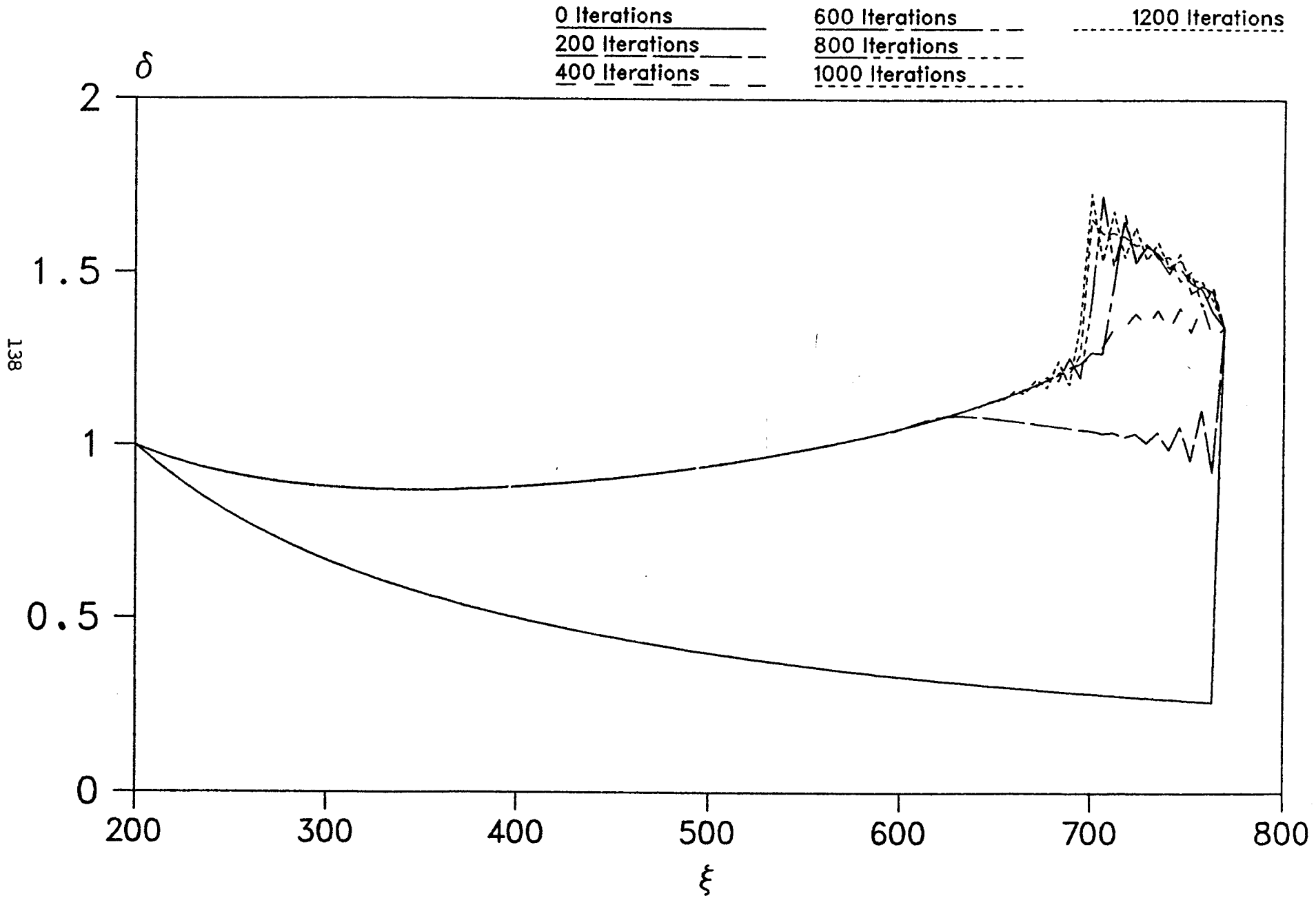

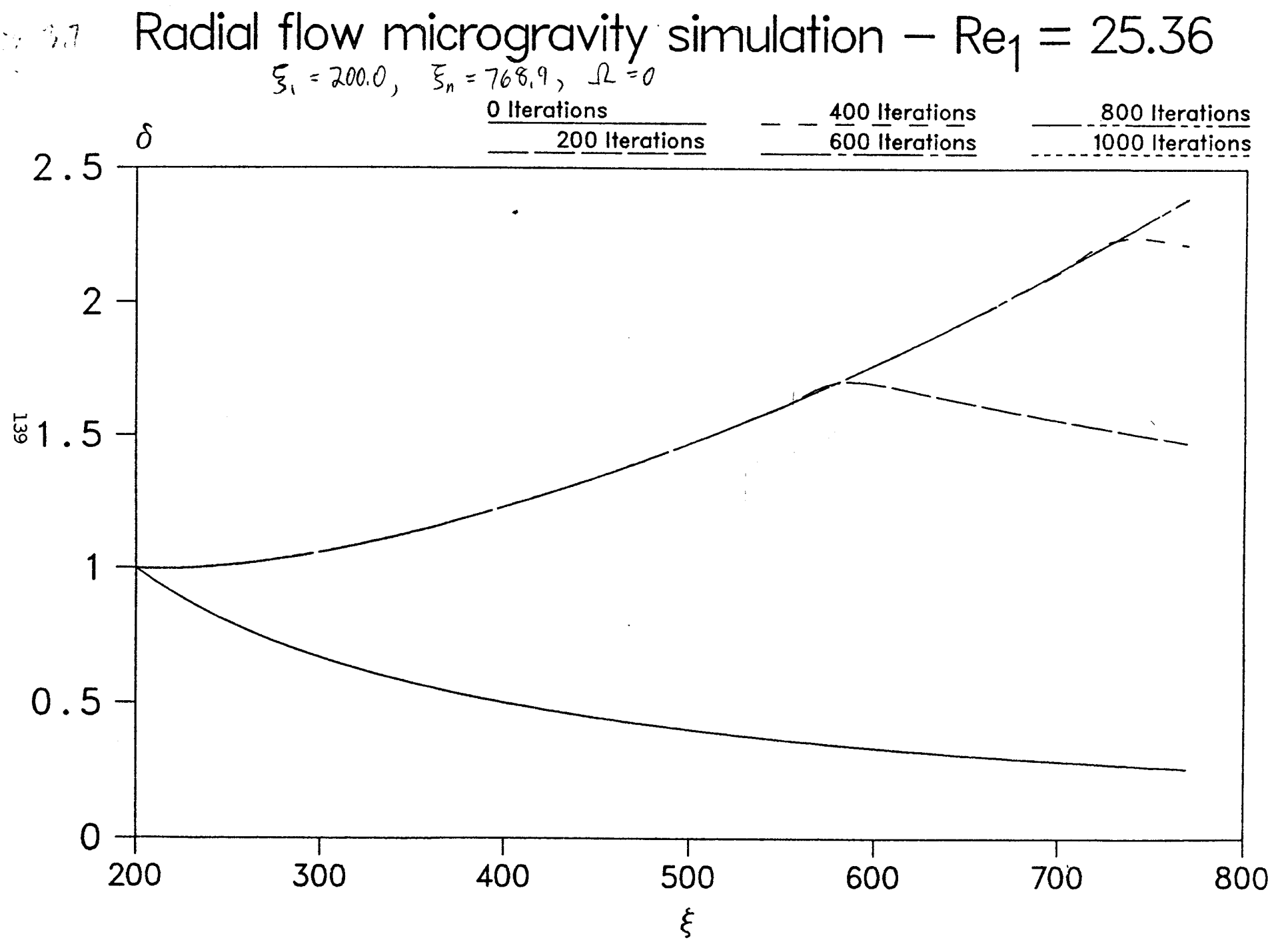
Radial flow microgravity simulation – $Re_1 = 25.36$
$\xi_1 = 200.0$, $\xi_n = 768.9$, $\Omega = 0$
0 Iterations
200 Iterations
400 Iterations
600 Iterations
800 Iterations
1000 Iterations
δ
2.5
2
1.5
1
0.5
0
200
300
400
500
600
700
800
ξ

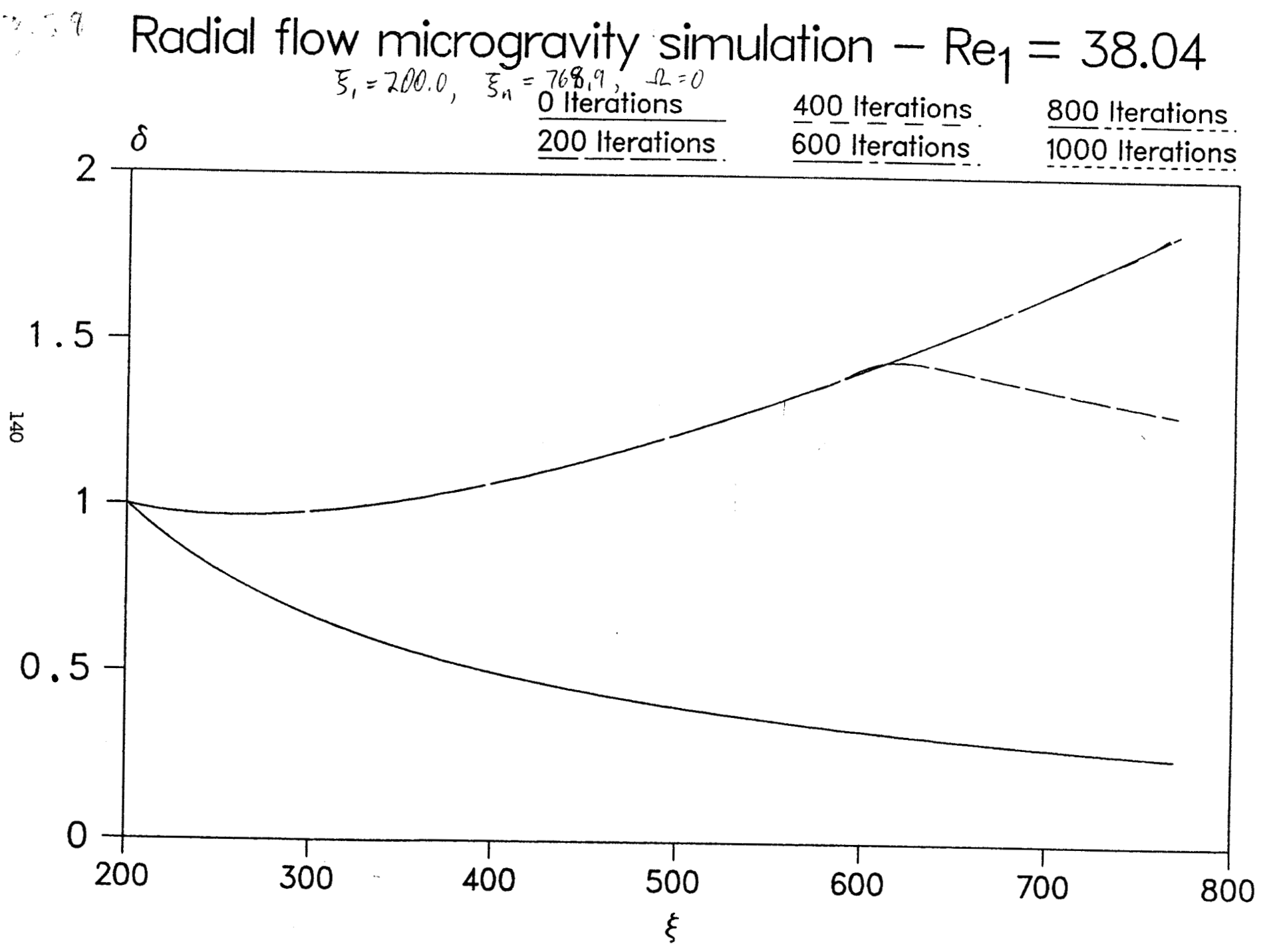
Radial flow microgravity simulation – $Re_1 = 38.04$
$\xi_1 = 200.0$, $\xi_n = 768.9$, $\Omega = 0$
0 Iterations
200 Iterations
400 Iterations
600 Iterations
800 Iterations
1000 Iterations
δ
2
1.5
1
0.5
0
200
300
400
500
600
700
800
ξ
140

Radial flow microgravity simulation – $Re_1 = 50.72$

$\Xi_1 = 200.0$, $\Xi_n = 768.9$, $\Omega = 0$

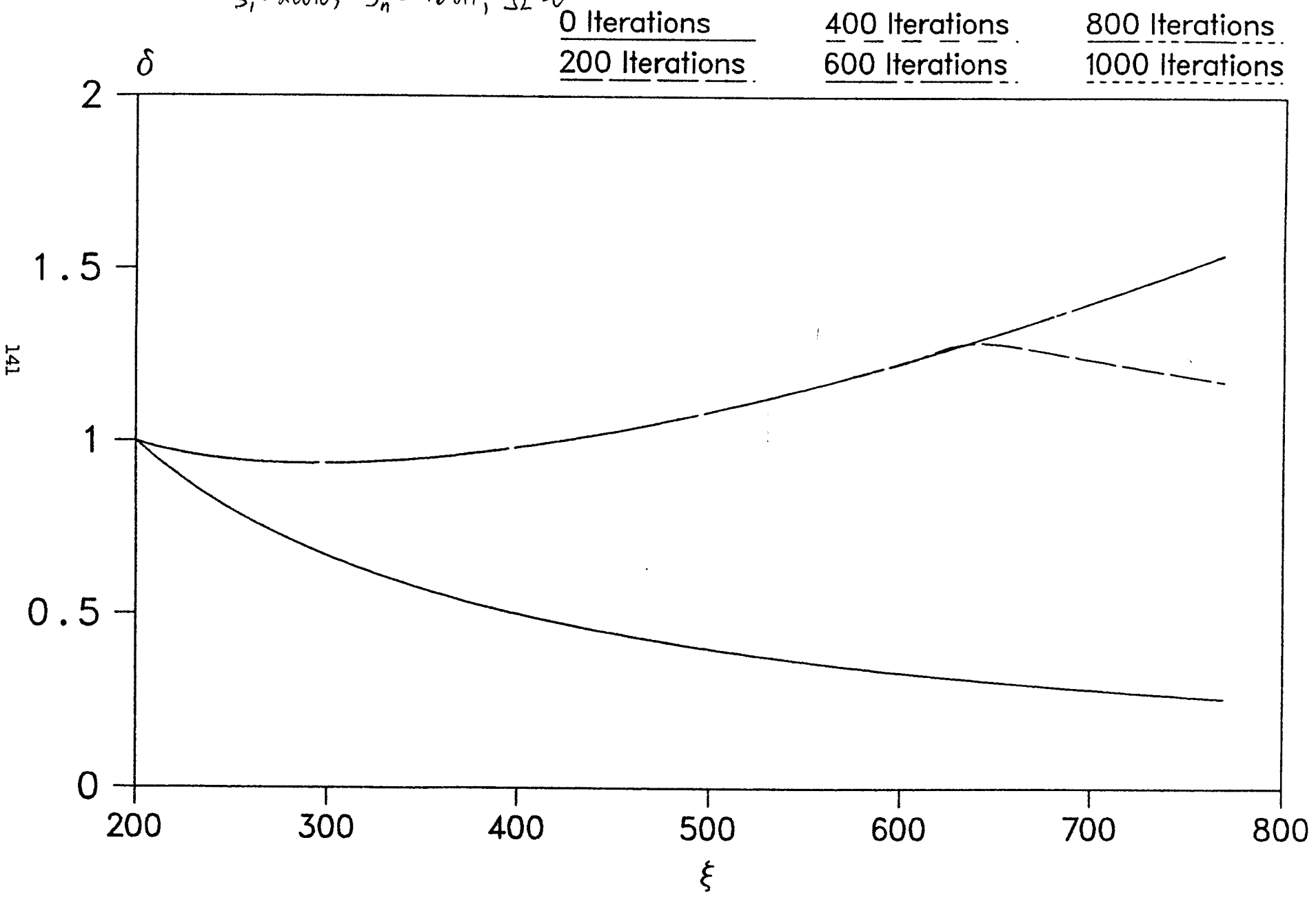

Fig. 3.10 Radial flow microgravity simulation – $Re_1 = 63.41$

$\xi_1 = 200.0$, $\xi_n = 768.9$, $\Omega = 0$

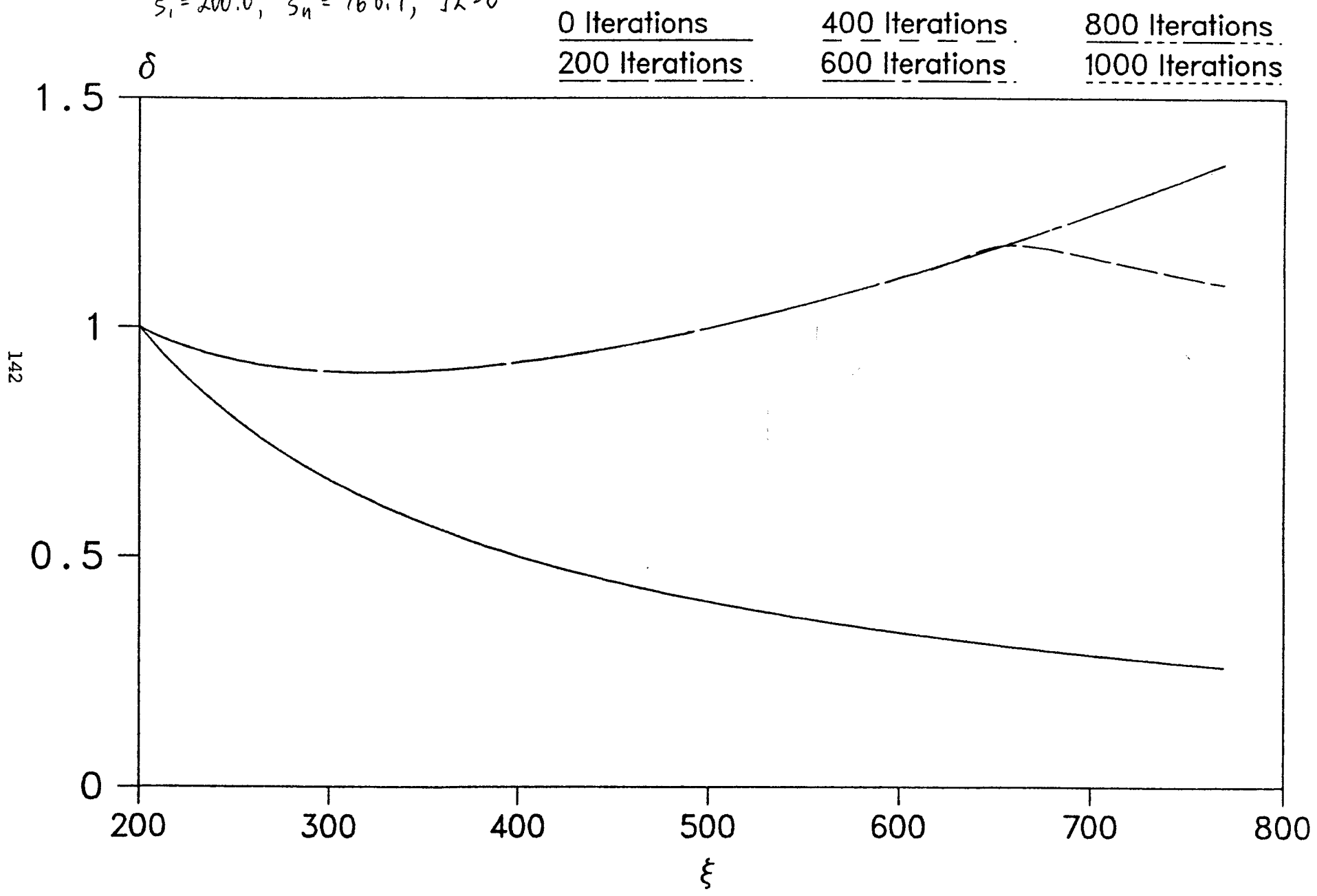

Radial flow microgravity simulation – $Re_1 = 76.06$

$\xi_1 = 200.0$, $\xi_2 = 768.9$, $\Omega = 0$

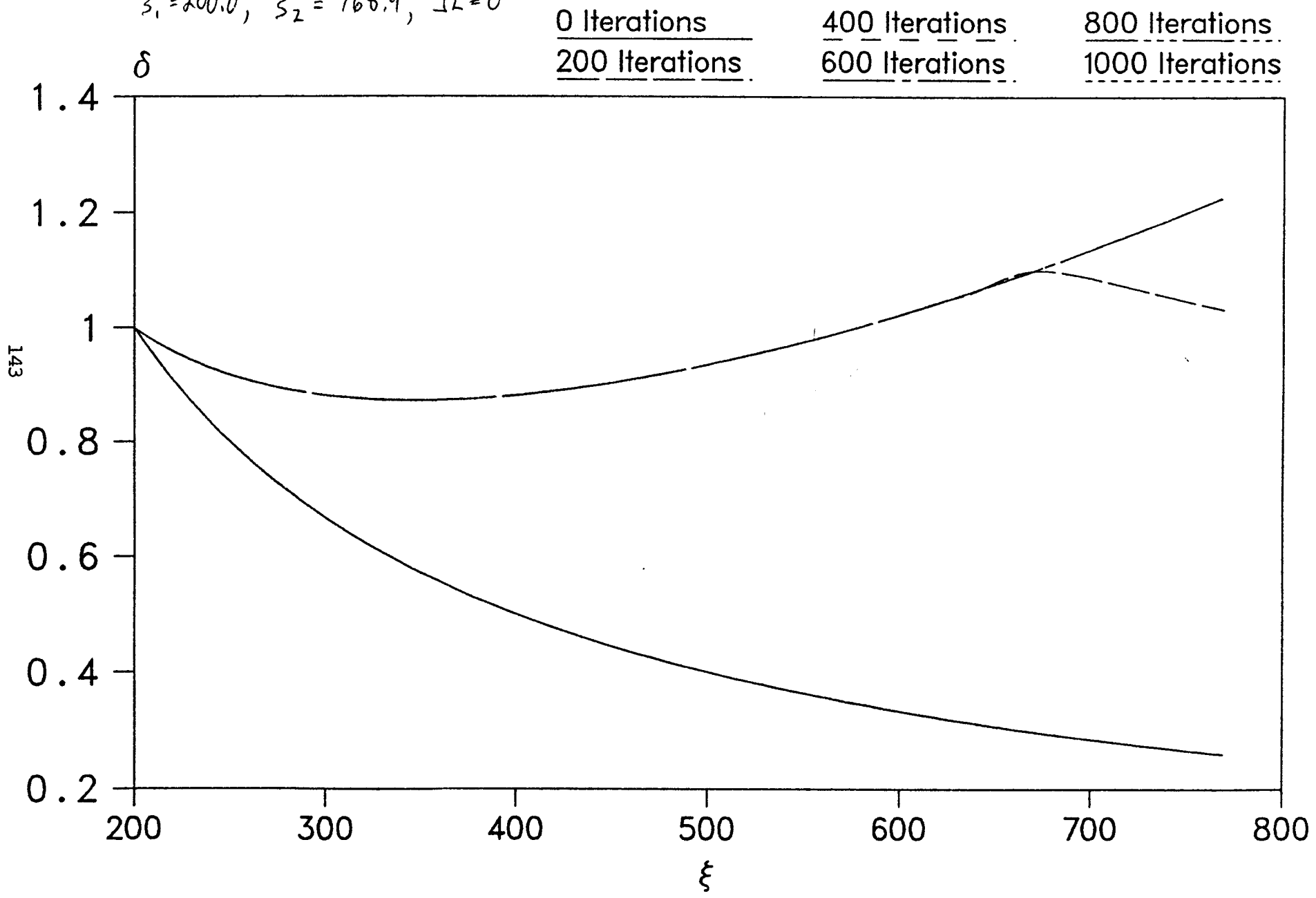

Fig 7.18 Radial flow – $Fr_1 = 5.0$, $Re_1 = 8.533$, $\xi_1 = 200.0$, $Fr_n = 1.0$, $\xi_n = 768.9$, $\Omega = 0.0$

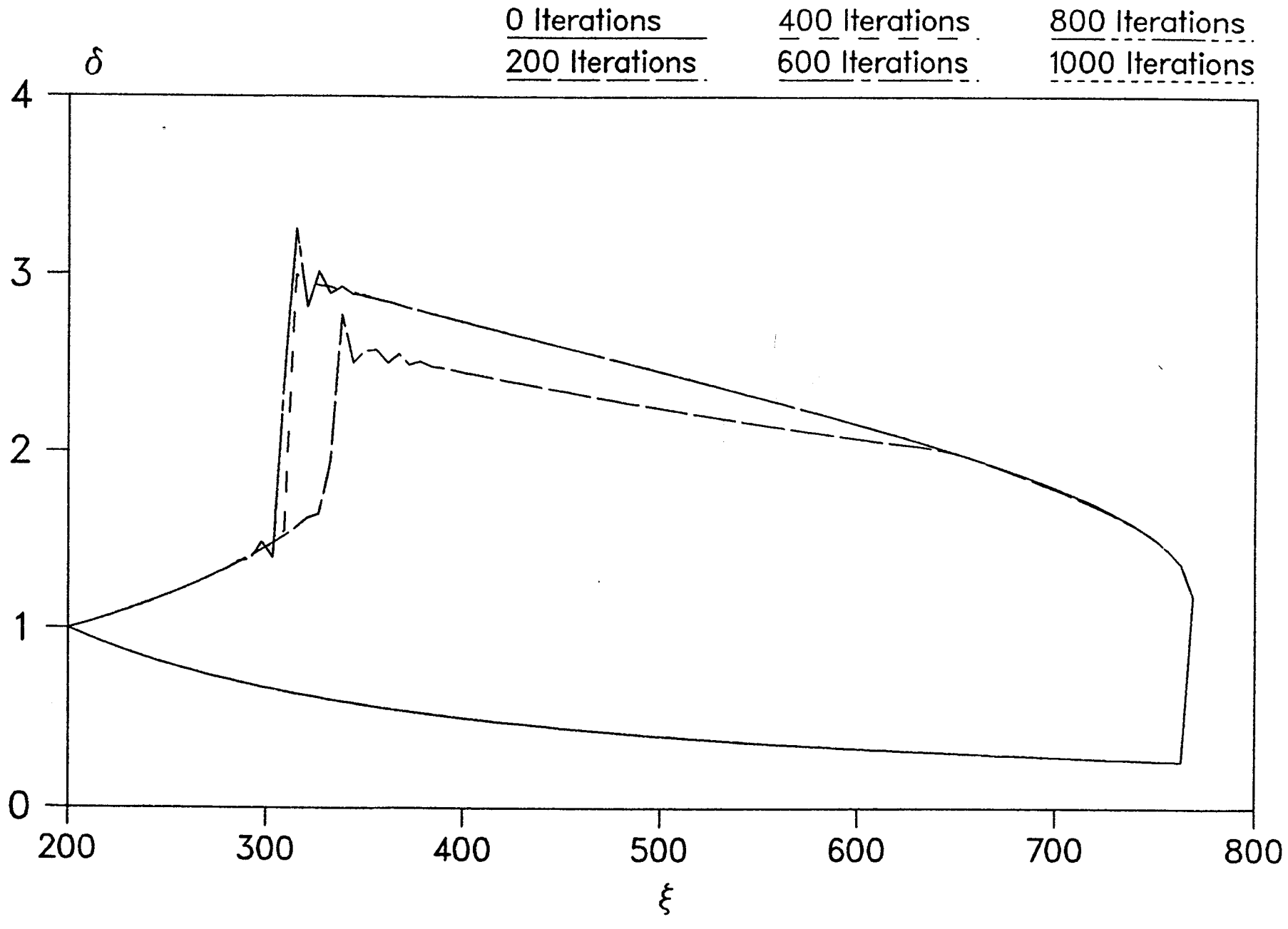

Radial flow – $Fr_1 = 5.0$, $Re_1 = 8.533$, $Fr_n = 1.0$, $\xi_1 = 200.0$, $\xi_n = 768.9$, $\Omega = 1.0E{-}3$

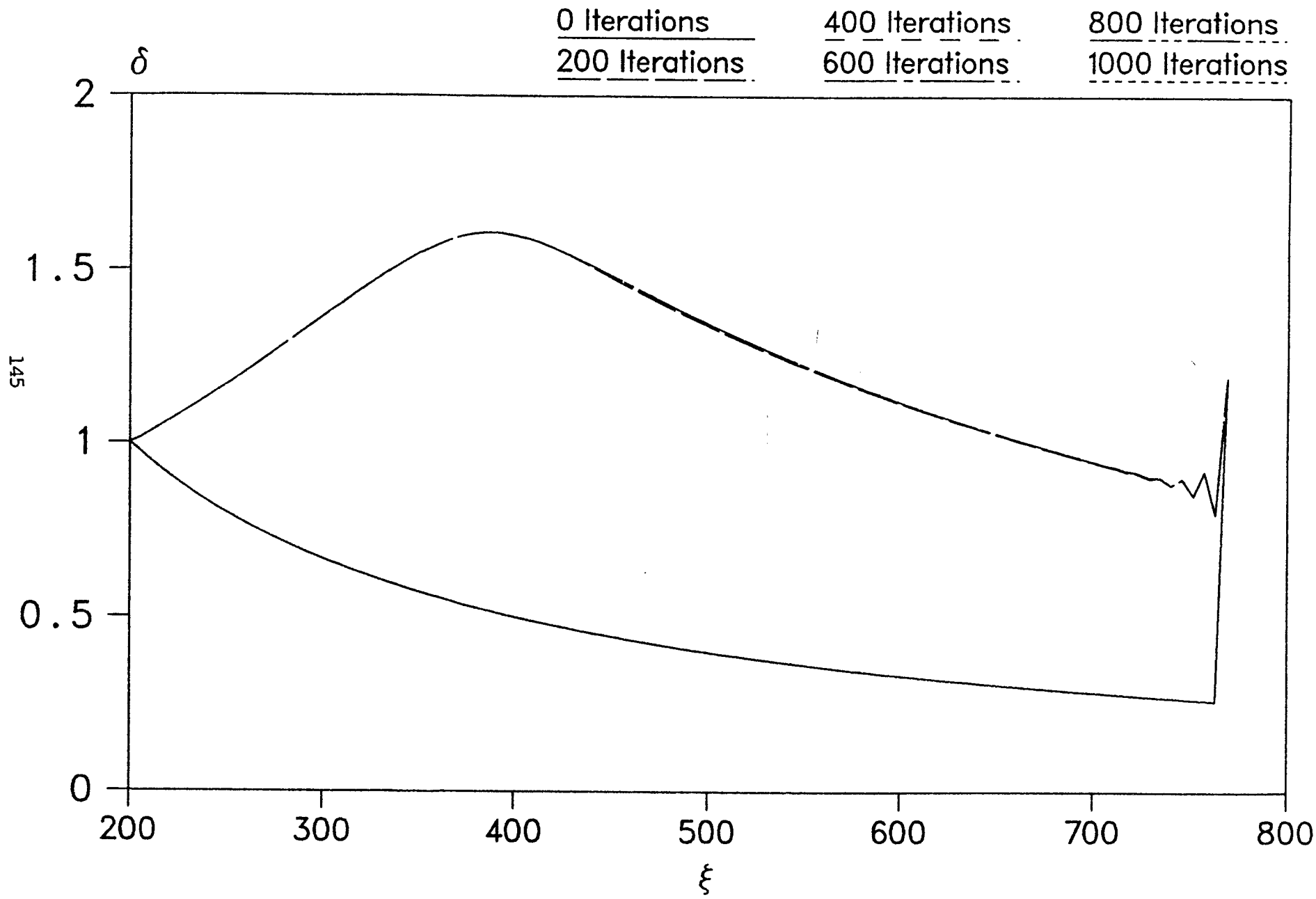

Fig. 3.14

Radial flow – $Fr_1 = 5.0$, $Re_1 = 8.533$, $Fr_n = 1.0$, $\xi_1 = 200.0$, $\xi_n = 768.9$, $\Omega = 1.0E{-}2$

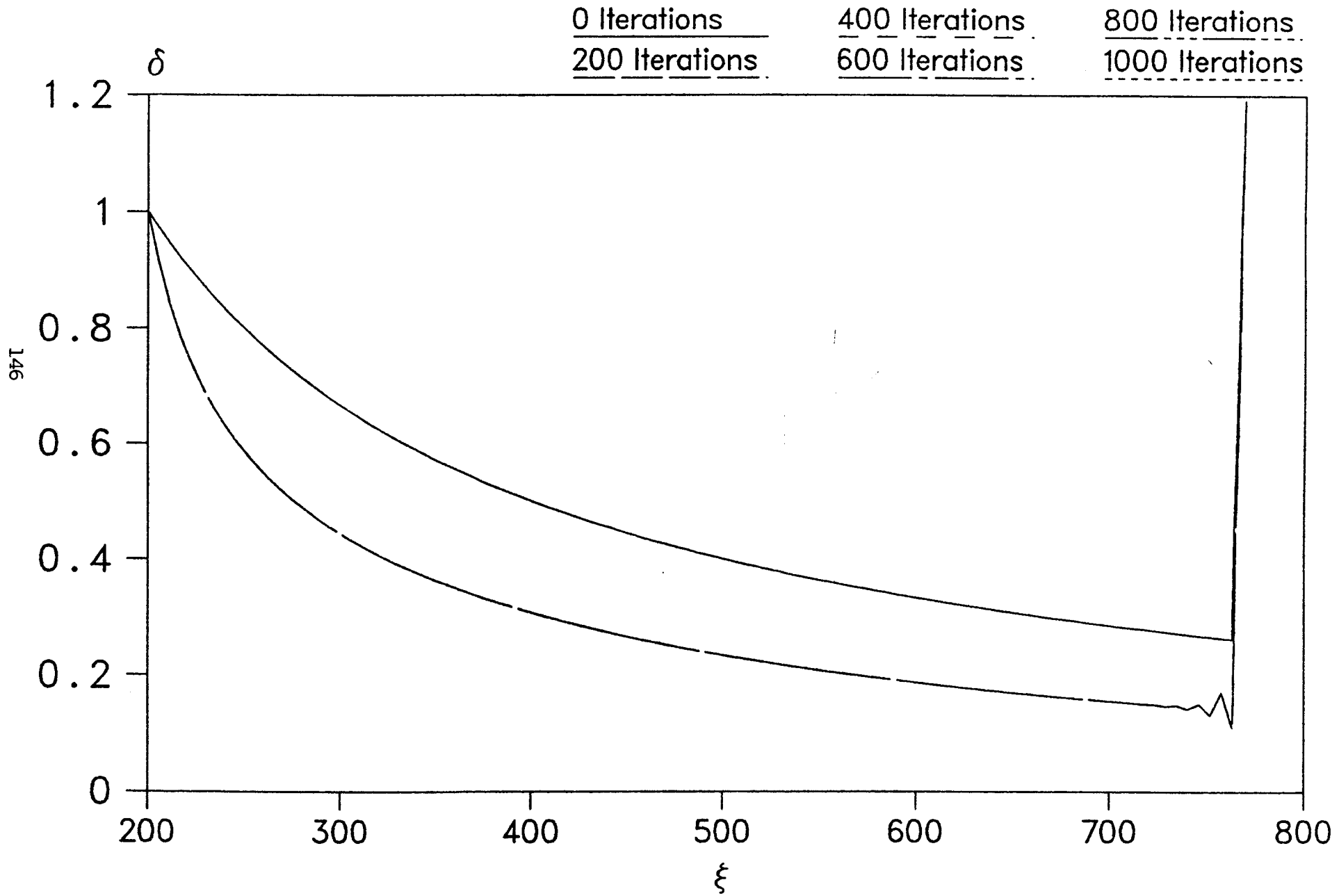

Fig. 3.15

Radial flow, 1–g, outlet boundary condition is not assigned.

$Fr_1 = 2.0$, $Re_1 = 25.36$, $\bar{\xi}_1 = 200.0$, $\bar{\xi}_n = 768.9$

0 Iterations
300 Iterations
600 Iterations
900 Iterations
1200 Iterations
1500 Iterations
1800 Iterations
2100 Iterations

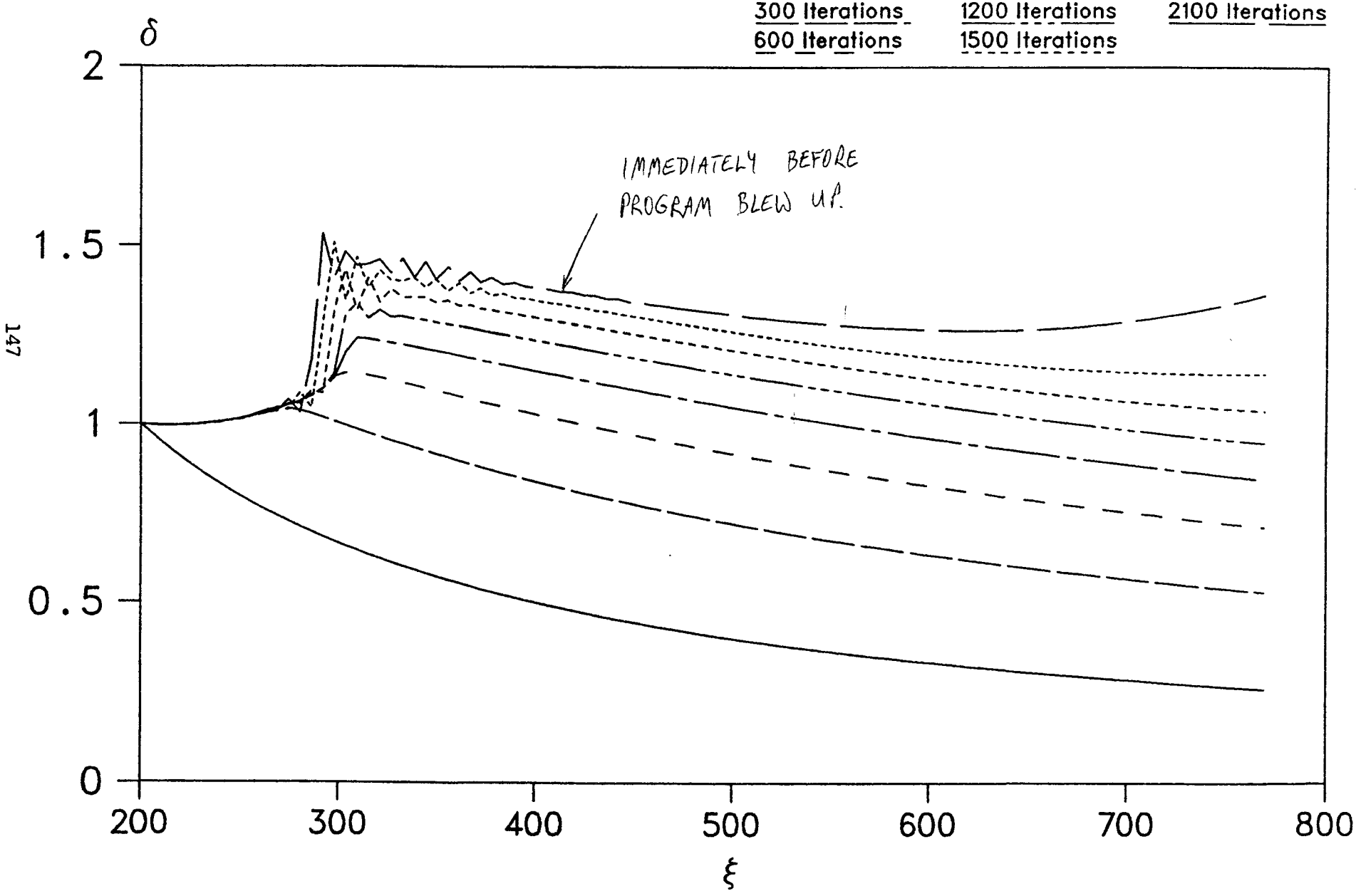

Fig. 3.16 Channel flow versus Radial flow – $Fr_1 = 4.0$, $Fr_n = 1.0$, $Re_1 = 50.71$, $\xi_1 = 200.0$, $\xi_n = 768.9$, $\Omega = 0.0$

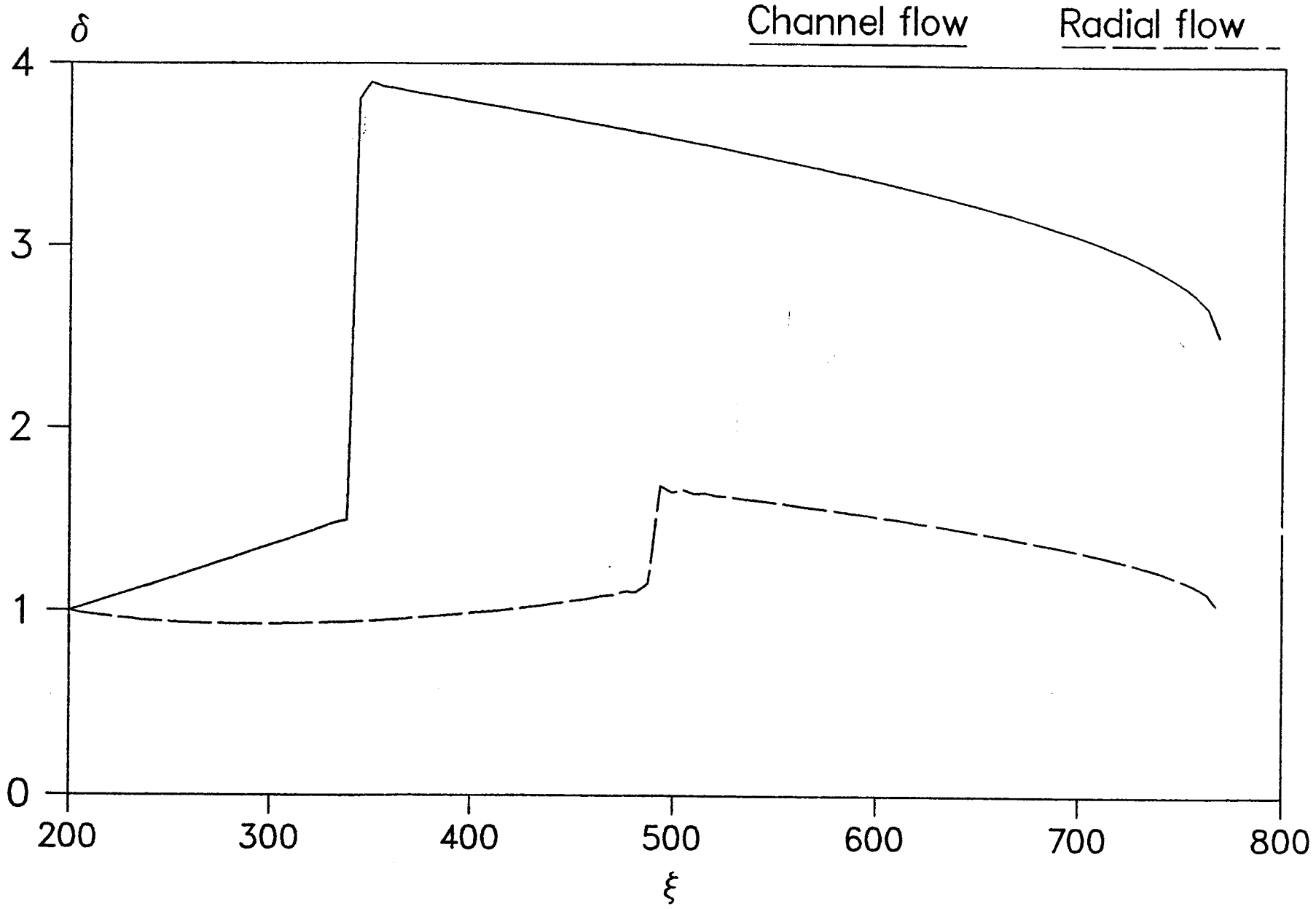

Fig. 3.17 Dimensionless liquid height versus dimensionless distance for radial flow with the Blasius friction factor increased with Fr_1=2.0, Fr_n=1.0, Re_1=25.36, ξ_1=200.0, ξ_n=768.9

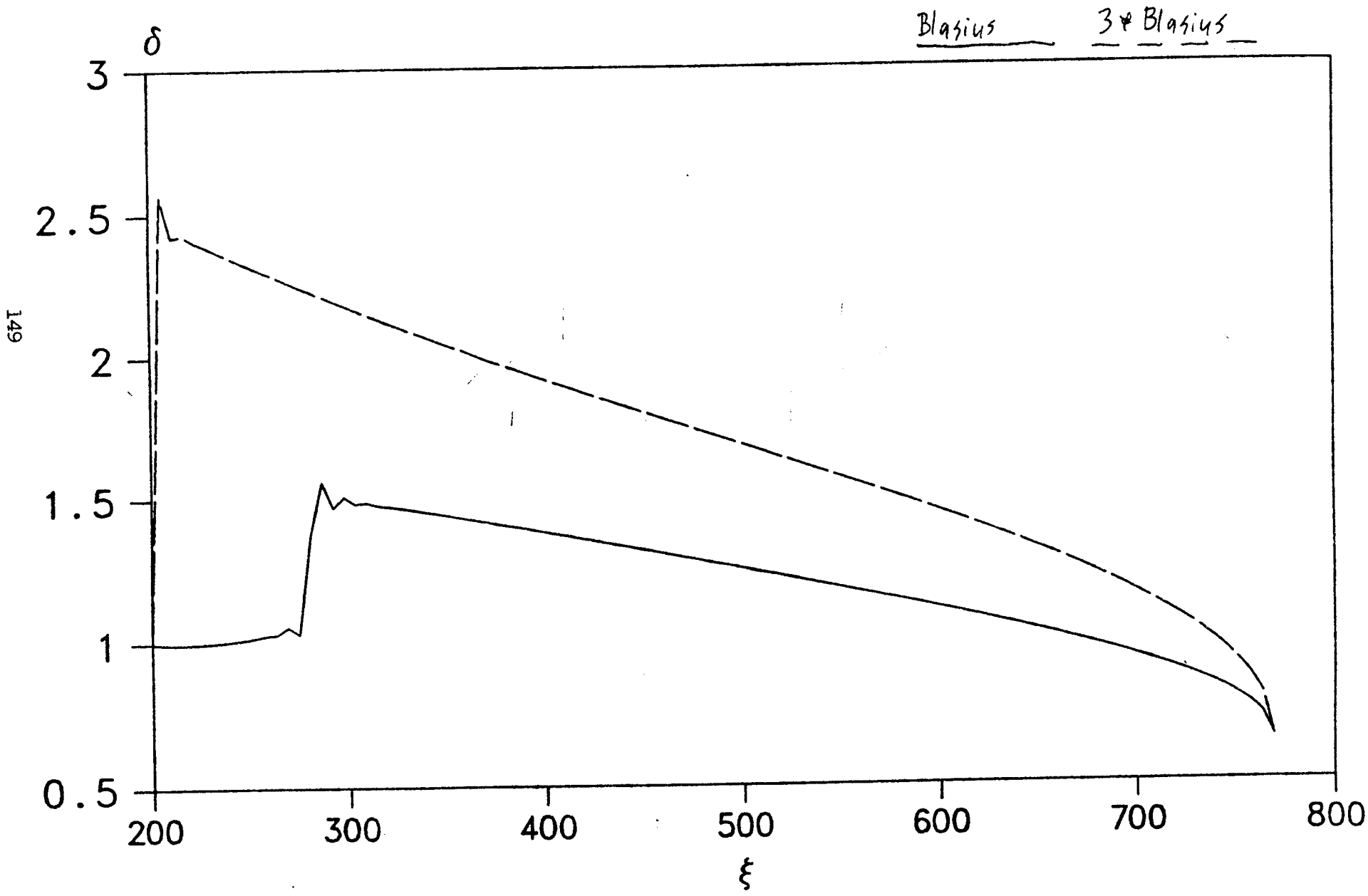

Fig. 7.19 Dimensionless liquid height versus dimensionless distance for radial flow with the Blasius friction factor increased with Fr_1=3.0, Fr_n=1.0, Re_1=38.04, ξ_1=200.0, ξ_n=768.9

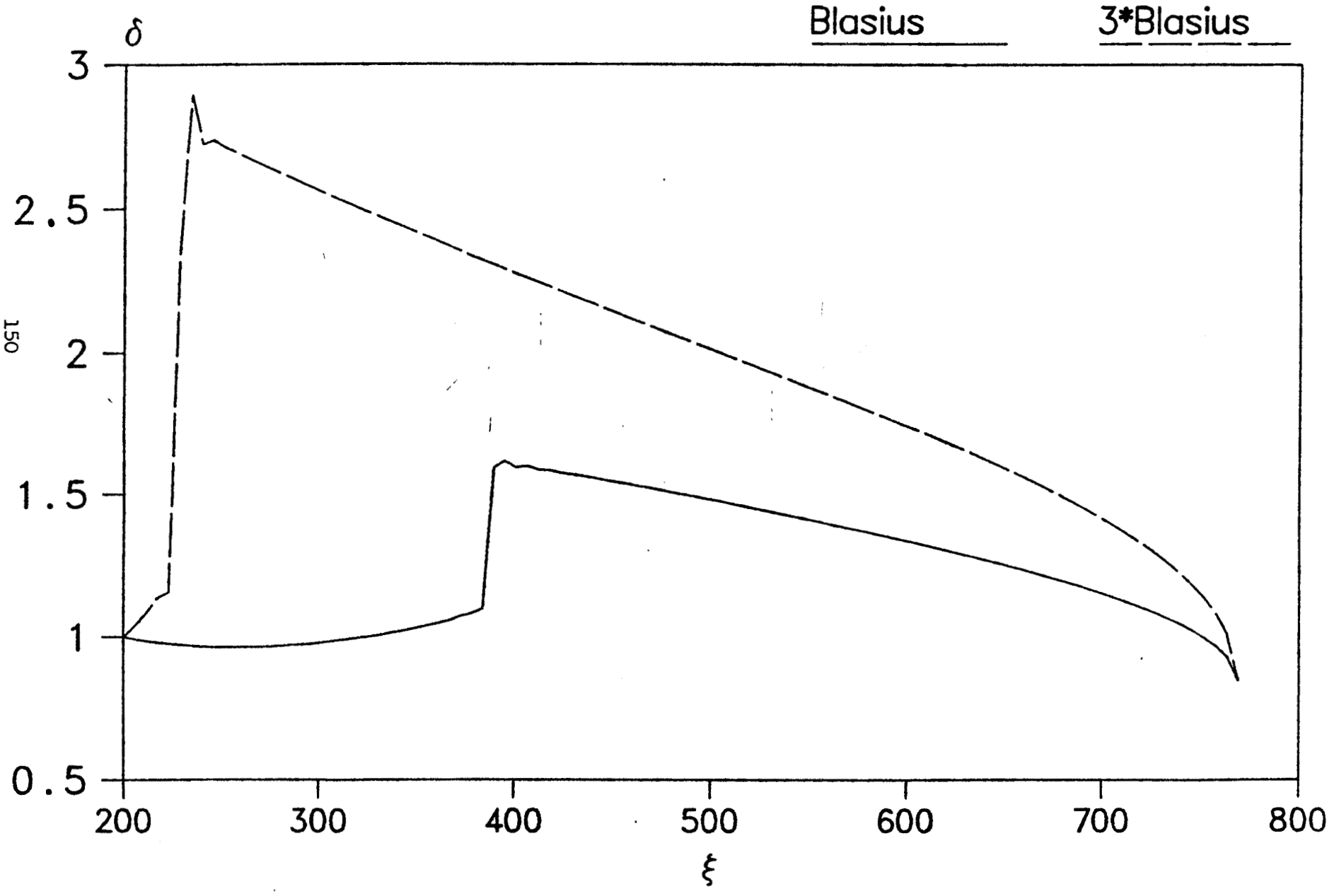

Fig. 3.19 Dimensionless liquid height versus dimensionless distance for radial flow with the Blasius friction factor increased with Fr_f=4.0, Fr_n=1.0, Re_f=50.72, ξ_f=200.0, ξ_n=768.9